Advanced Tank Car Collaborative Research Program
Research Report

Final Technical Report for Project TWP-10 – Revision 1

Correlating Material Properties to Puncture Resistance to Enhance the Safety and Security of Tank Cars

Steven W Kirkpatrick, Ph.D.
Applied Research Associates, Inc.

Peter C McKeighan[A], Ph.D., P.E.
For Exponent – Failure Analysis Associates

March 2018

Sponsored by the industry partners of the
Advanced Tank Car Collaborative Research Program (ATCCRP):
American Chemistry Council
Association of American Railroads
The Chlorine Institute
The Fertilizer Institute
Railway Supply Institute

[A] Currently with Hill Engineering, LLC

DISCLAIMER

This report was sponsored by the industry partners of the Advanced Tank Car Collaborative Research Program. It is disseminated for informational purposes only and is given to, and is accepted by, the recipient at the recipient's sole risk. American Chemistry Council (ACC), Association of American Railroads (AAR), The Chlorine Institute (TCI), The Fertilizer Institute (TFI) and Railway Supply Institute (RSI) make no representation or warranties, either expressed or implied, with respect to this report or its contents. ACC, AAR, TCI, TFI and RSI assume no liability to anyone for special, collateral, exemplary, indirect, incidental, consequential, or any other kind of damages resulting from the use or application of this report or its contents. Any attempt to apply the information contained in this report is made at the recipient's own risk.

Table of Contents

List of Figures

Figure **Page**

List of Tables

Table **Page**

Revision History

Rev.	Date	Sections	Description
0	Feb. 2018	All	Original report sponsored and released by the Advanced Tank Car Collaborative Research Program (ATCCRP).
1	Mar. 2018	Appendix B	Minor editorial corrections to the body of the report Appendix B added to describe the work performed under ATCCRP TWP-10A to characterize ASTM A240 Type 304L stainless steel and develop a corresponding constitutive model.

Acknowledgements

This program would not have been possible without the support of a number of organizations. First, the guidance of the Advanced Tank Car Collaborative Research Program (ATCCRP) group in assisting in this effort was invaluable and insightful during this work. Organizations that donated material for this effort are hereby recognized: Union Tank Car, Arcelor Mittal, SSAB and Trinity Industries. Several subcontractors performed testing on this program included Metcut (Cincinnati, OH) and University of Dayton Research Institute (Dayton, OH). Arcelor Mittal supported this effort and performed much of the initial characterization work for this program. Finally, numerous fruitful discussions were held with A.D. McKisic (Trinity), William Heitmann (Arcelor Mittal), Tanya Ros (Arcelor Mittal), Carl Hybinette (formerly Union Tank Car) and Phil Daum (ESI). Finally the support and patience of the Association of American Railroads during execution of this project is acknowledged.

This report describes analyses performed for the ATCCRP under a contract with the Association of American Railroads (AAR). Additional ATCCRP industry partners supporting this effort include the American Chemistry Council (ACC); the Chlorine Institute (CI); The Fertilizer Institute (TFI); and the Railway Supply Institute (RSI). The analysis methodologies used in this report build on the work previously performed under the Next Generation Rail Tank Car (NGRTC) Project.

Abstract

In the Next Generation Railroad Tank Car Project, testing and analysis were performed on TC128B material as well as other tank car steels (e.g. A1011, A516-70). In a similar material evaluation effort, the Chlorine Institute sponsored a program to characterize other high strength low alloy (HSLA) candidate steel materials (A710, HPS 70, and HPS 100). In this study, this past data is used and augmented by additional testing and analysis to evaluate the impact and puncture resistance performance of candidate materials that could be used in tank car structure (both shell and jacket). Understanding the appropriate form of material damage and failure models, predicting structural performance and linking behavior to basic material properties, will allow design optimization and selection of the most appropriate material for the tank structures.

The research program included detailed characterizations of various steel material samples (including a number of different TC128B variants). These detailed material characterizations included assessing tensile stress-strain properties as well as mechanical behavior of notched samples. As part of the research, detailed constitutive and damage models were developed for each material and the models were used to simulate the corresponding tests.

An unexpected result of this process was that the commonly used von Mises yield criterion could not adequately model the full range of tests in the material characterization data. Specifically, the von Mises assumption that the yield condition is independent of the mean stress resulted in the inability of the model to reproduce the load displacement curves for both the smooth and notched tensile tests. Moreover, as originally conceived, a number of different material failure models were proposed including the Bao-Wierzbicki, Gurson-Tvergaard and a maximum strain approach. In the end, the only suitable model for the materials considered herein was found to be the Bao-Wierzbicki model.

In addition to the direct material characterization, a series of puncture analyses were performed for various candidate materials to identify the material characteristics that most strongly control puncture resistance. Candidate materials with a wide range of mechanical properties were used in a suite of puncture analyses under various side impact conditions using a chlorine tank car geometry. These puncture results were then correlated to basic material properties (strength and ductility) with the form of the empirical correlations being simple linear combinations of different strength and ductility terms. Although these models are empirical, the roles of yield strength, ultimate strength, and ductility (percent elongation) are apparent from this modeling in terms of controlling puncture behavior.

The resulting correlations provide a predictive tool to rapidly screen candidate materials and hence avoid expensive and time-consuming laboratory tests and full-scale simulations on materials that will not yield significant performance improvements. Applying these models

(correlations) to various combinations of strength and ductility indicates that most common materials will net at best a modest improvements in puncture performance when compared with incumbent materials. The models indicate that significant improvements in puncture performance require candidate materials with markedly higher strength and ductility combinations than the incumbent materials (e.g. TC128B).

Correlating Material Properties to Puncture Resistance to Enhance the Safety and Security of Tank Cars

1 Introduction and Background

There is ongoing research to develop strategies for improving railroad tank cars so they can maintain tank integrity for more severe accident conditions than current equipment. Research results are being used to develop improved tank car designs and inform rulemaking by the Pipeline and Hazardous Materials Safety Administration (PHMSA). One area of research is to evaluate the effects of different steel materials that can be applied for enhanced tank car puncture protection. This report describes research to characterize and evaluate the performance of different steels.

A significant portion of the previous tank car material characterization testing and constitutive modeling methodologies were developed under the Next Generation Railroad Tank Car (NGRTC) Program [1]. A key effort in the NGRTC Program was the development and validation of detailed finite element constitutive and failure models which can be used to accurately predict the puncture resistance under different impact conditions. These validated methodologies are being applied in this study to assess the puncture protection potential of various candidate tank car steels.

In the Next Generation Tank Car Project analysis and testing was performed on TC128B material as well as other tank car steels (e.g. A1011, A516-70) [2-8]. In a similar material evaluation effort, the Chlorine Institute sponsored a program to characterize other high strength low alloy (HSLA) candidate steel materials (A710, HPS 70 and HPS 100) [9]. In this study, this past data is used and augmented by additional testing and analysis to evaluate the performance of these and other candidate materials that could be used in tank car structure (both shell and jacket). Understanding the appropriate form of material damage and failure models, predicting structural performance and linking behavior to basic material properties, will allow design optimization and selection of the most appropriate material for the tank structure.

The research described in this report extends these previous material characterization and modeling efforts and was performed as part of the Advanced Tank Car Collaborative Research Program (ATCCRP). The analysis methodologies used in this report build on the work of the previous research.

1.1 Problem Definition and Approach

Accident statistics show that the rail industry's safety performance has generally improved over the last few decades. The Federal railroad Administration's (FRA) Railroad Accident and Incident Reporting System (RAIRS) show that the number of accidents per year with at least one

car releasing hazardous materials has decreased significantly over the past 25 years [10]. However, a series of three clustered accidents or derailments involving the release of hazardous material focused attention on the structural integrity of railroad pressure tank cars. These events included (1) Minot, ND, on January 18, 2002; (2) Macdona, TX, on June 28, 2004; and (3) Graniteville, SC, on January 6, 2005 [11-13]. More recently, the July 6, 2013 derailment and fire of the crude oil tank car train in Lac-Mégantic, Quebec, along with other oil train derailments, have expanded the interest in improved puncture resistance for general purpose tank cars.

There are several proposed methods to improve the puncture resistance of tank cars. The most common are (1) increased thickness of the tank and/or jacket, (2) top and bottom fittings protection, (3) improved tank car materials, and (4) advanced protection systems such as sandwich structures or composites. Of these, the approach using improved tank car steels has the advantages of both maintaining the existing tank car designs and manufacturing processes and obtaining improved puncture resistance without adding weight to the tank car.

The approach in the study had three primary tasks. The first was to review and collect past work related to tank car and other candidate steels. This included the testing and analysis already completed by the NGRTC research program as well as other studies and structural applications. In addition, the Tank Car Committee efforts to identify and evaluate candidate TC128B replacement materials were included.

The second task in this study was to evaluate different analysis methodologies and material and damage models suitable for tank car puncture analyses. While substantial puncture modeling work has already been performed by Applied Research Associates, Inc. (ARA) and Quest Reliability, it is necessary to re-visit these analyses, review them critically, and assess where they work or do not work. Three primary failure criteria were considered: the Bao-Wierzbicki (BW), the Gurson-Tvergaard (G-T), and the critical plastic strain models.

The final task in this program was material characterization testing. It was anticipated that much of this study would use existing test data minimizing the need to generate additional experimental data. However, testing was required for new candidate steel materials that provide enhanced protection. In addition, additional testing was required on conventional tank car materials to address variability and metallurgical composition effects.

2 Material Constitutive and Damage Models

2.1 Introduction

Tank car impact and puncture analyses require a model for the material constitutive and damage behaviors to accurately predict the puncture threshold under various impact conditions. A piecewise linear elastic-plastic constitutive model was modified for this purpose to include the Bao-Wierzbicki (BW) failure criterion [14-16]. This model has been applied by other researchers to assess tank car puncture conditions [17] and is capable of reproducing both the nonlinear stress-strain behavior of the material as it deforms into the plastic regime and the fracture and failure behavior that depends on the state of stress and plastic strain history in the material. The material parameters used in these constitutive models were developed from the material test data on TC128B steel, developed under the NGRTC program [2-8].

The following sections describe the development of the constitutive and damage parameters used in the subsequent tank car puncture analyses.

2.2 Material Stress-Strain Behavior

2.2.1 Background Information on Continuum Mechanics

At the onset of this project, it was assumed that we would be applying typical computational methodologies for metal plasticity. These include a material model that applies a von Mises yield criterion and a hardening law based on the effective plastic strain. Although these modeling methodologies are appropriate for most applications of analysis of steel structures, we found that a fundamental assumption for these models was not suitable for the very detailed assessment of the material behaviors in different stress conditions. In particular, the von Mises criterion assumes that the yield stress is independent of the hydrostatic stress that resulted from experimental observations on metal plasticity, notably by Bridgeman [18]. We found in this study that the von Mises criterion could not reproduce the full range of material behaviors measured for the materials with sufficient accuracy.

Because we extended our investigation to include more advanced constitutive theories, we thought it helpful to include some background information on continuum mechanics. The information provided here uses descriptions from various sources including a background paper on effective stress and effective plastic strain [19] and other reference on continuum mechanics [e.g. 20].

The development of constitutive relations to describe nonlinear material response has a rich history drawing on developments in both experimental and theoretical mechanics. As a class of materials, metals have received the most attention from experimentalists and theoreticians in

developing constitutive relations which describe their behavior over a wide range of environments and applications. Many of the basic ideas and a lot of the terminology used to describe the behavior of other materials have their origin in the development of constitutive relations for metals. It is within the context of metal plasticity that the definition and function of effective stress and effective plastic strain will be presented.

2.2.1.1 Invariants of the Stress Tensor, σ_{ij}.

The stress tensor is assumed to be symmetric ($\sigma_{ij} = \sigma_{ji}$) and has six independent components which are defined at a point with respect to a set of coordinate axes. There are three normal stresses, $\sigma_{xx,}$ σ_{yy}, and σ_{zz}, and three shear stresses, $\sigma_{xy,}$ σ_{yz}, and σ_{zx}. It is always possible to select a special set of axes through the point so that the shear stress components are zero in the special coordinate system. These special axes are called principal axes and the three non-zero stress components are called principal stresses, which will be denoted as $\sigma_{1,}$ σ_2, and σ_3.

The principal stresses are physical qualities, scalar numbers, whose values do not depend on the coordinate system in which the components of stress were initially given. They are therefore invariants of the stress state, invariant with respect to rotation of the coordinate axes to which the stresses are referred. Similarly, the symbols I_σ, II_σ, and II_σ in the following scalar expressions denote additional invariants of the stress tensor with respect to rotation of the reference axes:

$$I_\sigma = \sigma_{xx} + \sigma_{yy} + \sigma_{zz} = \sigma_{ii}$$

$$II_\sigma = \sigma_{xx}\sigma_{yy} + \sigma_{yy}\sigma_{zz} + \sigma_{zz}\sigma_{xx} - \sigma_{xy}^2 - \sigma_{yz}^2 - \sigma_{zx}^2 = \frac{1}{2}(\sigma_{ii}\sigma_{jj} - \sigma_{ij}\sigma_{ij}) \quad (1)$$

$$III_\sigma = = \sigma_{xx}\sigma_{yy}\sigma_{zz} - \sigma_{xx}\sigma_{yz}^2 - \sigma_{yy}\sigma_{zx}^2 - \sigma_{zz}\sigma_{xy}^2 + 2\sigma_{xy}\sigma_{yz}\sigma_{zx}$$

If the axes of reference are chosen to align with the principal axes of the stress tensor, the much simpler algebraic forms given below are found in terms of the principal stresses.

$$I_\sigma = \sigma_1 + \sigma_2 + \sigma_3$$

$$II_\sigma = \sigma_1\sigma_2 + \sigma_2\sigma_3 + \sigma_3\sigma_1 \quad (2)$$

$$III_\sigma = = \sigma_1\sigma_2\sigma_3$$

In any two coordinate systems, the numerical value of any of the individual components will in general be different, but the numerical value of the invariants will be the same.

I_σ is called the first invariant of the stress tensor; it is also called the trace of the stress matrix, denoted tr(σ), which is the sum of the elements of the main diagonal (the three normal stresses). The second invariant II_σ is a homogeneous quadratic expression in the stress components; it is the sum of the three minor determinants of the diagonal elements in the determinant of the stress matrix. The third invariant III_σ is the determinant of the stress matrix, denoted by det(σ), and is a homogeneous cubic expression in the stress components. These tensor invariants should be thought of as characterizing a tensor, just as the length invariant characterizes to some extent a vector. Many writers use the notation I_1, I_2, I_3 or J_1, J_2, J_3 instead of I_σ, II_σ, III_σ for the invariants of the stress tensor.

2.2.1.2 Spherical and Deviatoric Stress Tensors·

The stress tensor, σ_{ij}, can be written as the sum of two tensors, one representing a spherical or hydrostatic state of stress and the second called the deviatoric stress (S_{ij}). Let $\hat{\sigma}$ denote the mean normal stress (p is the mean normal pressure).

$$\hat{\sigma} = -p = \frac{1}{3}\left(\sigma_{xx} + \sigma_{yy} + \sigma_{zz}\right) = \frac{1}{3}\sigma_{ii} \tag{3}$$

Thus for the deviatoric stress we have

$$S_{ij} = \sigma_{ij} - \hat{\sigma}\delta_{ij} \tag{4}$$

where δ_{ij} is the Kronecker delta defined by

$$\delta_{ij} = \begin{cases} 1 \text{ if } i = j \\ 0 \text{ if } i \neq j \end{cases} \tag{5}$$

Many writers use the notation σ'_{ij} instead of Sii for the deviatoric stress.

In general, the deviatoric stress is associated with changes in shape, while the hydrostatic stress produces volume change without changing the shape in an isotropic continuum, i.e. in a material with the same properties in all directions.

2.2.1.3 Invariants of the Deviatoric Stress Tensor, S_{ij}·

The principal directions of the deviatoric stress tensor are the same as those of the stress tensor, since both represent directions perpendicular to planes having no shear stress. Although the principal directions are the same for the deviatoric and stress tensors, the principal values are not the same. The principal deviator stresses are the principal stresses scaled by subtracting the mean normal stress (adding the pressure) and are given by

$$S_k = \sigma_k - \hat{\sigma} = \sigma_k + p \tag{6}$$

In the same manner that we found the invariants of the stress tensor, we may also determine the invariants of the deviator stress. The invariants of the deviatoric stress tensor are given by

$$\mathrm{I_S} = S_1 + S_2 + S_3 = 0$$

$$\mathrm{II_S} = S_1S_2 + S_2S_3 + S_3S_1 \tag{7}$$

$$\mathrm{III_S} = = S_1S_2S_3$$

which are analogous to those given for the stress tensor by Eqs. (2), but calculated with the principal components of the deviatoric stress. Note that the first invariant of the deviatoric stress, $\mathrm{I_S}$, is zero since we defined the deviatoric stress to be the stress tensor minus the pressure.

Alternative expressions for $\mathrm{II_S}$ are

$$\mathrm{II_S} = \frac{1}{2}S_{ij}S_{ij} = \frac{1}{2}(S_{xx}^2 + S_{xx}^2 + S_{xx}^2) + \sigma_{xy}^2 + \sigma_{yz}^2 + \sigma_{zx}^2 \tag{8}$$

$$\mathrm{II_S} = \frac{1}{6}\left[(\sigma_{xx} - \sigma_{yy})^2 + (\sigma_{yy} - \sigma_{zz})^2 + (\sigma_{zz} - \sigma_{xx})^2\right] + \sigma_{xy}^2 + \sigma_{yz}^2 + \sigma_{zx}^2 \tag{9}$$

$$\mathrm{II_S} = \frac{1}{6}[(\sigma_1 - \sigma_2)^2 + (\sigma_2 - \sigma_3)^2 + (\sigma_3 - \sigma_1)^2] \tag{10}$$

Some writers use the notation J_1, J_2, and J_3 to denote the invariants of the deviatoric stress tensor, but the most common notation is J_2' and J_3' which we will use in the following discussion of constitutive relations; since $J_1' = 0$, it is seldom used.

2.2.1.4 Generalized Yield Criteria

A yield criterion determines what levels and combinations of three dimensional stress states permit inelastic (plastic) response to begin. This can be expressed mathematically as

$$\begin{aligned} f(\sigma_{ij}) &< 0 \; for \; elastic \; response \\ f(\sigma_{ij}) &= 0 \; for \; plastic \; response \end{aligned} \tag{11}$$

This yield condition can be interpreted geometrically in terms of a surface $f(\sigma_{ij}) = 0$, i.e. a hypersurface in a nine-dimensional space in which the stresses σ_{ij} are interpreted as nine Cartesian coordinates. Since σ_{ij} is symmetric, we can alternatively interpret the yield surface as a

surface in six-dimensions. If the stress state is inside the surface, $f(\sigma_{ij}) < 0$, the response is elastic. If the stress state is on the surface, $f(\sigma_{ij}) = 0$, the response is plastic. Note that the stress state is never outside of the surface; $f(\sigma_{ij}) \leq 0$ always. If the stress state is estimated to lie outside the yield surface, then the surface moves (kinematic hardening) or changes shape (isotropic hardening) and/or the strains are adjusted (plastic straining) until $f(\sigma_{ij}) = 0$.

We now consider additional assumptions, limiting the generality of the yield criteria and some consequences that follow from the assumptions. Not all the additional assumptions are made in every plasticity theory, but all are included in the theories most widely used for metal plasticity.

2.2.1.5 Assumption 1. Yield is independent of the spherical part of the stress.

Experimental observations by Bridgeman [18], indicate that plastic deformation of metals is essentially independent of hydrostatic pressure. Because of the difficulties in loading a specimen in hydrostatic tension, most experimental verifications have been limited to superimposed hydrostatic compression, but the postulate is also assumed to apply to hydrostatic tension. It follows from this assumption that the function $f(\sigma_{ij})$ must in fact be a function only of the deviatoric stress.

$$f(\sigma_{ij}) = f(S_{ij}) \tag{12}$$

2.2.1.6 Assumption 2. The material is isotropic.

If the material is isotropic, there can be no preferred direction and the yield function should have the same form for all orientations of the rectangular Cartesian coordinate axes relative to the material. This implies that the yield function should only depend on the principal values of the stress and indeed it must be a symmetric function of the principal values of stress, since an isotropic material is unable to distinguish one principal direction, and associated principal value, from another.

One way to mathematically express this symmetry condition of the yield function is to use the invariants of the stress rather than the principal values. This is possible since the invariants are completely determined by the principal values and are symmetric functions of the principal values. The reader may easily verify that the stress invariants given in Eqs. (6) are symmetric functions of the principal values.

Assumptions 1, f is independent of pressure thus $f = f(S_{ij})$, and 2, f is symmetric and thus $f = f(I_\sigma, II_\sigma, III_\sigma)$, imply that f must be a function of the invariants of the deviatoric stress tensor. Thus the yield function must be expressible as

$$f(\sigma_{ij}) = f(J_2', J_3') \tag{13}$$

for an isotropic material which is independent of the hydrostatic part of the stress tensor.

2.2.1.7 Assumption 3. Yield is independent of the sign of the stresses.

For most isotropic polycrystalline metals the initial yielding in tension and compression occurs at the same level of stress. This is usually postulated to apply to the general yield function by requiring

$$f(-\sigma_{ij}) = f(\sigma_{ij}) \tag{14}$$

This assumption and the assumption of isotropy may both lead to significant departures from observed behavior when applied to materials after previous plastic deformation, but experience indicates that they work reasonably well for initial yield. In frictional materials, such as soil, rock, or concrete, Assumption 3 is definitely incorrect, since these materials are much weaker in tension than compression, e.g. these materials fracture, crack, or pull apart in tension.

2.2.2 The Von Mises Yield Criterion

The two simplest, and most widely used yield criteria are the Tresca criterion and the von Mises criterion. Both of these criteria satisfy all three of the above assumptions about the form of yield criteria functions. We will concern ourselves only with the von Mises criterion, since its use is much more prevalent in numerical analyses, while the Tresca criterion is more often used in closed form analyses due to its less complex form for simple states of stress.

von Mises suggested that yielding occurs when the second invariant of the deviatoric stress J_2' reaches a critical value, or

$$\sqrt{J_2'} = k \tag{15}$$

in which k is a material parameter to be determined. This yield criterion mayalso be written as

$$\sigma_{eff} = \sqrt{3J_2'} = \sqrt{3}k \tag{16}$$

and σ_{eff} is termed the effective stress, generalized stress, or equivalent stress.

Some physical insight into the definition of effective stress is gained by considering the case of uniaxial yielding. For the uniaxial case the principal stresses at yield are $\sigma_1 = \sigma_y$, $\sigma_2 = \sigma_3 = 0$ and thus

$$-p = \frac{1}{3}(\sigma_1 + \sigma_2 + \sigma_3) = \frac{1}{3}\sigma_y \tag{17}$$

and

$$S_1 = \sigma_1 + p == \frac{2}{3}\sigma_y$$
$$S_2 = \sigma_2 + p = -\frac{1}{3}\sigma_y \tag{18}$$
$$S_3 = \sigma_3 + p = -\frac{1}{3}\sigma_y$$

then

$$J_2' = \frac{1}{2}S_{ij}S_{ij} = \frac{1}{2}(S_1^2 + S_2^2 + S_3^2) = \frac{1}{3}\sigma_y^2 = k^2 \tag{19}$$

Or for the von Mises criterion

$$\sigma_{eff} = \sigma_y = \sqrt{3J_2'} \tag{20}$$

2.2.3 The Drucker Prager Yield Criterion

As described in the previous section, one of the primary assumptions built into the von Mises yield model is that the yield is independent of the spherical part of the stress. However, this approximation was challenged in the 1970s by the experiments of Richmond, Spitzig, and Sober [21-24]. They studied the effects of hydrostatic pressure on the yield strength of various steels. Their research found that the yield was dependent on the hydrostatic stress level at pressure levels significantly less than the maximum pressures used by Bridgman years earlier.

In general, the independence of yield on hydrostatic stress is a reasonable approximation for analysis of ductile metals. However, some researchers have determined the need to eliminate this approximation for analysis of specific metals and loading conditions [e.g. 25-26]. The most common approach in this case is to apply a yield function identical to one proposed by Drucker and Prager [27] for soils described the yielding process. The Drucker-Prager yield function can be written as a modification of the von Mises yield criterion [19, 20] that includes a term dependent on the first stress invariant as:

$$\sqrt{J_2'} + \alpha I_\sigma = k \tag{21}$$

This form of yield function is included in later analyses of the materials tested in this program.

2.3 Material Damage Models

Accurate prediction of the response and puncture behavior of tank car materials requires a nonlinear constitutive and damage model. The primary function of the constitutive model is to determine the internal forces (stress) that are developed as the material is deformed (strained) under various loading and deformation conditions. The corresponding damage model determined the accumulation of damage and corresponding failure of the material for a given deformation history.

The damage models described here apply local fracture mechanics approaches (LFM) that model the microstructural deformation and failure processes leading to fracture in terms of continuum parameters averaged over a small volume of material [28-35]. LFM focuses on the evolution of the process zone, in contrast to classical linear elastic and elastic-plastic fracture mechanics (LEFM and EPFM, respectively), which characterize fracture in terms of the boundary conditions of the fracture process zone. Although LFM may initially seem more complex to formulate and more difficult to apply than LEFM/EPFM, it is more versatile and more general. LFM is also ideally suited to implementation into finite element analyses where damage can be evaluated at the local element level.

One objective of the analyses in this study was to evaluate a few commonly used damage models for ductile materials. The most commonly used failure criterion is to apply a single critical value of the plastic strain. The damage model applied for puncture analyses in the NGRTC program [1] was the Bao-Wierzbicki (BW) model. An alternate failure model applied in a series of analyses for the Chlorine Institute was the Gurson-Tvergaard (G-T) model [9]. These models are described in the following sections.

2.3.1 Bao-Wierzbicki Failure Surface

The key mechanism that needs to be included in the ductile local fracture model for tank car puncture analyses is the influence of the stress state on the rate of damage development as the material is undergoing plastic deformation. The primary stress state factor that controls the rate of damage development is the stress triaxiality, defined as the ratio of the mean stress to the equivalent stress ($\sigma_{mean}/\sigma_{eq}$). The mean stress (or hydrostatic stress) and equivalent stress (or effective stress or the von Mises stress) were defined previously in Equations (15) and (16).

There are many models that include the effects of stress triaxiality on damage development and ductility. Several of these have previously been applied within LS-DYNA to analyze various ductile fracture problems [e.g. 36-38] including the use of the Gurson-Tvergaard model [39-41] for the puncture assessment of pressure tank cars [42]. These models have the ability to include the stress triaxiality effects on ductility for tensile loading as illustrated in Figure 1. The deficiency with many of these previous local damage models is that they do not include the

changes in damage development and failure for low triaxiality where the tensile damage and failure behavior transitions into a shear dominated fracture behavior. The concern that shear fracture behavior is important for tank car puncture assessment led to the selection of the Bao-Wierzbicki (BW) model in this effort.

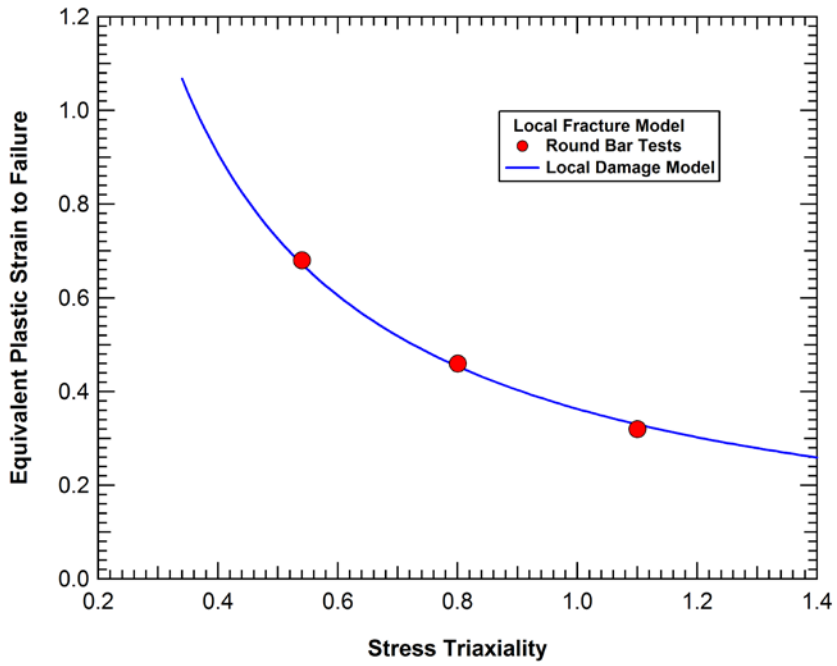

Figure 1. Local damage criterion for tensile ductile fracture analyses.

As implemented, the BW model is a basic form of a ductile fracture criterion [31]. It assumes that failure at a material location occurs when the damage within a surrounding characteristic volume (V_{MIC}) exceeds a critical value. The damage development and failure criterion can be written in the form

$$D = \int \frac{d\varepsilon_{eq}^{p}}{\varepsilon_c\left(\sigma_{mean}/\sigma_{eq}\right)} = 1 \quad \text{over } V_{MIC} \tag{22}$$

where D is the normalized damage parameter; $d\varepsilon_{eq}^{p}$ is an increment in equivalent plastic strain; and $\varepsilon_c\left(\sigma_{mean}/\sigma_{eq}\right)$ is the critical failure strain as a function of the stress triaxiality. The characteristic volume (V_{MIC}) in this application is the element size which was maintained with a characteristic element length of approximately 0.040 inch (1 mm) in the fracture zone. Damage accumulation occurs with plastic deformations and the damage is tracked locally in each element in the model. When the damage level in any element exceeds the failure criterion (D=1), the local failure is propagated in the model by element erosion.

The critical strain function is that proposed in the BW criterion and contains multiple branches depending on the range of stress state as shown in Figure 2. The critical strain in each branch are governed by the equation

$$\varepsilon_c\left(\sigma_{mean}/\sigma_{eq}\right)=\begin{cases}\infty & \left(\sigma_{mean}/\sigma_{eq}\right)\le -\dfrac{1}{3}\\ \dfrac{A}{1+3\left(\sigma_{mean}/\sigma_{eq}\right)} & -\dfrac{1}{3}\le\left(\sigma_{mean}/\sigma_{eq}\right)\le 0\\ 9(B-A)\left[\left(\sigma_{mean}/\sigma_{eq}\right)\right]^2+A & 0\le\left(\sigma_{mean}/\sigma_{eq}\right)\le\dfrac{1}{3}\\ \dfrac{B}{3\left(\sigma_{mean}/\sigma_{eq}\right)} & \dfrac{1}{3}\le\left(\sigma_{mean}/\sigma_{eq}\right)\end{cases} \tag{23}$$

And the parameters *A* and *B* can be determined by a series of tests under different stress conditions including notched tensile tests with specimens of varying notch radii [43] and tensile-shear tests with different ratios of tension to shear stress.

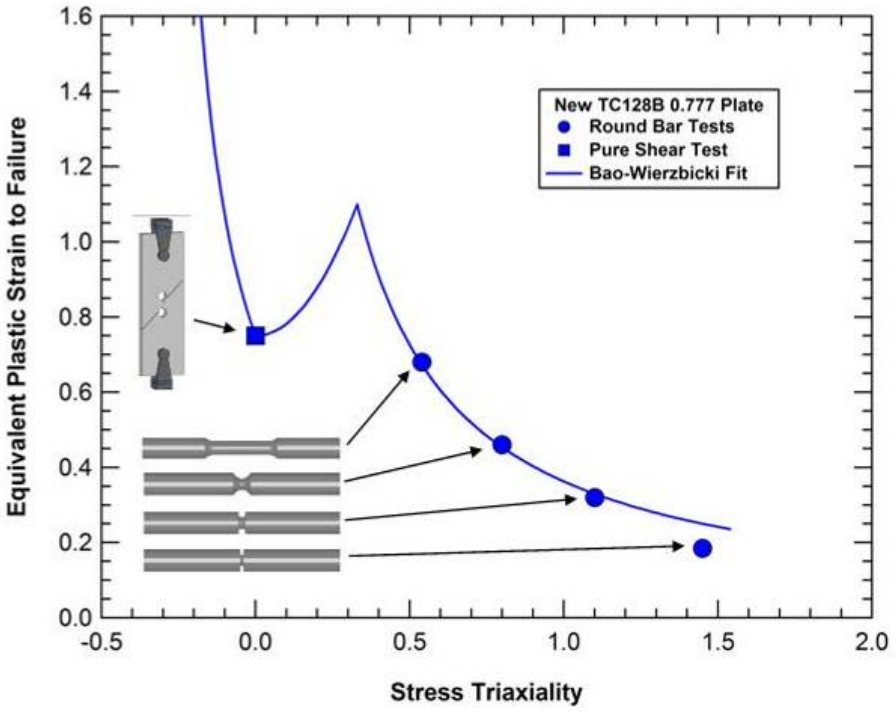

Figure 2. Bao-Wierzbicki failure surface and tests used for model calibration.

2.3.2 Modified Bao-Wierzbicki Failure Criterion

The Bao-Wierzbicki criterion was found to provide a good fit to the failure data for many of the materials tested. However, for some materials, the model as applied could not fit the failure data over the range of triaxialities tested. An example is seen in the data from three different TC128B materials tested in the NGRTC program as shown in Figure 3. The BW model provides a reasonably good fit to the data for both the Normalized 0.777 and Tank Car 3074 materials (Red and green curves and data points). However, the Tank Car 3069 material is the most ductile in the smooth round bar tensile tests (triaxiality = 0.33-0.60) and least ductile at the sharpest notched tensile test (triaxiality ≅ 1.4).

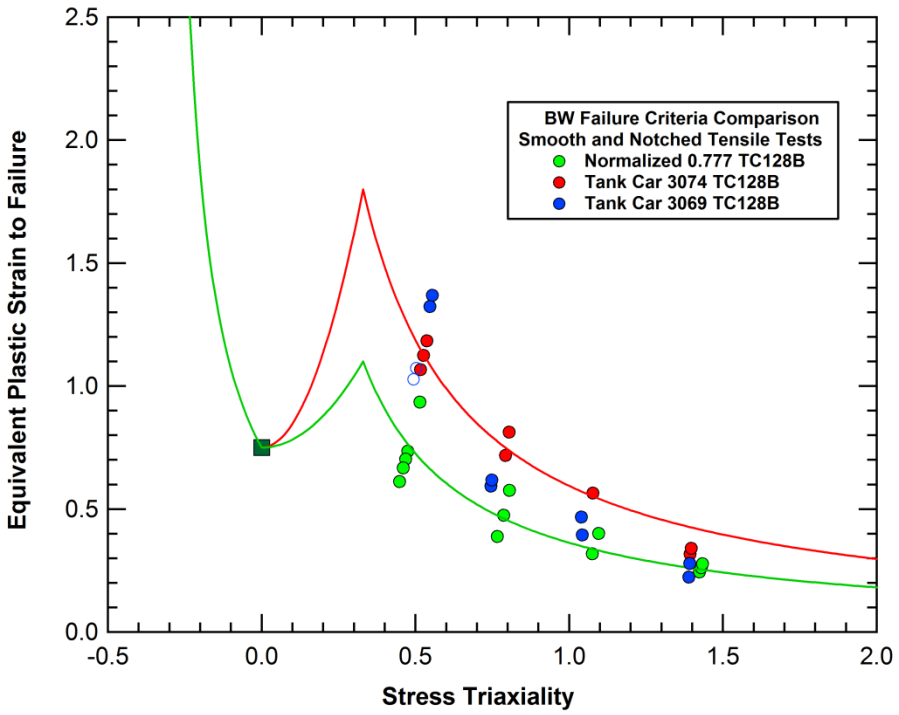

Figure 3. Bao-Wierzbicki failure surface and tests used for model calibration.

There are different approaches that can be used to obtain a better fit to the data. In the original work of Bao and Wierzbicki they allow the point at which the local maximum ductility is reached, set at the uniaxial stress triaxiality ratio of 1/3 in this study, to be a variable that is adjusted in the model. Alternatively, other ductile damage models have different functional forms for the decay in ductility at higher stress triaxialities.

In this study, we used a modified functional form for the high triaxiality branch of the damage function. This was accomplished by adding an exponent (n) to the denominator to the equation for the critical strains at high triaxiality. This modified BW damage model is provided in Equation 24.

$$\varepsilon_c\left(\sigma_{mean}/\sigma_{eq}\right)=\begin{cases}\infty & \left(\sigma_{mean}/\sigma_{eq}\right)\le -\dfrac{1}{3}\\ \dfrac{A}{1+3\left(\sigma_{mean}/\sigma_{eq}\right)} & -\dfrac{1}{3}\le\left(\sigma_{mean}/\sigma_{eq}\right)\le 0\\ 9(B-A)\left[\left(\sigma_{mean}/\sigma_{eq}\right)\right]^2+A & 0\le\left(\sigma_{mean}/\sigma_{eq}\right)\le\dfrac{1}{3}\\ \dfrac{B}{\left[3\left(\sigma_{mean}/\sigma_{eq}\right)\right]^n} & \dfrac{1}{3}\le\left(\sigma_{mean}/\sigma_{eq}\right)\end{cases} \tag{24}$$

2.3.3 Maximum Strain Failure Criterion

In this section, we explore an alternate damage modeling methodology which is called the maximum strain or critical plastic strain criterion. This is the most commonly used failure criterion applied in engineering failure analyses. This simple approach is typically applied using a critical strain value from a single source (e.g. tensile test) to determine the critical plastic strain value. The advantage of the maximum strain approach is both the ease of use and common availability in many constitutive models of most nonlinear finite element codes. Like most damage models, the maximum strain methodology has computational issues, such as mesh sensitivity, which can complicate analyses and need to be controlled.

A comparison of the Bao-Wierzbicki and maximum strain failure criteria are shown in Figure 4. The maximum strain failure criterion uses a constant value of plastic strain for failure for all stress states. As a result, we would expect the maximum strain failure criterion to be more ductile than the BW criterion in some loading conditions (e.g. high triaxiality notched tensile tests and shear tests) and less ductile in other loading conditions (e.g. compression).

To evaluate the Maximum Strain Approach (MSA), the maximum strain criterion was used to simulate the TC128B material tests from the NGRTC program using the existing FE models. The results were compared to the results to the test data and BW model simulations to assess the performance of the MSA model for tank car puncture applications.

The methodology that was applied is:

1. Recover archived NGRTC models of the laboratory material tests for the tensile, notched tensile, tensile-shear, and punch tests on the TC128B material.
2. Convert the BW constitutive model used in the NGRTC program for TC128B to be a model controlled by a maximum strain failure criterion.
3. Calibrate the critical maximum strain value to match the data on the tensile tests.

4. Use the calibrated value to assess the failure modeling performance in the high-triaxiality (Notched tensile: 3 configurations)) and low-triaxiality (tensile-shear: 7 configurations) stress regime tests. Similarly the punch shear tests (3 configurations) will be analyzed and compared to analyses with the BW model.
5. Document the comparisons of the BW and MSA approach for the laboratory tests and identify areas where discrepancies occur.

The two constitutive models being applied in this assessment are identical up to the point of failure. The only difference in the two approaches is in the criterion used to determine the point at which the material fails.

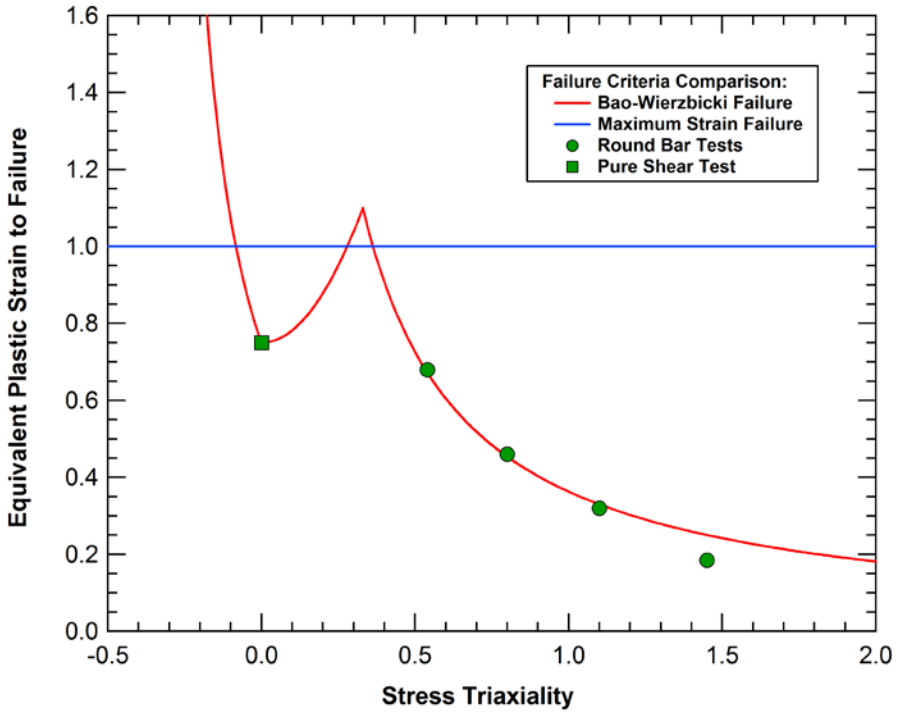

Figure 4. Comparison of the Bao-Wierzbicki and maximum strain failure criteria.

Simulations of the smooth round bar tensile test with the BW and maximum strain criteria are compared to the measured tensile response in Figure 5. Overall there is good agreement between the calculated and measured stress-strain behavior and elongation at failure with both models. However, this is expected since the critical plastic strain value (plastic strain of 1.0) was selected to match in this test condition. We see in Figure 4 that the critical strain value is slightly below the value in the BW criterion at a uniaxial stress loading condition (triaxiality=0.333). However, as the specimen starts to neck the triaxiality increases and the critical BW- strain value in the necked region would drop below maximum strain value. Thus the average value in the simulation for the BW model is close to the critical plastic strain value.

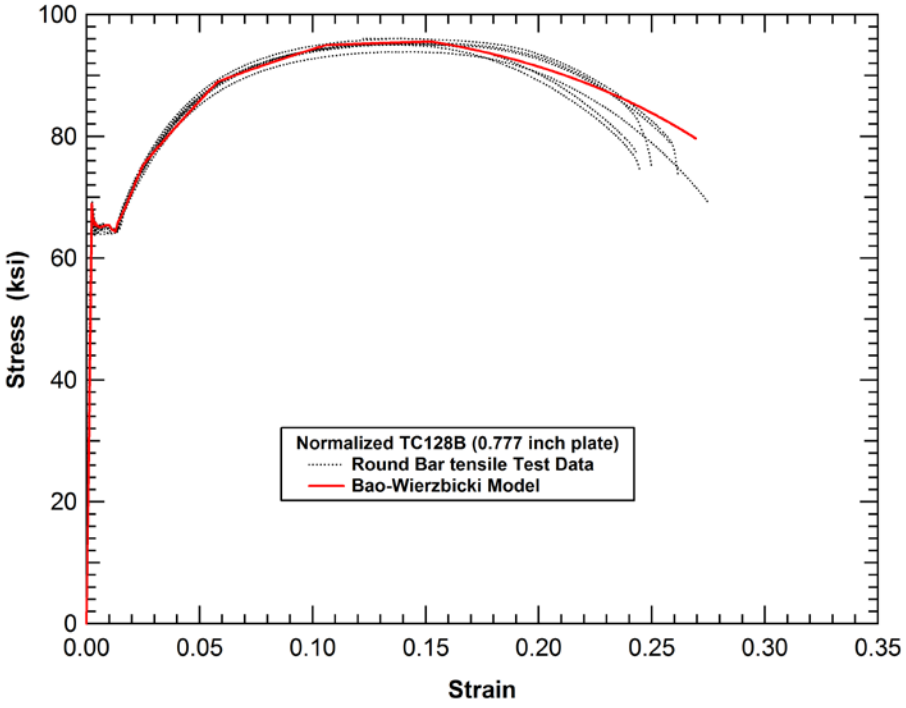

(a) Bao-Wierzbicki failure model

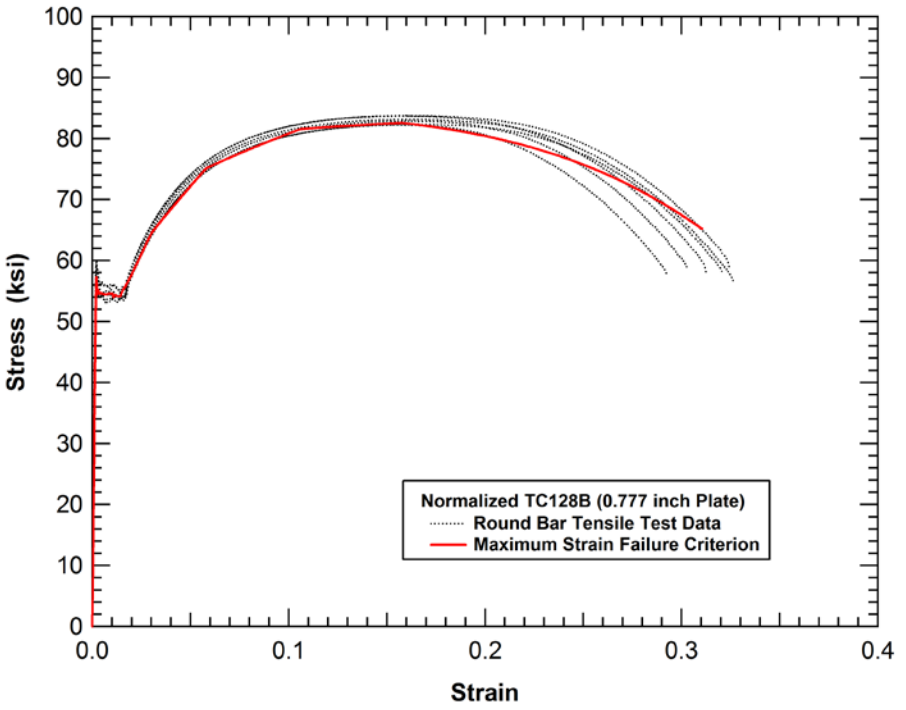

(b) Maximum strain failure model

Figure 5. Comparison of the tensile test analyses with different failure criteria.

Simulations of the notched round bar tensile test with the BW and maximum strain criteria are compared to the measured tensile response in Figure 6. There is good agreement between the calculated and measured stress-strain behavior and elongation at failure with the BW model, shown in Figure 6(a). However, the analyses with the maximum strain criterion significantly overpredict the ductility of the notched tensile tests compared to the measured behavior. This is not surprising since the critical plastic strain value (plastic strain of 1.0) is significantly above that of the BW criterion for the high triaxiality states of these notched tests (triaxiality values of 0.7-1.4).

Similar simulations of the tensile-shear tests with the BW and maximum strain criteria are compared to the measured tensile response in Figure 7. Again, there is good agreement between the calculated and measured stress-strain behavior and elongation at failure with the BW model, shown in Figure 7(a). However, the analyses with the maximum strain criterion significantly overpredict the ductility of the tensile-shear tests compared to the measured behavior. This is not surprising since the critical plastic strain value (plastic strain of 1.0) is above that of the BW criterion for the low triaxiality states of the shear tests (triaxiality values of 0.0-0.3).

The above comparisons of the maximum strain criterion clearly indicate that there are some loading conditions where the MSA does not accurately predict the failure of the material. However, there are also applications where the simpler maximum strain criterion is sufficiently accurate. The final comparison of the two failure criteria is for the blunt side impact puncture respose of tanks. When we compare the analyses of tank puncture performance using the BW and maximum strain failure criteria we get very similar behaviors, as shown in Figure 8. The puncture forces are quite similar with slightly higher forces calculated for the BW failure criterion for the smaller impactors. The puncture energies are also similar with the exception of the 6x6 impactor where a slight increase in the puncture force allowed some late time tank kinematics to be included and this increases the calculated puncture energy by approximately 30% for this case. However, this result is specific to the details of the impact kinematics and would not be typical for most other scenarios (e.g. different impact speed). Note that for the impact behaviors analyzed, the strain rates are relatively low and strain rate effects were not included in the models. This approach is consiustent with the previous tank car puncture analysis programs [e.g. 1].

A closer inspection of the impact calculations explains why the two failure criteria are in reasonable agreement for the tank puncture analyses. The failure typically initiates on the inside surface of the tank under the impact zone where the metal is deformed in tension. At these locations, the stress triaxiality is typically in the range between 0.5 and 0.7 for a variety of impactors and tank impact scenarios as shown in Figure 9 through Figure 11.

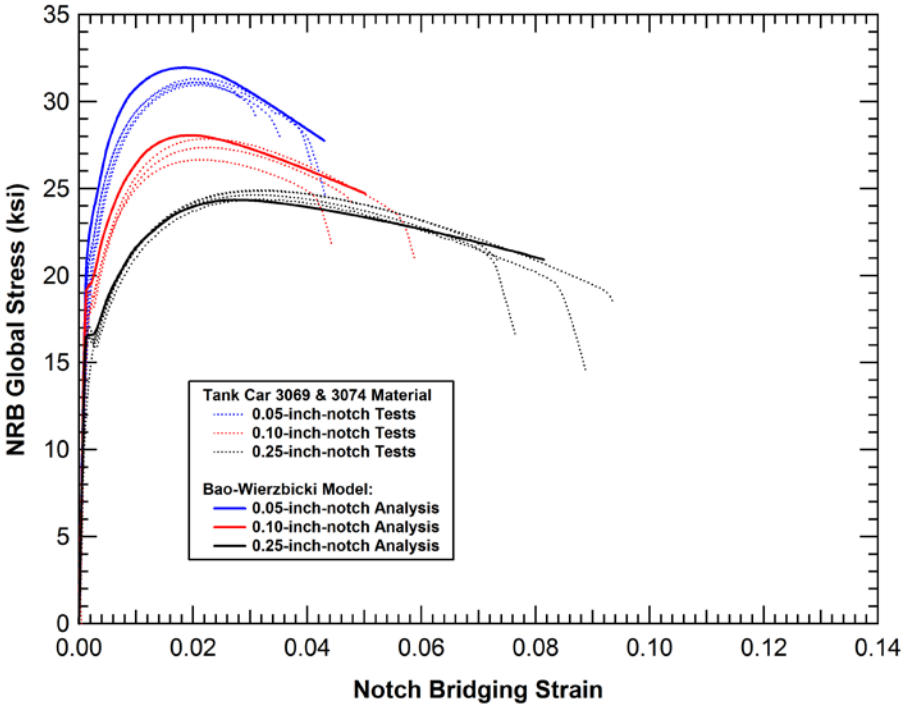

(a) Bao-Wierzbicki failure model

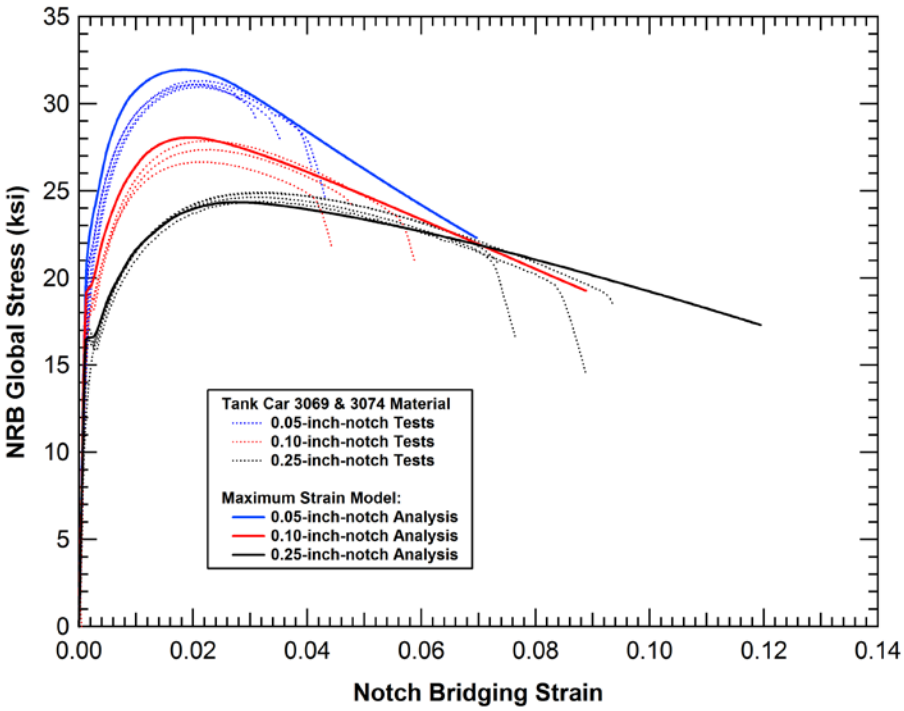

(b) Maximum strain failure model

Figure 6. Comparison of notched round bar tensile tests with different failure criteria.

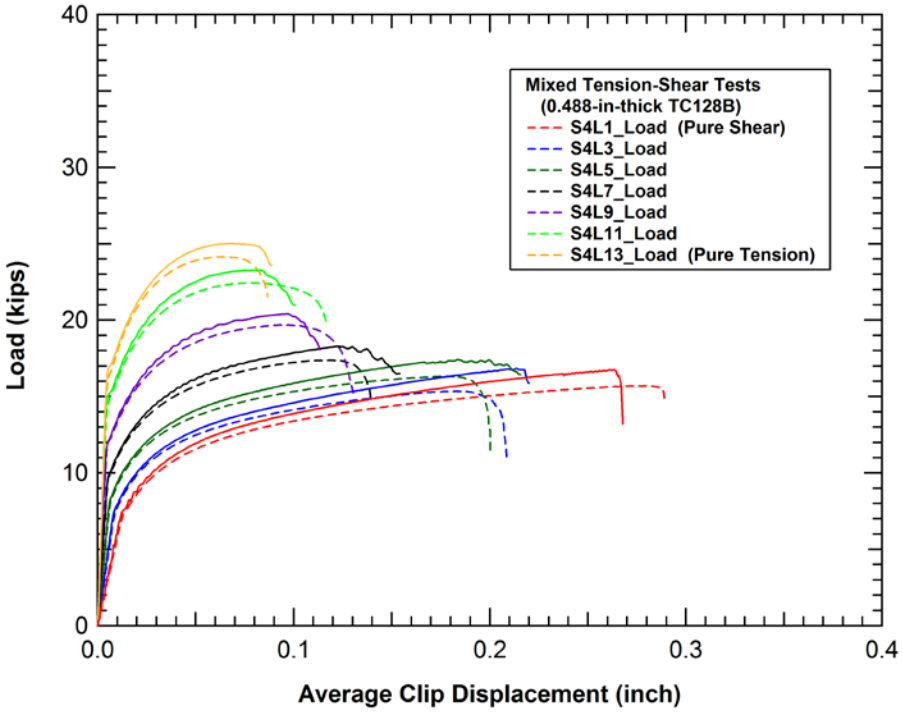

(a) Bao-Wierzbicki failure model

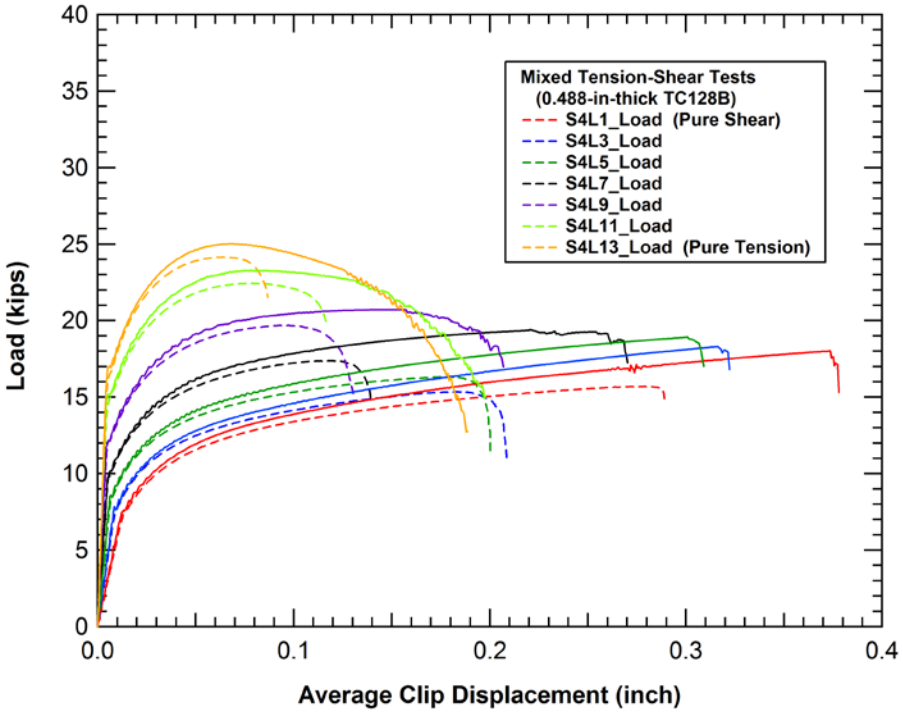

(b) Maximum strain failure model

Figure 7. Comparison of the tensile-shear test analyses with different failure criteria.

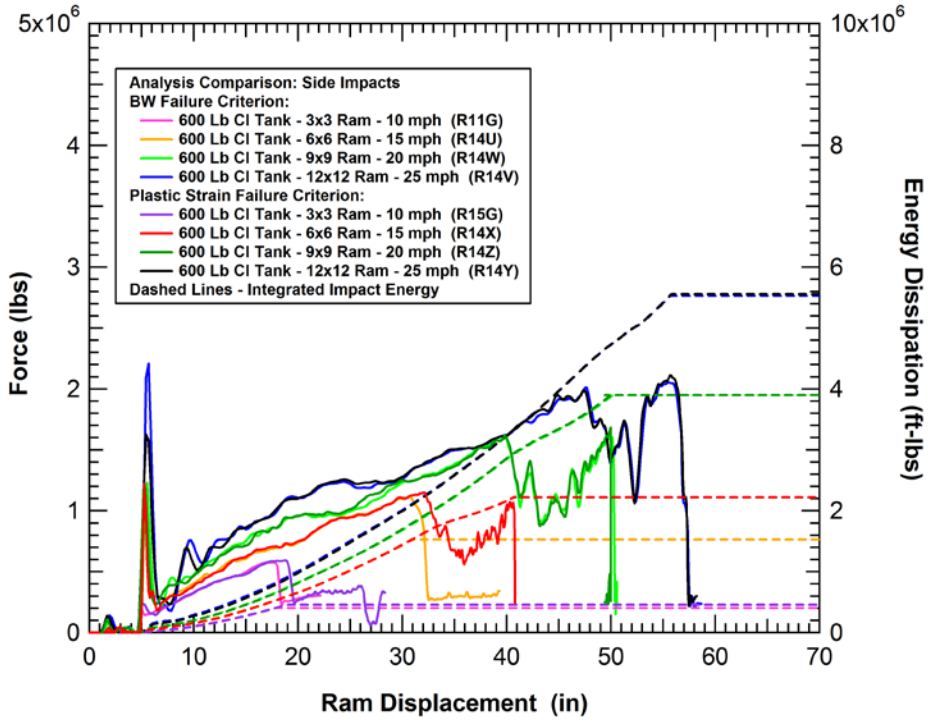

Figure 8. Comparison of tank car puncture analyses with different failure criteria.

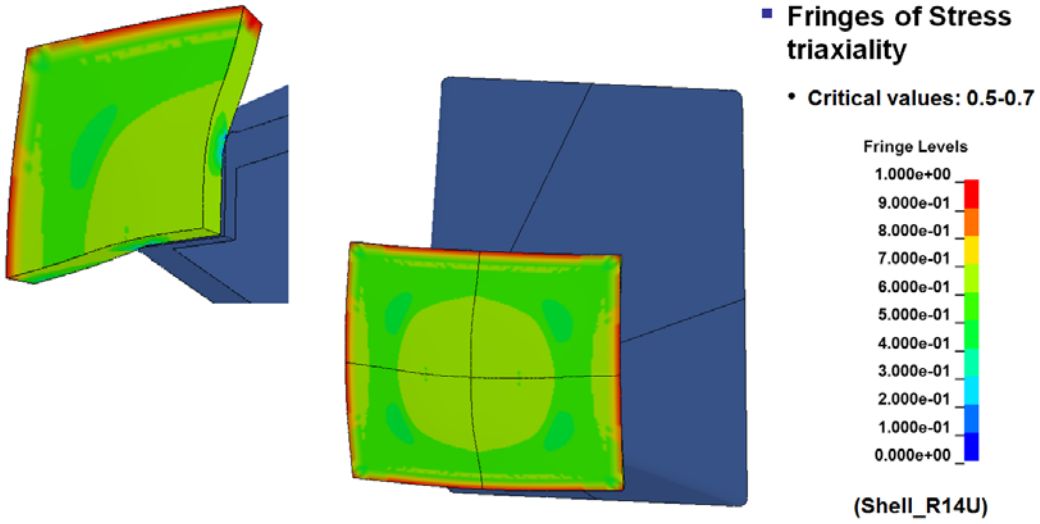

Figure 9. Calculated stress triaxiality in the impact zone for a 6x6-inch side impact.

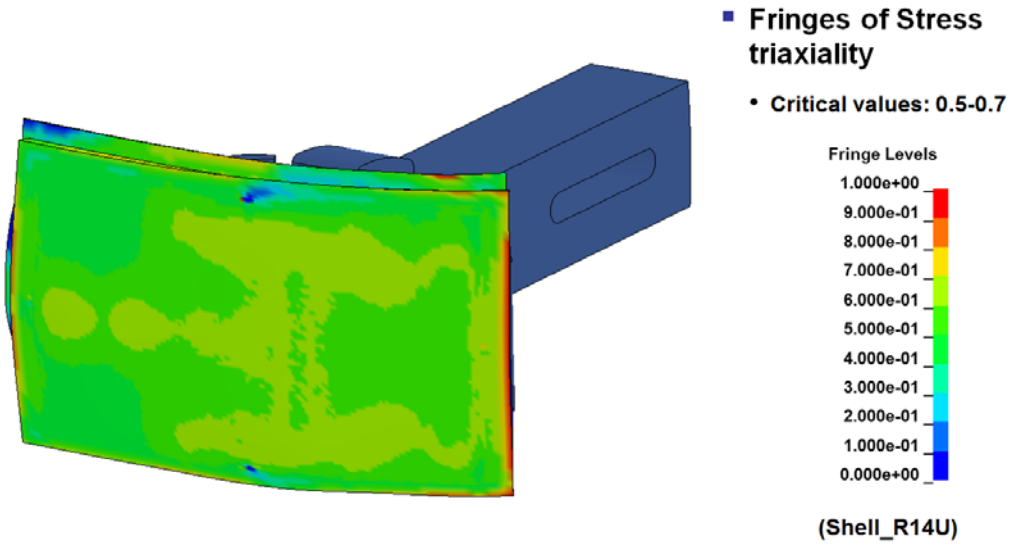

Figure 10. Calculated stress triaxiality in the impact zone for a coupler side impact.

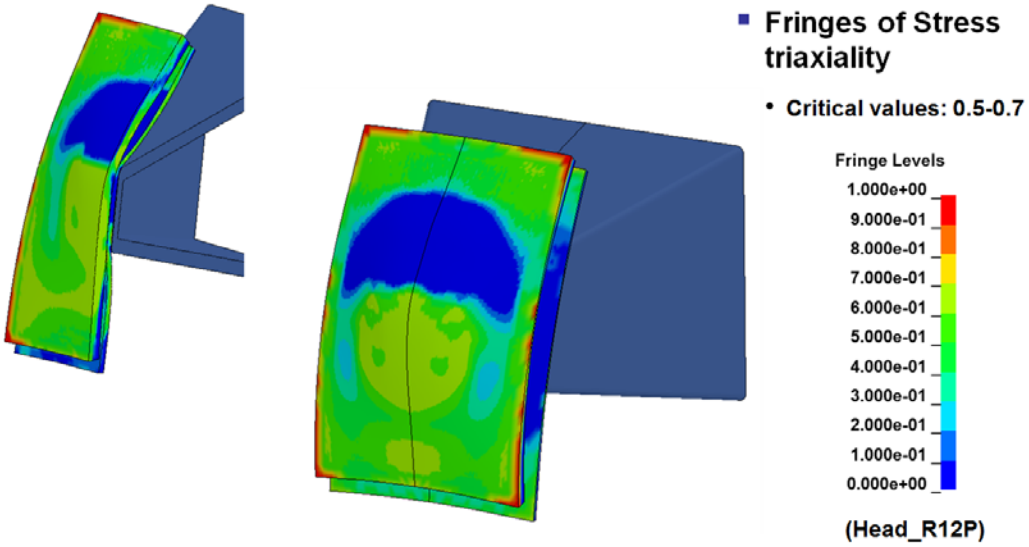

Figure 11. Calculated stress triaxiality in the impact zone for a 6x6-inch offset head impact.

Although the prediction of the tank punctures occurs at similar levels with the BW and critical strain criteria, the comparison of analyses show an important difference. The predicted damage in the impact zone for the 6x6 offset head impact with the BW and critical strain failure criteria are shown in Figure 12, and Figure 13, respectively. The BW model predicts that the failure initiates on the inside surface of the tank (dominated by tensile deformations). In contrast, the

maximum strain criterion predicts that the failure initiates on the outer surface of the tank in a region dominated by compressive stress states during deformation.

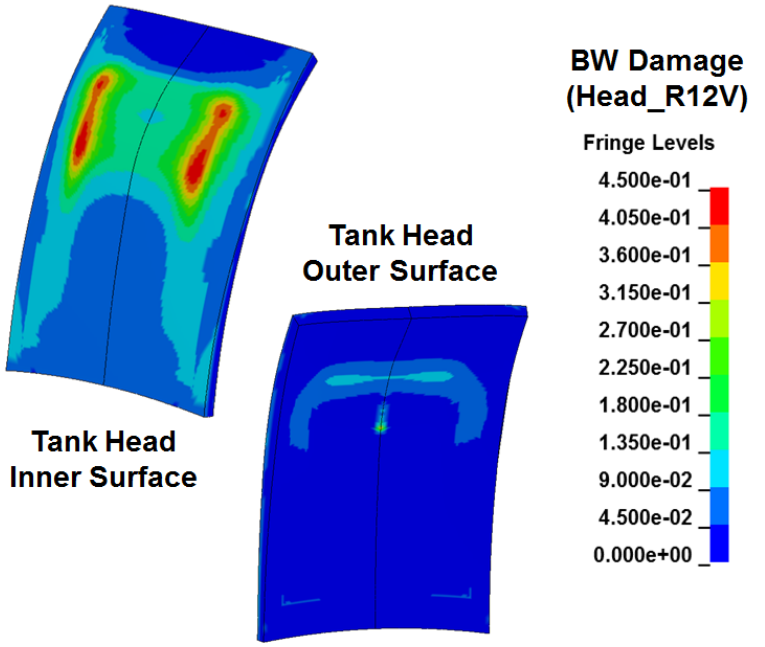

Figure 12. Calculated tank head impact damage with the Bao-Wierzbicki failure criterion.

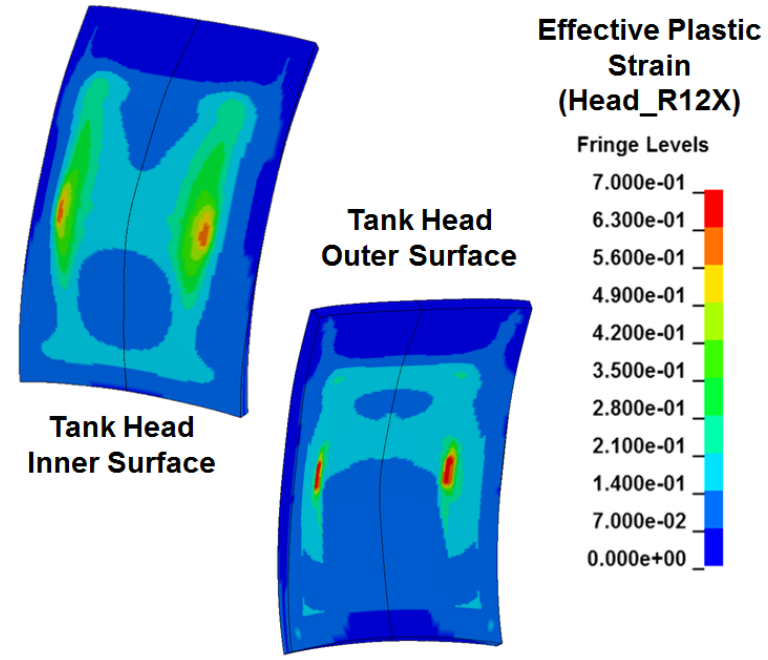

Figure 13. Calculated tank head impact damage with the maximum strain failure criterion.

2.3.4 Gurson-Tvergaard Failure Criterion

The damage model applied for puncture analyses in the NGRTC program was the Bao-Wierzbicki (BW) model. An alternate failure model applied in a series of analyses for the Chlorine Institute was the Gurson-Tvergaard (GT) model [9]. An illustration of the GT failure criterion compared to the BW failure criterion is shown in Figure 14. The model has the characteristic of capturing the reduction in ductility for the high triaxiality stress conditions. As applied in Reference 9, the emphasis of the material evaluations was on the high triaxiality material ductility. In that study, various materials were characterized by, and the material models were fit to, Charpy impact test results.

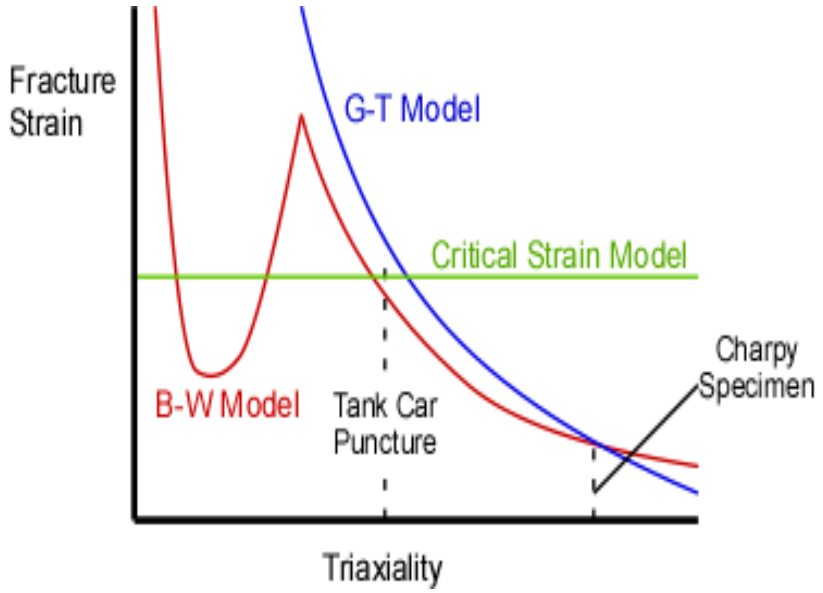

Figure 14. Comparison of the Gurson-Tvergaard, Bao-Wierzbicki, and maximum strain failure criteria.

Since the completion of that effort, two different aspects of this approach have been reconsidered. The first is that the assumption that the entire damage curve scales with the ductility in the Charpy impact test may not be accurate. The models that are fit to the variability in the Charpy energy may not be appropriate to assess the difference in puncture behavior. This is the effect that required development of the Modified Bao-Wierzbicki damage model described in Section 2.3.2. The variability in Charpy impact test ductility is not proportional to the ductility in tensile behaviors.

The second aspect of the G-T model is that researchers have identified that it does not accurately capture the ductility of a model for low stress triaxiality levels [e.g. 44-47]. As a result, the G-T model was not further examined in this study.

2.4 Data Reduction Procedures for Material Characterization Test Data

A tabular stress-strain curve was developed based on testing of different samples of TC128B [1, 2]. A series of standard tensile tests were performed on different batches of TC128B, as shown in Figure 15. The data is consistent within each batch of material but significant variation can be found in tank car material obtained from different sources. The new material that was tested was at the upper range of strength for TC128B and the material recovered from the tank cars used in the test were more consistent with previous test data [48, 49]. As a result, the material recovered from the tank car used as the Test 2 target vehicle was used as the baseline material for the analyses in this report.

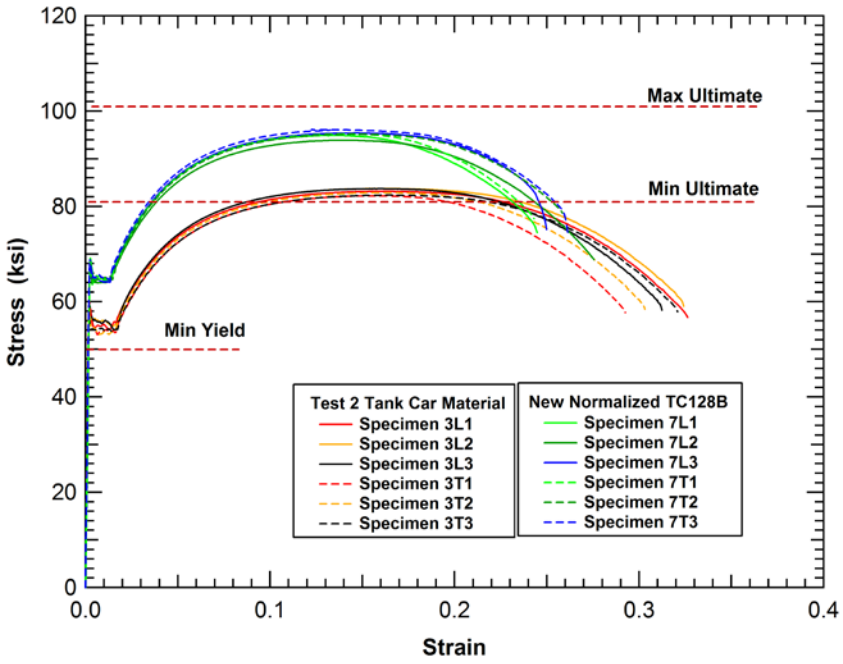

Figure 15. Material testing data for different TC128B materials.

The data shown in Figure 15 is the measured engineering stress-strain behavior. Engineering stress was obtained by dividing the measured loads by the original cross-sectional area of the specimen. Similarly, engineering strain was obtained by dividing the change in the specimen gauge-section length by the original length.

The constitutive model in the finite element analyses requires that the engineering data be converted to a true stress and true strain. This conversion accounts for the changing cross section of the specimen as it was deformed. The specimen cross section changes (shrinks) significantly during the test, and the engineering stress does not yield the "true" stress in this cross section. Similarly, the engineering strain is not representative of the material behavior, especially when a general three-dimensional state of strain exists. As a result, the engineering

stress decreases as some materials approach failure, implying a weakening of the material. In reality, the stress in the cross section is increasing due to the reduction in the cross-sectional area (i.e. necking).

There are several different ways to measure stress and strain based on the coordinate system used [20]. Some are based on material (Lagrangian) coordinates and some on spatial (Eulerian) coordinates. These give rise to terms such as "Green" and "Almansi" strain tensors. These are important in writing a computer code to solve large strain problems. An alternate approach is to define a "true" or "natural" stress and strain. The true stress is based on the load divided by the actual cross-sectional area of the specimen and is equal to the engineering stress multiplied by a term to correct for the change in cross section.

$$\sigma_T = \sigma_{eng}(1+e) \tag{25}$$

where σ_T and σ_{eng} are the true and engineering stresses, respectively, and e is the engineering strain.

Prior to the onset of localization (necking), the natural or true strain, ε_T, is defined as

$$\varepsilon_T = \ln(\frac{l}{l_o}) = \ln(1+e) \tag{26}$$

This definition comes about from defining the incremental true or "natural" strain as the current "change in length" divided by the current length, or

$$d\varepsilon_T = \frac{dl}{l} \tag{27}$$

This is in contrast with the definition of engineering strain that references the change in length, Δl, divided by the original length, l_0, or

$$e = \frac{\Delta l}{l_0} \tag{28}$$

After the onset of localization, the determination of the true strain in the necked region becomes more complex and requires measurement of the local neck geometry.

The TC128B engineering test results are compared to the converted true stress and true strain data in Figure 16. The true stress curves from the tests do not include a correction for the necking behavior. As a result, they are only valid up to the onset of necking at a true strain of approximately 15%. The actual true-stress and true strain curves for the material continue to strain harden throughout the loading if the effects of necking were corrected. An extrapolated

true stress curve that corrects for the effects of the necking behavior is added to Figure 16 (solid black line). It is this extrapolated curve that is used in the material constitutive model.

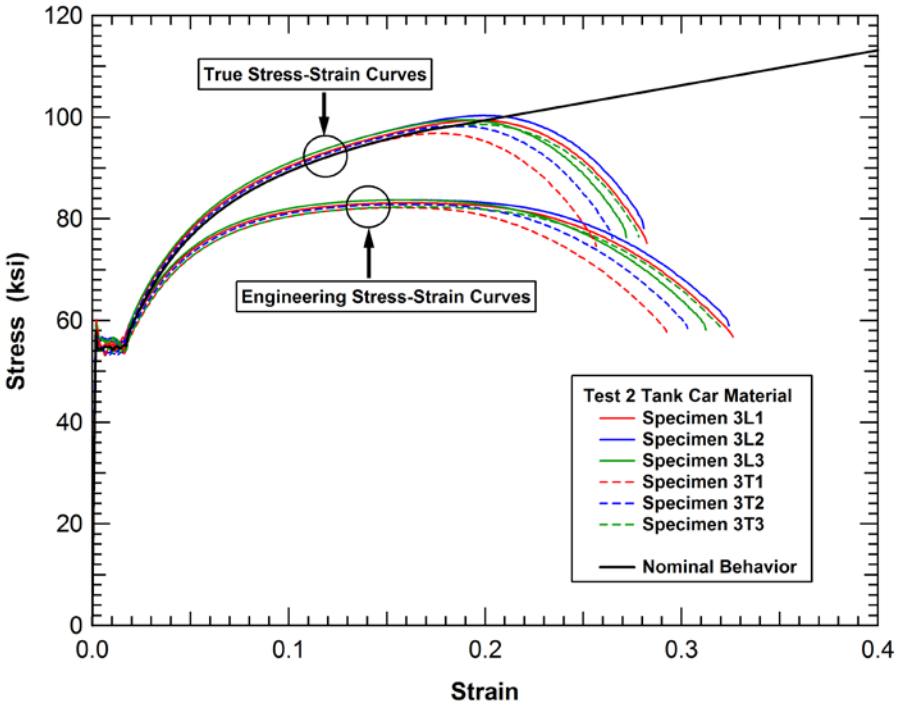

Figure 16. Comparison of engineering and true stress-strain data for TC128B.

The final step in obtaining the tabular stress-strain parameters for the TC128B constitutive model was to fit a smooth set of points to the extrapolated true-stress data. This final tabular fit for the TC128B is shown in the true stress versus plastic strain curve in Figure 17. The specific values for the tabular stress-strain curve are also listed in Table 1. As a validation that this curve accurately captures the true stress-strain behavior of the material, a tensile specimen model was generated and the constitutive parameters were applied to simulate the tensile test response. The calculation was analyzed to determine the engineering stress-strain behavior consistent to the tests (e.g. using equivalent gauge section length). A plot of the calculated engineering behavior compared to the test data is shown in Figure 18. The data shows that the constitutive parameters accurately reproduce the material behaviors including the onset and development of necking in the specimen.

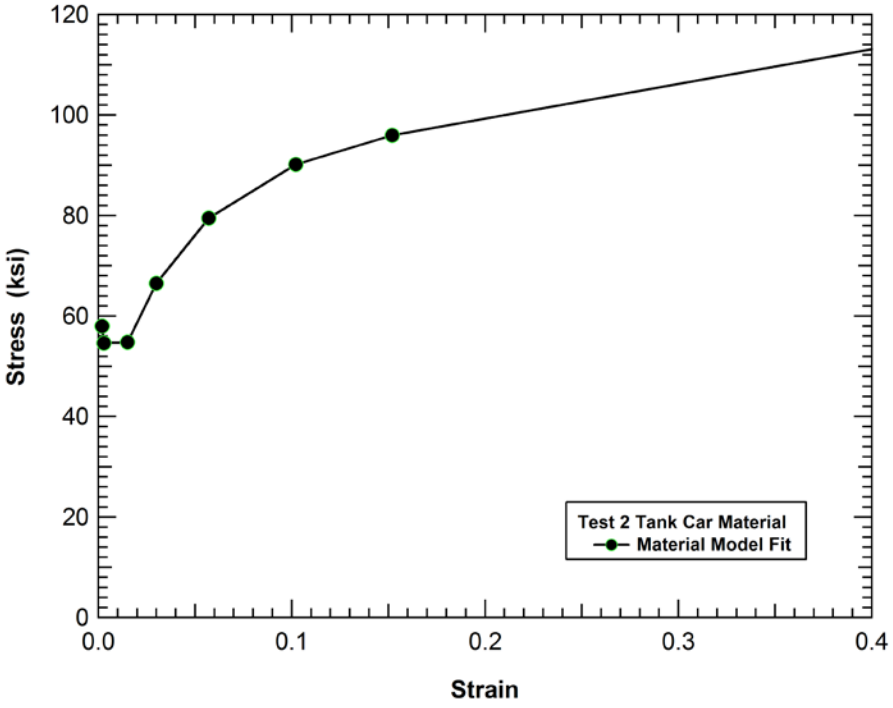

Figure 17. Tabular true stress curve developed for the TC128B constitutive model.

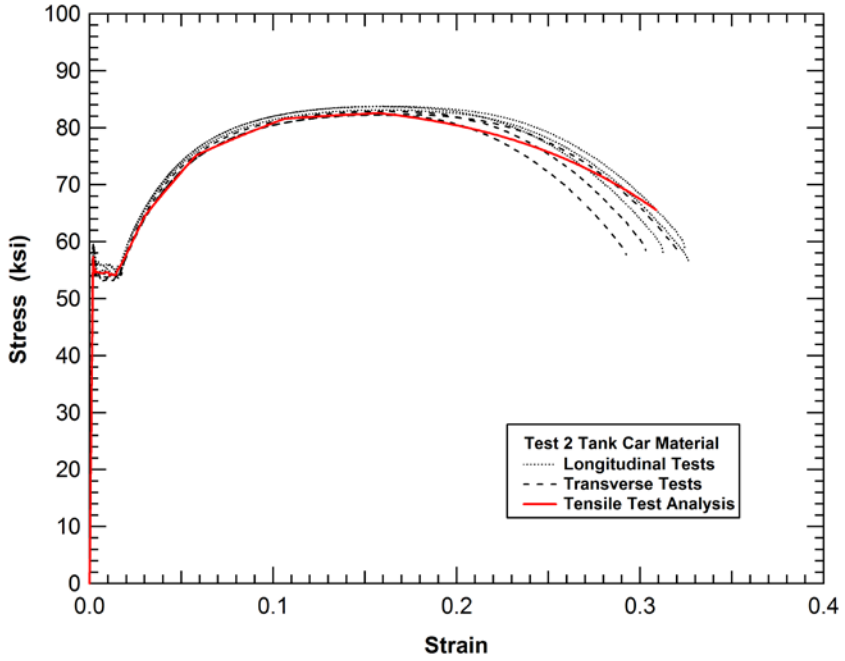

Figure 18. Comparison of the measured and calculated TC128B tensile test.

Table 1. Tabular TC128B stress-strain curve values

Point No.	Plastic Strain (in/in)	True Stress (ksi)
1	0.00e+00	58.0
2	8.22e-04	54.6
3	1.30e-02	54.8
4	2.76e-02	66.5
5	5.41e-02	79.5
6	9.87e-02	90.2
7	1.49e-01	96.0
8	1.15e+00	165.0

The above procedure is that used for fitting the true-stress-true strain behavior for a model using the von Mises yield criterion. The Drucker Prager model requires use of additional data at different levels of stress triaxiality (e.g. notched tensile data). Consider the data reduction of the 0.777-inch-thick normalized TC128B material from the NGRTC Program [1]. An initial data reduction was applied using the von Mises model methodology described above and a comparison of the tensile test data to the simulation of the tensile test is shown in Figure 19. The overall agreement for the tensile test behavior is good. However, when we use the same model with the von Mises yield criterion to simulate the notched tensile tests we get the correlation shown in Figure 20. The model with the von Mises yield criterion significantly over predicts the measured test loads, especially for the sharper notch radii.

The error in the calculated versus measured load levels for the sharper notch tensile tests, combined with knowledge of the triaxiality levels in the various tests, can be used to calculate an estimate of the Drucker Prager coefficient (α in Equation 21, Section 2.2.3). The stress triaxiality versus plastic strain paths for the various tensile tests are shown by the dashed lines in Figure 21. The uniaxial tensile test starts with a triaxiality of 0.33 and the triaxiality increases as the specimen starts to neck (localized in the failure zone) to a maximum value of approximately 0.5. By comparison, the sharpest notched tensile test has an average triaxiality of approximately 1.4. Thus the notch results in a much larger tensile mean stress in the specimen gauge section.

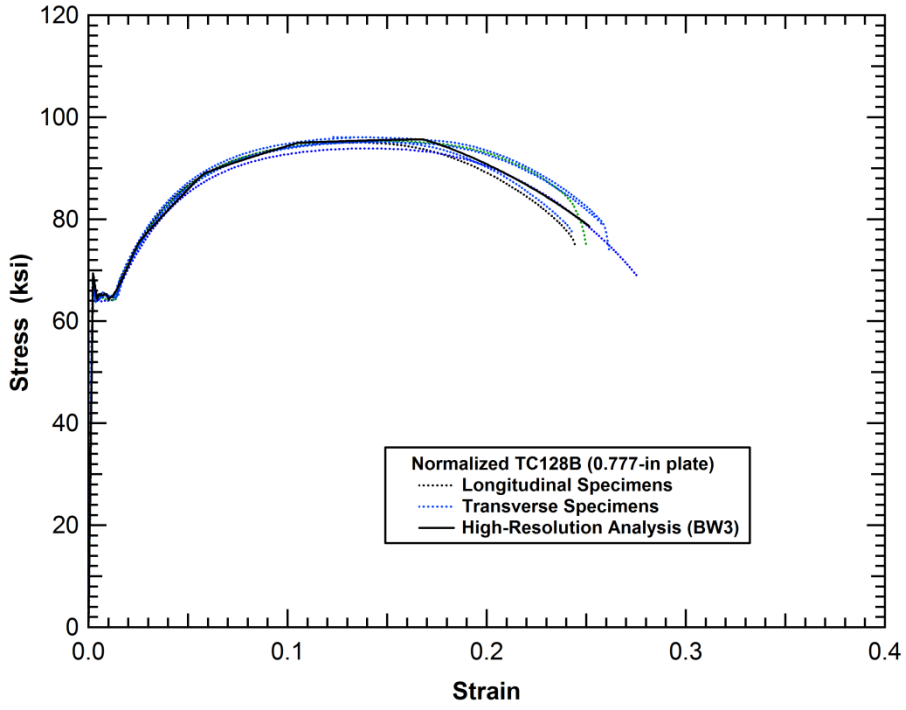

Figure 19. Comparison of Tensile test data and analysis for 0.777-in-thick TC128B using a von Mises yield criterion.

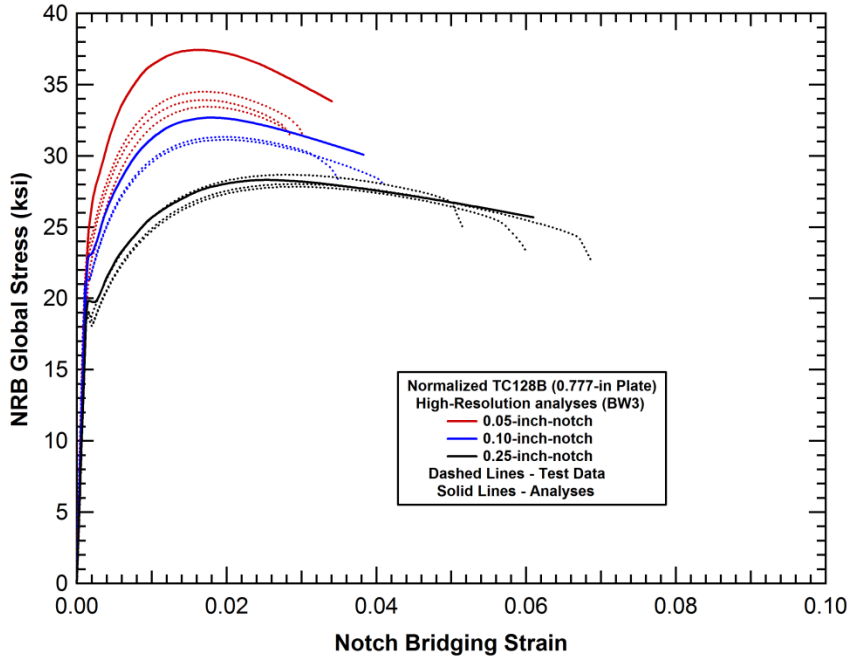

Figure 20. Comparison of notched tensile tests and analysis for 0.777-in-thick TC128B using a von Mises yield criterion.

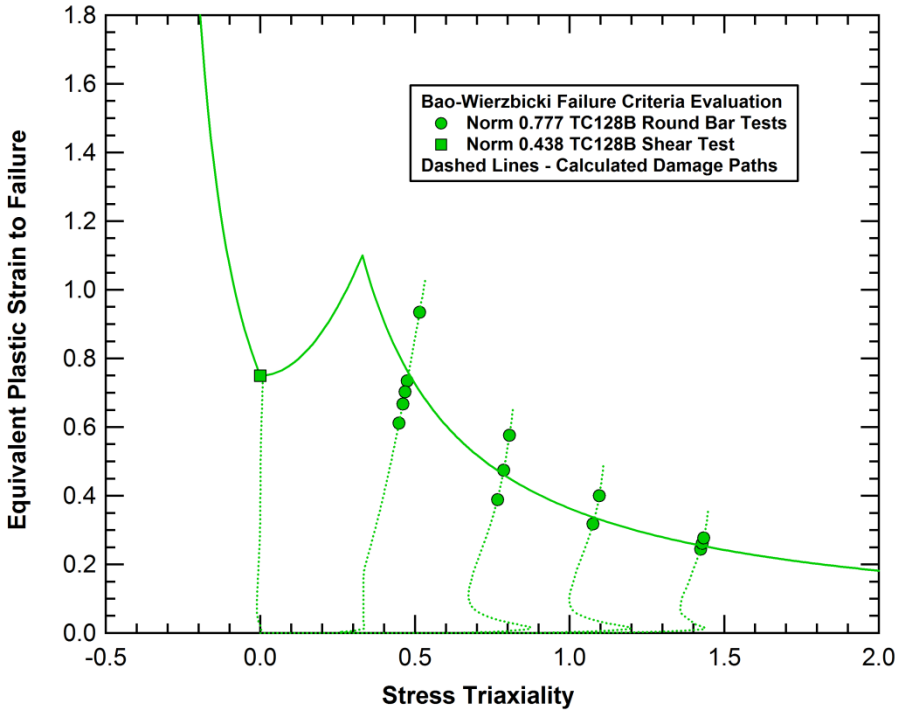

Figure 21. Calculated stress-strain paths for the notched tensile tests on 0.777-in-thick TC128B.

After the Drucker Prager coefficient has been determined, the true-stress true-strain curve used in the constitutive model needs to be corrected to match the uniaxial tensile data. At times, some additional adjustment is needed to ensure the model correctly predicts the behavior through necking. However, when the parameters have been correctly determined, the model can predict the behaviors significantly better over the range of stress states in the tests.

A comparison of the measured and calculated tensile test results for the normalized 0.777-in TC128B material using the Drucker Prager yield function (α=0.195) is shown in Figure 22 and Figure 23. The comparisons show good agreement for all levels of confinement (strength and ductility).

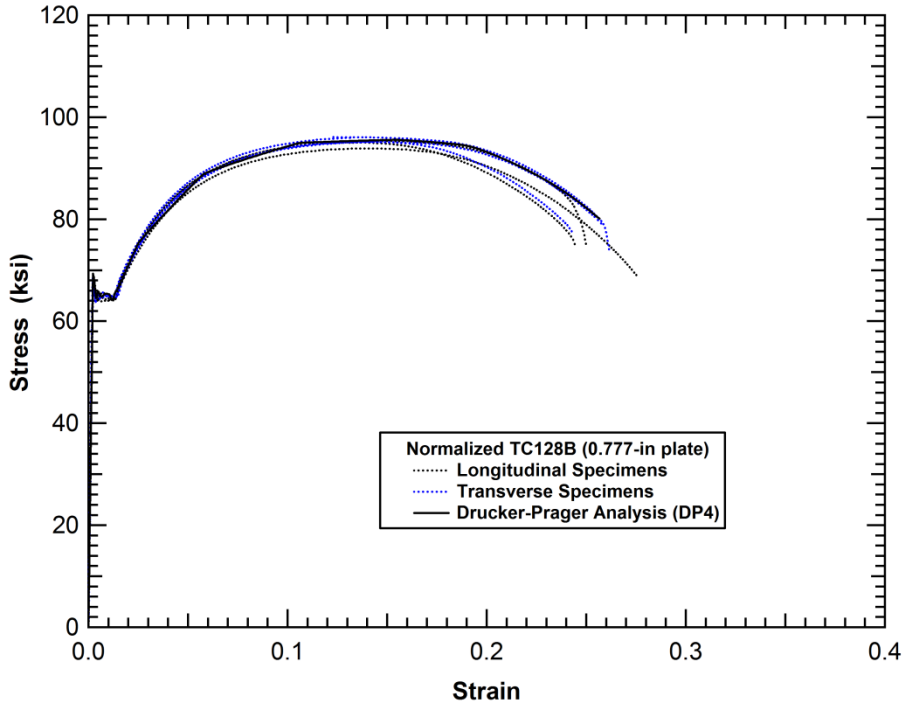

Figure 22. Comparison of Tensile test data and analysis for 0.777-in-thick TC128B using a Drucker-Prager yield criterion.

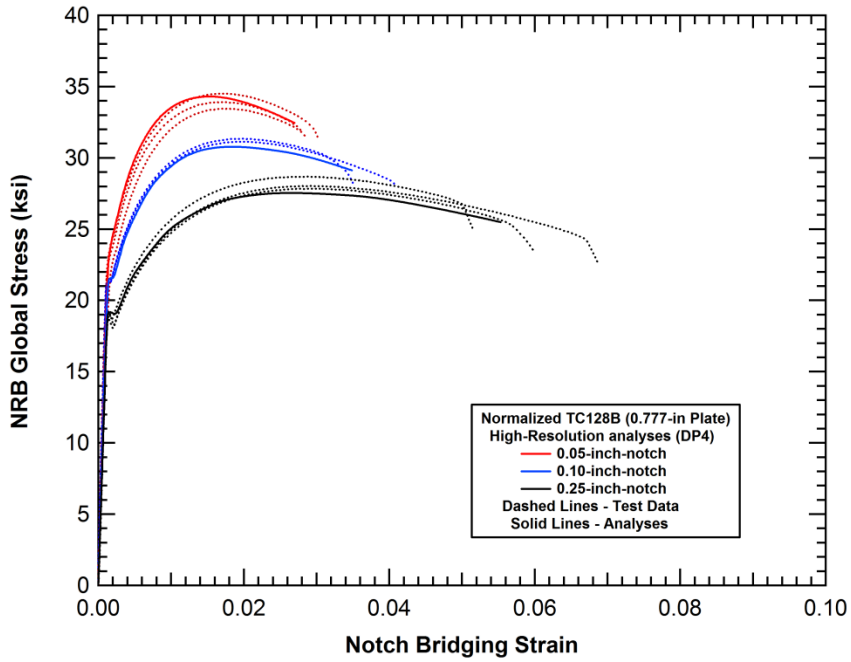

Figure 23. Comparison of notched tensile tests and analysis using a Drucker-Prager yield criterion.

3 Material Characterization Testing and Analyses

3.1 Testing Overview

The first step in the development of a constitutive model is the development of the nonlinear stress strain behavior. This governs the mechanical response of the material and prescribes the internal forces (stress) that are developed as the material is deformed (strained).

The purpose of this section is to provide a complete description of the materials testing performed and the methods employed. Testing was performed on seven different steel material lots during two distinct testing phases. Of the seven materials, four were nominally TC128B with three other different steel alloys. The initial first Phase I focused on a typical TC128B and the other three medium strength steels. During the second Phase II testing, the focus was on TC128B with lower levels of sulfur in the composition of the material (nominal TC128B limits sulfur concentration to 0.015% by weight). The testing performed in the two phases was similar, although high rate tensile tests in Phase I were replaced with notched shear tests in Phase II.

Sulfur is not a deliberate addition into TC128B material; rather it occurs at differing levels depending upon the cleanliness of the material, the source of the melt and the methods used during compositional refinement. The role of sulfur in TC128B is evident from Heitmann et al[1] who reports significant improvements in transverse CVN (Charpy v-notch) fracture toughness at lower and upper shelf temperatures with low sulfur concentrations (<0.006%). It is anecdotally reported that the modern steelmaking process has resulted in significant improvements in alloy cleanliness, with decreased sulfur concentrations resulting as a benefit of this.

A recent report[2] clearly illustrates high sulfur concentrations are apparent in older rail tank cars. As part of this report, TC128B composition was examined in 28 retired tank cars built between 1965 and 1999, with 80% of these fabricated prior to 1980. The reported sulfur weight percent values for TC128B were 67% with sulfur <0.03% (only 14% of the total with ≤0.01%) and 33% with sulfur ≥0.03%. Clearly the vast majority of these levels exceed the typical sulfur weight percent of ≤0.01% produced in modern steels today.

[1] Heitmann, W.E., Feher, F.C., Hybinette, C. and Manohar, M., "The Influence of Sulfur Concentration Below 0.006% Along With Sulfide Shape Control on the Charpy V-Notch Properties of Normalized and Stress Relieved TC128 Grade B Steel Plate,"STEEL: 4th International Symposium on Railroad Tank Cars, Sept. 2007, Detroit MI, Materials Science and Technology (MS&T) 2007.
[2] McKeighan, P.C., "Mechanical Properties of Tank Car Steels Retired from the Fleet," Southwest Research Institute Project No. 18.12240, Foster-Miller Subcontract SUB3-00022, DOT Volpe Contract No. DDTS.060183.000.801, June 2007.

3.1.1 Material

The ideal material for this evaluation would have both a range of strengths as well as upper shelf toughnesses. For Phase I, materials for this work were donated by Union Tank Car in conjunction with characterizations being performed at Miner Enterprises (Geneva, IL). The specific alloys and materials included in this study are detailed in Table 2 and include the following:

- TC128B: rail tank car steel (0.75-inch thick),
- A709-Gr. HPS100W: moderate strength bridge steel (1-inch thick),
- NUCU: a higher strength bridge steel, nominally ASTM A710-GrB (0.5-inch thick), and,
- A514-GrB: current higher strength bridge steel (0.75-inch thick).

Table 2. Material donated by Union Tank Car for the Phase I evaluations (rolling direction parallel to the short, 8-inch, dimension of the plates).

Material	No. of Pieces	Size of Piece (inch)	Thickness (inch)
A709-Gr. HPS100W	3	8 x 12	1.0
NUCU steel (A710-Gr B)	3	8 x 12	0.5
A514-Gr B	2	8 x 12	0.75
TC128B normalized	2	8 x 12	0.75

All of these materials were supplied in the normalized condition. The motivation for the Phase II testing was due to increasing interest in the rail tank car community to utilize the improved toughness low sulfur steels combined with the fact that the Phase I TC128B material had a high level of sulfur present.

Phase II materials included three different TC128B heats donated by SSAB, Arcelor Mittal and Trinity Industries. A description of these three heats of TC128B is shown in Table 3 and can be summarized as follows:

- TC128B – nominal sulfur content (“A-material”) flat plate,
- TC128B – ultra-low sulfur content (“S-material”) flat plate,
- TC128B – ultra-low sulfur content (“T-material”) curved plate extracted from a tank car undergoing fabrication.

All materials were nominally supplied in the normalized condition, although the Trinity material was remnants from tank car production (the cutout from the manway). Hence this plate had been formed into one of the rings that make-up the tank car. Due to this deformation, this plate was subjected to a post-weld heat treatment (PWHT) prior to testing by Arcelor Mittal during the material characterization phase. This PWHT cycle was performed in accordance with AAR M-1002, Appendix W, paragraph 16 guidelines. It was heated from room temperature to 1150°F, held for 1 hour, and furnace cooled until 800°F when it was subsequently removed and air cooled.

Table 3. TC128B material donated by various sources for the Phase II evaluations.

Material Source	Material Descriptor	Prefix Identifier	Size of Piece (inch)	Thickness (inch)	Known Pedigree
Arcelor	nominal sulfur	A-material	12 x 12	0.729	Arcelor heat no. 812A38770
SSAB	ultra-low sulfur	S-material	8 x 12	0.505	SSAB heat no. W2L567
Trinity	ultra-low sulfur	T-material	8 x 11	0.729	Manway cutout subsequently PWHT, originally produced by Arcelor heat no. 821Y13090

The rolling directions for the different materials were all marked on the plates received.

3.1.2 Pre-Test Material Characterization

Before a more extensive test program ensued, some basic material characterization was performed on the seven different heats of steel. This is important to ensure that the plates meet specification and exhibit expected behavior prior to embarking on a more extensive testing effort. This basic characterization work included alloy elemental composition measurements, plate hardness measurements, and room temperature longitudinal and transverse CVN fracture toughness.

The chemical compositions of the three non-tank car steels is shown in Table 4 and the TC128B heats in Table 5. All test materials exhibited chemical compositions within the specifications of the appropriate material. The Phase I TC128B exhibited a sulfur composition of 0.008% (high sulfur) whereas Phase II included a medium sulfur (A-material, 0.005%) and two ultra-low sulfur heats (S-material and T-material, 0.002% and 0.0025%, respectively). Recall too that the S- and T-materials differed in thickness (thinner, 0.5-inch thick S-material as opposed to 0.73-inch T-material). The grain structures of the three Phase II TC128B materials are shown in Figure 24.

The grain structure was the typical fine grain microstructure observed in TC128B with banding and linear stringer features indicating plate rolling with consistent plate center and near edge microstructures (see Figure 24).

The materials listed in Table 5 were procured to assess the role of sulfur. Any other material differences or microstructural differences between the materials that could have had an effect on properties were not considered in this work (hence beyond the scope of this program). For instance, Table 5 indicates that the differences in the four materials are not only sulfur content but also other elemental species (as well as potentially processing variables from the different material suppliers). For example, the nickel content of the SSAB material is markedly greater than any of the other TC128B samples.

Table 4. Chemical composition of the three non-TC128B materials.

	Composition, weight percent					
	A709 Gr. HPS100W		NUCU (A710-Gr. B)		A514 Gr. B	
Element	**spec**	**measured**	**spec**	**measured**	**spec**	**measured**
Carbon	<0.08	0.06	0.03–0.40	0.07	0.12–0.21	0.19
Manganese	0.95–1.5	0.99	0.4–0.8	0.71	0.70–1.00	0.93
Phosphorus	<0.015	0.006	<0.035	0.006	<0.035	0.011
Sulfur	<0.006	<0.005	<0.04	<0.005	<0.035	<0.005
Silicon	0.15–0.35	0.26	0.4–0.6	0.42	0.20–0.35	0.24
Nickel	0.65–0.90	0.79	0.65–1.0	0.94	n/a	0.21
Chromium	0.40–0.65	0.51	n/a	0.07	0.40–0.65	0.44
Molybdenum	0.40–0.65	0.48	n/a	0.05	0.15–0.25	0.17
Copper	0.9–1.2	1.1	1.3–1.5	1.4	n/a	0.20
Aluminum	0.02–0.05	0.03	n/a	0.03	n/a	0.03
Vanadium	0.04–0.08	0.06	n/a	<0.01	0.03–0.08	0.03
Niobium	0.01–0.03	0.02	<0.006	0.004	n/a	<0.01
Titanium	n/a	<0.01	<0.03	0.03	0.01–0.03	0.02
Boron	<0.006	<0.005	n/a	0.005	<0.005	0.002

Hardness and room temperature CVN fracture toughness was also evaluated as shown in Table 6 and Table 7. The measured hardness of the materials was consistent with expectation for the expected strength levels of the materials:

- HPS100W: expected UTS 110-130 ksi, UTS inferred from hardness 129 ksi
- NUCU: expected UTS >82 ksi, UTS inferred from hardness 98 ksi
- A514B: expected UTS 110-130 ksi, UTS inferred from hardness 124 ksi

- TC128B: expected UTS 81-101 ksi, UTS inferred from hardness for the four heats 84-90 ksi

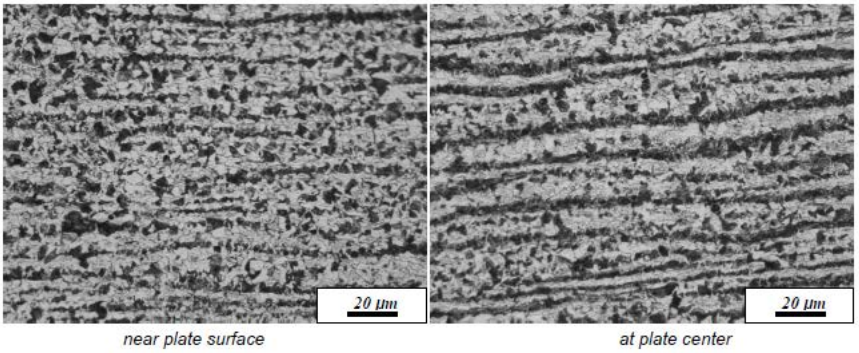

(a) A-material (medium sulfur)

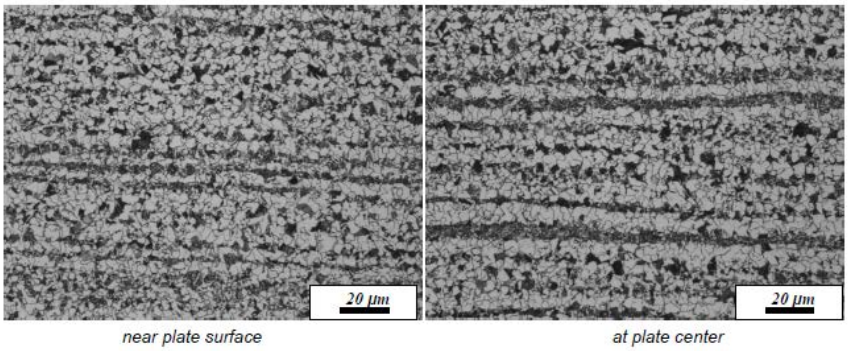

(b) S-material (low sulfur)

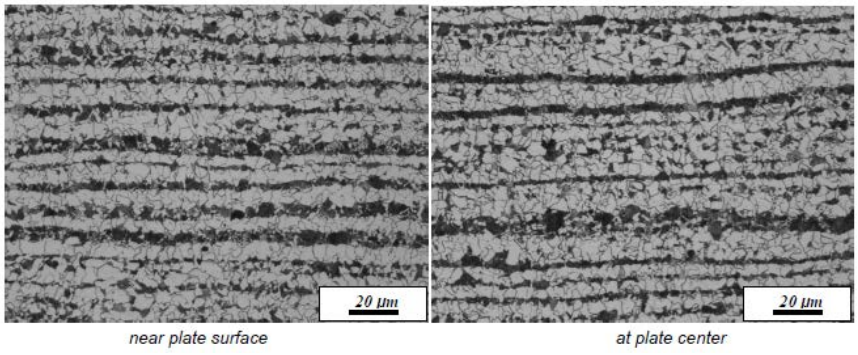

(c) T-material (low sulfur)

Figure 24. Microstructure of the three Phase II TC128B materials.

Table 5. Chemical composition of the Phase I and Phase II (A-, S- and T-) TC128B materials.

Element	Composition, weight percent						
	AAR App M spec (2012)	Ph. I matl measured	A-matl measured	S-material heat	S-material measured	T-material heat	T-material measured
Carbon	<0.26	0.23	0.21	0.20	0.19	0.22	0.21
Manganese	1.00 – 1.70	1.39	1.37	1.37	1.39	1.34	1.27
Phosphorus	<0.025	0.030	0.008	0.008	0.009	0.014	0.014
Sulfur	<0.015	0.008	0.005	0.001	0.002	0.002	0.0025
Silicon	0.15 – 0.50	0.44	0.35	0.20	0.20	0.34	0.33
Nickel	no limit	0.02	0.010	0.17	0.170	0.01	0.008
Chromium	no limit	0.21	0.16	0.12	0.13	0.16	0.16
Molybdenum	no limit	0.07	0.06	0.06	0.06	0.057	0.05
Copper	<0.35	0.03	0.020	0.25	0.241	0.016	0.013
Aluminum	0.015 – 0.060	0.03	0.035	0.023	0.022	n/a	0.027
Vanadium	<0.084	0.06	0.066	0.043	0.041	0.055	0.050
Niobium	n/a	<0.01	0.002	0.002	0.003	n/a	0.001
Titanium	<0.02	<0.01	0.001	0.001	0.002	0.002	0.003
Boron	<0.0005	<0.005	0.0002	0.0001	0.0004	0.0002	0.0001
Nitrogen	<0.012	n/a	0.0085	0.0065	0.0067	n/a	0.0070
Tin	<0.02	n/a	n/a	0.009	n/a	n/a	n/a
Carbon EQ (CE)	<0.55	0.53	0.50	0.50	0.50	0.50	0.48
Cu+Ni+Cr+Mo	<0.65	0.33	0.25	0.60	0.60	0.24	0.23
Nb+V+Ti	<0.11	0.020	0.003	0.046	n/a	n/a	0.064
Ti/N	<4.0	n/a	0.12	0.15	0.30	n/a	0.43

CE = %C + %Mn/6 + (%Cr + %Mo + %V)/5 + (%Cu + %Ni)/15

Table 6. Hardness and room temperature CVN tests for the three non-TC128B materials.

Material	Hardness			Room Temperature (73°F) CVN energy, ft-lbs					
	Rockwell B- or C-			Longitudinal			Transverse		
	A	B	C	A	B	C	A	B	C
HPS100W	27	27	26	180	181	191	205	213	201
	Rc =27 ~ 129 ksi UTS			TYP ~ 180 ft-lbs			TYP ~ 205 ft-lbs		
NUCU	93	93	94	143	135	139	175	187	175
	Rb =93 ~ 98 ksi UTS			TYP ~ 139 ft-lbs			TYP ~ 175 ft-lbs		
A514B	25	25	25	94	96	96	139	143	132
	Rc =25 ~ 124 ksi UTS			TYP ~ 96 ft-lbs			TYP ~ 139 ft-lbs		

Table 7. Hardness and room temperature CVN tests for the four different TC128B materials.

TC128B Material Pedigree	Hardness			Room Temperature (73°F) CVN energy, ft-lbs					
	Rockwell B or Brinell (HB)			Longitudinal			Transverse		
	A	B	C	A	B	C	A	B	C
Phase I	87	88	87	70	70	46	53	65	64
	Rb =87 equiv to HB 170 (~84 ksi UTS)			TYP ~ 70 ft-lbs			TYP ~ 65 ft-lbs		
A-material	185	185	186	134	124	102	99	107	108
	HB = 185 (~90 ksi UTS)			TYP ~ 120 ft-lbs			TYP ~ 105 ft-lbs		
S-material	188	187	180	118	115	119	105	117	133
	HB = 185 (~90 ksi UTS)			TYP ~ 117 ft-lbs			TYP ~ 119 ft-lbs		
T-material	175	174	169	132	121	136	148	143	150
	HB = 173 (~86 ksi UTS)			TYP ~ 130 ft-lbs			TYP ~ 147 ft-lbs		

As an indication of upper shelf hardness, CVN toughness was evaluated at room temperature conditions (even though most materials have specifications for low temperature toughness, this particular aspect of the materials was not evaluated during this program). Transverse room temperature toughnesses for the non-TC128B materials were in the range of 140-200 ft-lbs whereas for TC128B values of 70-150 were evaluated.

Toughness is expected to increase with decreasing sulfur content for TC128B (see, for instance, earlier referenced Heitmann paper). An examination of the upper shelf toughness values in Table 7 clearly indicates this with the high sulfur Phase I material exhibiting 65 ft-lbs (room temperature), the medium sulfur (A-material) at 105 ft-lbs and the two low sulfur materials in the range of 120-150 ft-lbs. For the Phase II TC128B's evaluated in Phase II, additional CVN tests were performed as a function of temperature as shown in Figure 25. Although the data is scattered, the most pronounced influence of temperature was apparent for the longitudinal specimens (bottom plot, Figure 25) with the lowest temperature CVN toughness approximately 2 times greater for the low sulfur conditions.

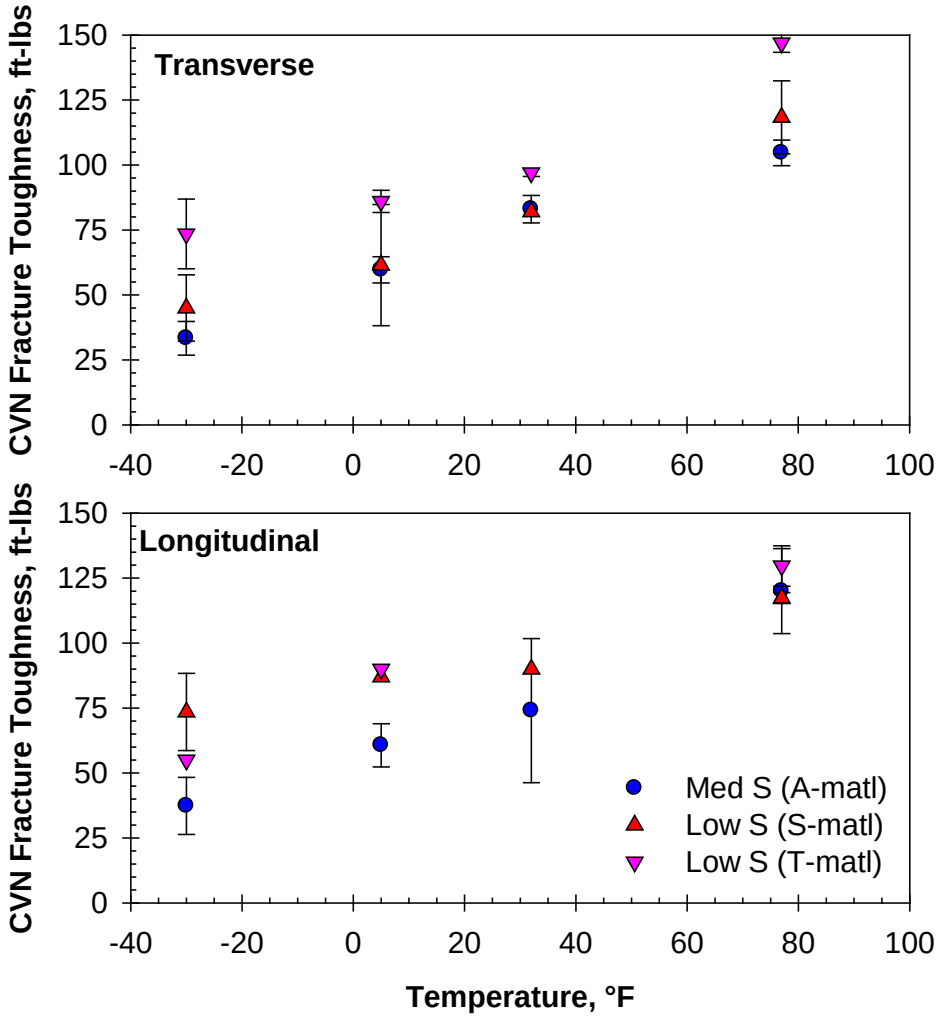

Figure 25. CVN fracture toughness as a function of temperature for Phase II TC128B materials.

3.1.3 Test Matrices and Experimental Methods

The testing performed during Phase I and Phase II are described in detail in Table 8-Table 11. All tests were performed under room temperature conditions. All seven materials were subjected to the following tests:

- Tensile stress-strain tests on smooth specimens in both the longitudinal and transverse orientation
- Tensile stress-strain tests on notched specimens (three notch radii: 0.05, 0.10 and 0.25-inch) in the longitudinal orientation

- Phase I testing only – tensile stress-strain tests on smooth specimens (reduced gage length) in the longitudinal orientation at three different rates: quasistatic, intermediate and high loading rate.
- Phase II testing only – shear tests on a 0.5-inch thick specimen with a notch radius of 0.05-inch.

Table 8. Test matrix for each material involved in the material property testing (Phase I).

Specimen Geometry	Gage Length	Notch Radius	Test Rate	Specimen Orientation	No. of Replicates
smooth	2-inch	none	quasistatic	L	2
			quasistatic	T	2
smooth	0.75-inch	none	quasistatic	L	2
			intermediate	L	2
			highest possible	L	2
notched	2-inch	0.25-inch	quasistatic	L	2
		0.10-inch	quasistatic	L	2
		0.05-inch	quasistatic	L	2

Table 9. Test parameters for the smooth and notched tensile tests at quasistatic rate (Phase I).

Quantity	Smooth	Notched
Gage dimensions (inch):	0.25D x 2.0	0.25D net, various notches
Test specification:	ASTM E8-11	none (spirit of E8)
Extensometer gage length (inch):	1.0	0.5
Head rate <5% ε (inch/minute):	0.005	0.030
Head rate >5% ε (inch/minute):	0.050	0.030
Test temperature:	RT	RT

Table 10. Test parameters for the variable rate tensile tests (Phase I).

Quantity	Smooth
Gage dimensions (inch):	0.25D x 0.75
Test specification:	ASTM E8-11
Extensometer gage length (inch):	0.5
Open Loop Head Rate (inch/second): *Intermediate Head Rate (inch/minute):*	1.4 – 1.6 0.02
Open Loop Strain Rate (inch/inch/second) *Intermediate Strain Rate (inch/inch/minute):*	0.50 – 0.55 0.01
Test temperature:	RT

Table 11. Test matrix for each material involved in the material property testing (Phase II).

Specimen Geometry	Overall Dimensions	Notch Radius	Test Rate	Specimen Orientation	No. of Replicates
smooth	2-inch GL	none	quasistatic	L	2 – 4
			quasistatic	T	2 – 4
notched	2-inch GL	0.25-inch	quasistatic	L	2 – 3
		0.10-inch	quasistatic	L	2
		0.05-inch	quasistatic	L	2
shear	0.5” thick	0.05-inch	quasistatic	L	2 – 3

The change in testing between Phase I and Phase II was due to ongoing modification of program goals and objectives based upon results from analyses performed during the program.

Tensile and notch testing was performed in accordance with the ASTM E8 metallic material tensile test standard. For the smooth tensile testing, ASTM standard 2-inch and 0.75-inch gage length specimens were utilized. The notched specimen design shown in Figure 26, with different sized notches and a fixed net section diameter, is based upon testing performed during the previous NGRTC program. The shear test specimen utilized during testing, Figure 27, was also adopted from the previous NGRTC testing program. Note that this shear test evaluates the worst case 90° shear condition (previous testing evaluated different angular offsets but this particular condition is the worst-case and most critical for modeling).

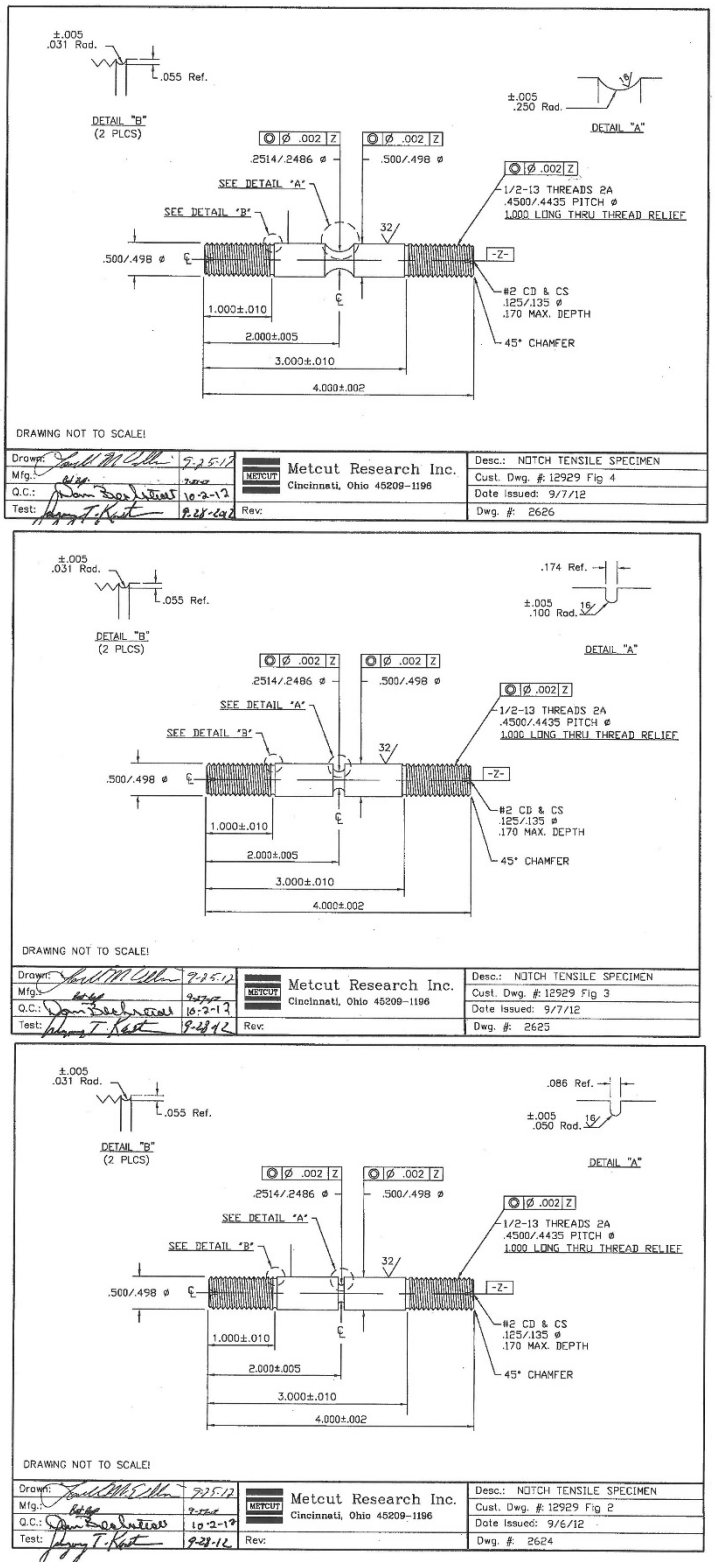

Figure 26. Three different notched tensile specimen geometries with a 2-inch gage length.

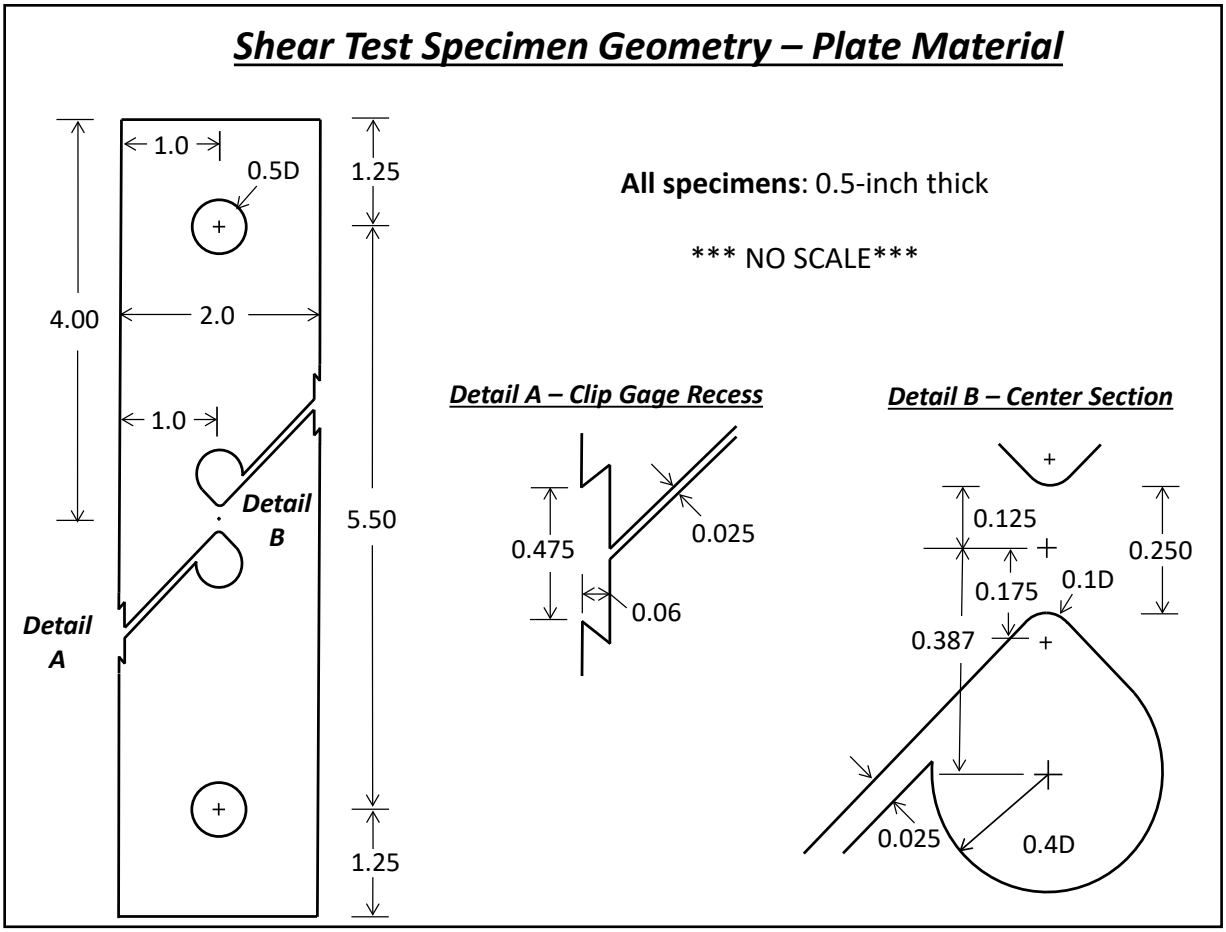

Figure 27. Shear test specimen utilized for testing.

For reference, photographs of typical test setups are provided in Figure 28, highlighting the instrumentation utilized during testing. The instrumentation attached to the specimens in Figure 28 are transducers designed to measure displacement on the specimen. Each test result was essentially a discrete listing of load and displacement that was subsequently analyzed to provide insight and results for the test.

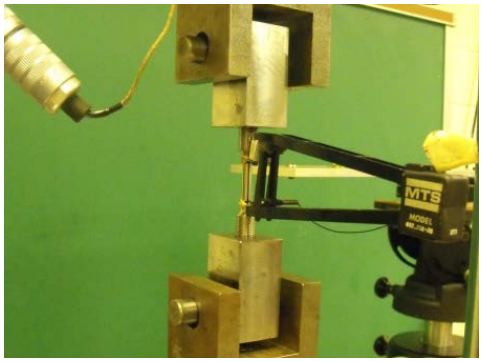

(a)

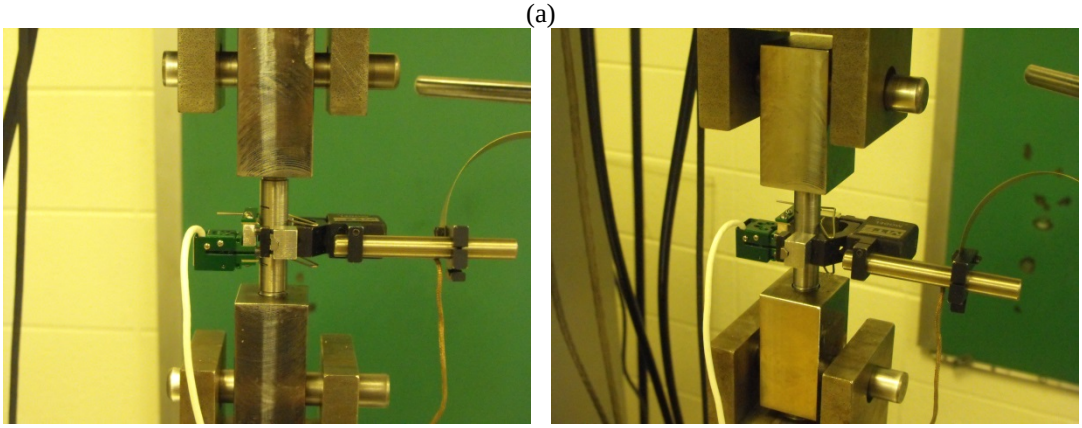

(b)

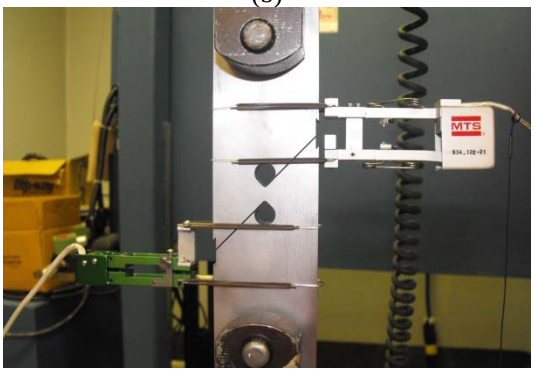

(c)

Figure 28. Different test setups for (a) smooth, (b) notched, and (c) shear tests.

3.2 Overview of Results

The key data from this program for the modeling was the continuous load-displacement data recorded during the tests. Examples of the measured data for the smooth and notched round bar tensile tests are shown in Figure 29, Figure 30, and Figure 31 for the NUCU, HPS100W and A514B steels respectively. In these figures the load and displacement data have been converted to engineering stress-strain data for the tests.

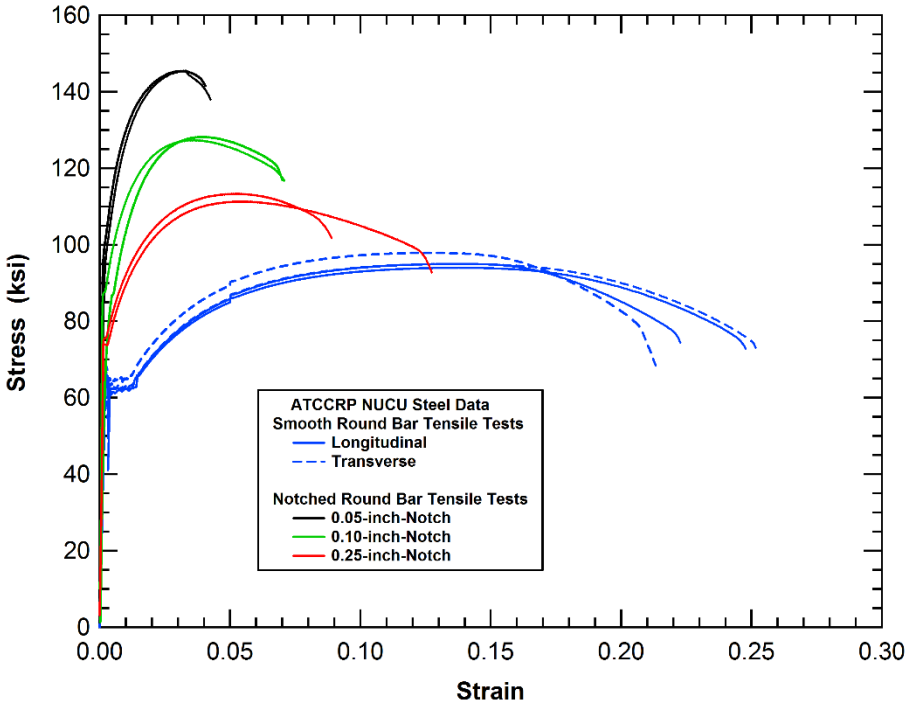

Figure 29. Characterization test data for the ATCCRP NUCU Steel.

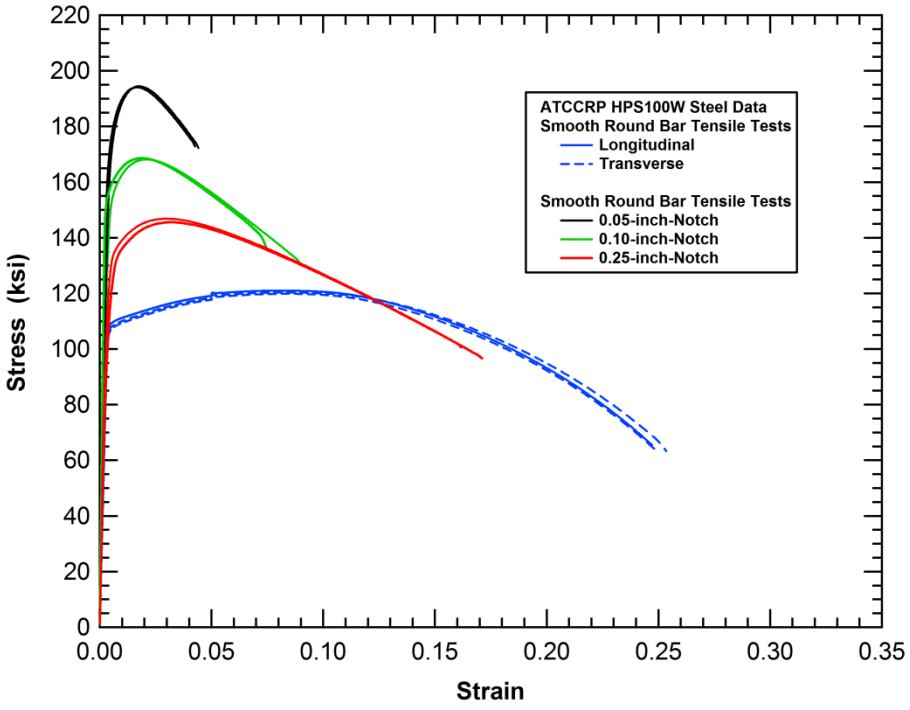

Figure 30. Characterization test data for the ATCCRP HPS100W Steel.

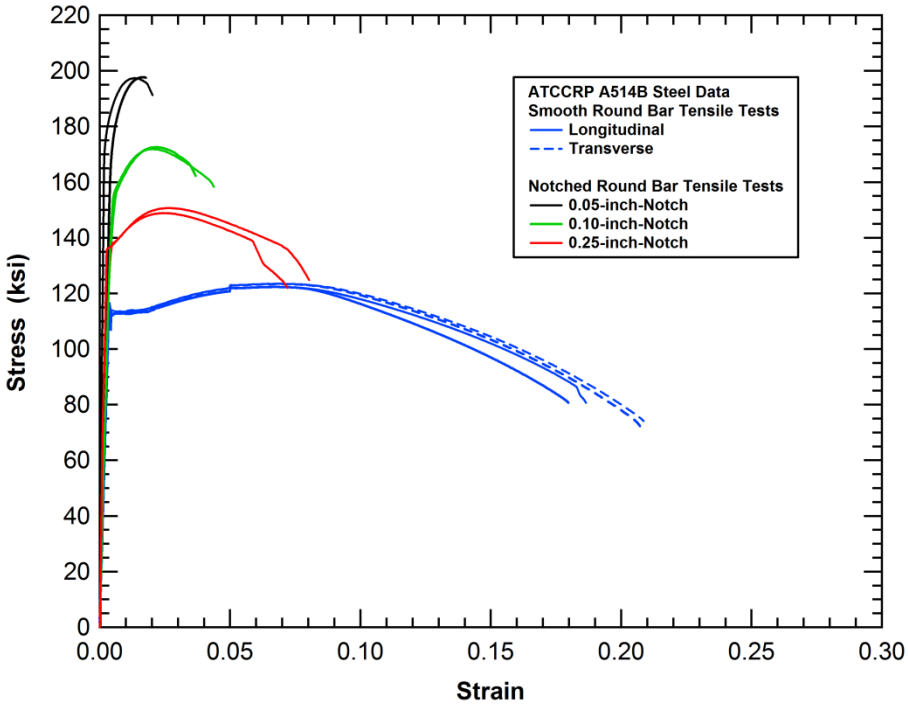

Figure 31. Characterization test data for the ATCCRP A514B Steel.

In this section of the report, we provide primarily a tabular summary of the tests and the key data resulting from each test. Tabulated results for the Phase I testing are included in Table 12-Table 14 and for Phase II in Table 15-Table 17. These critical continuous test data results will be provided in a subsequent section of this report when the data fits used in the analysis are presented.

3.2.1 Smooth Specimen Tensile Properties

A comparison of the average tensile properties measured for the non-TC128B material tested during Phase I is summarized in Figure 32 based upon the average data in Table 12. Several observations are apparent. First, the degree of observed anisotropy (difference between the two orientations) is very low. The materials are homogeneous, likely based on the fine grain microstructure apparent in these materials. The two highest strength steels, namely the A514B and A709 Gr HPS100W, exhibit very similar properties with slightly higher strength and lower ductility observed in the A514B steel. Conversely the NUCU material (A710 Gr B) tensile properties in Figure 32 exhibit lower strength and higher ductility than the other two steels.

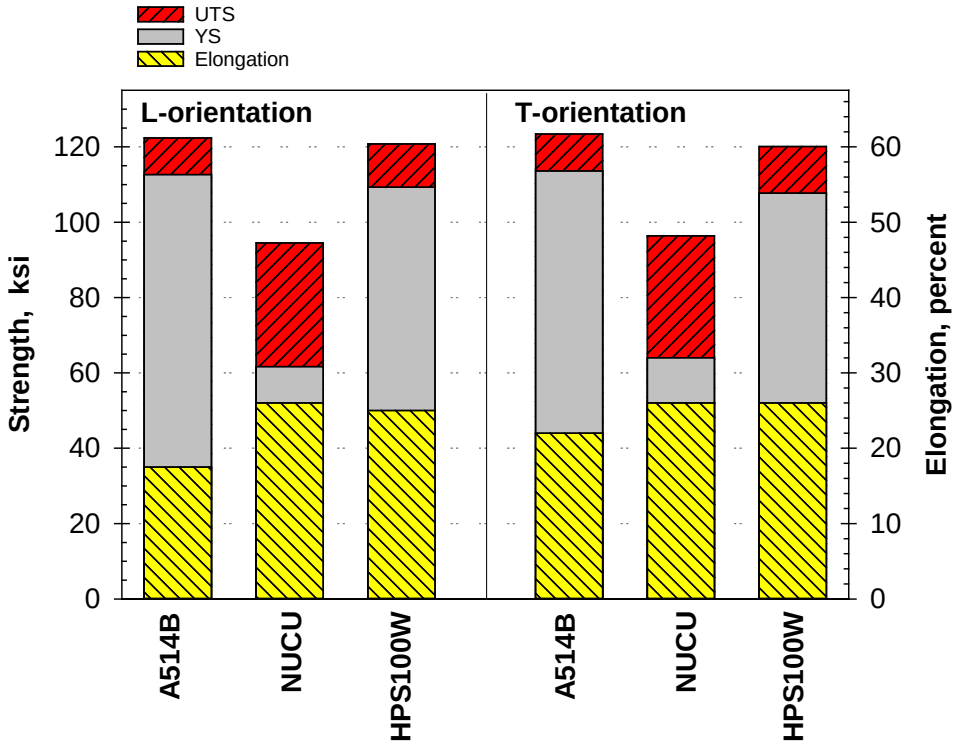

Figure 32. Tensile property comparison of Phase I non-TC128B materials.

Tensile strain rate effects can be determined for the Phase I materials by comparing data in Table 14. Strain rate makes no statistical impact on ductility; this is true if either the percent elongation or reduction of area data are compared in Table 14. The rate effects manifested by strength are fairly weak. For the non-TC128B materials in Table 14, the result of a higher rate is only 4-7 ksi in tensile strength (slightly higher impact on yield strength). Virtually no statistical increase in properties is noted for the Phase I TC128B tested at high rate.

The average tensile properties for the four different TC128B heats is shown in Figure 33 based on the data in Table 15. Note that the average values are for both orientations combined; the extent of anisotropy noted was negligible between the two orientations. On balance, little strength or ductility variation is apparent for any of these different TC128B heats. This suggests that sulfur content has a minimal impact on tensile properties. The lowest strength and highest ductility observed was for the Phase II T-material (low sulfur content and extracted from a tank car being built). Recall this material was subjected to a PWHT treatment since it had been curved into one of the tank car segments. It is unknown whether the slight difference in tensile properties for this material when compared to the other materials is a consequence of the PWHT or simply lot-to-lot variability.

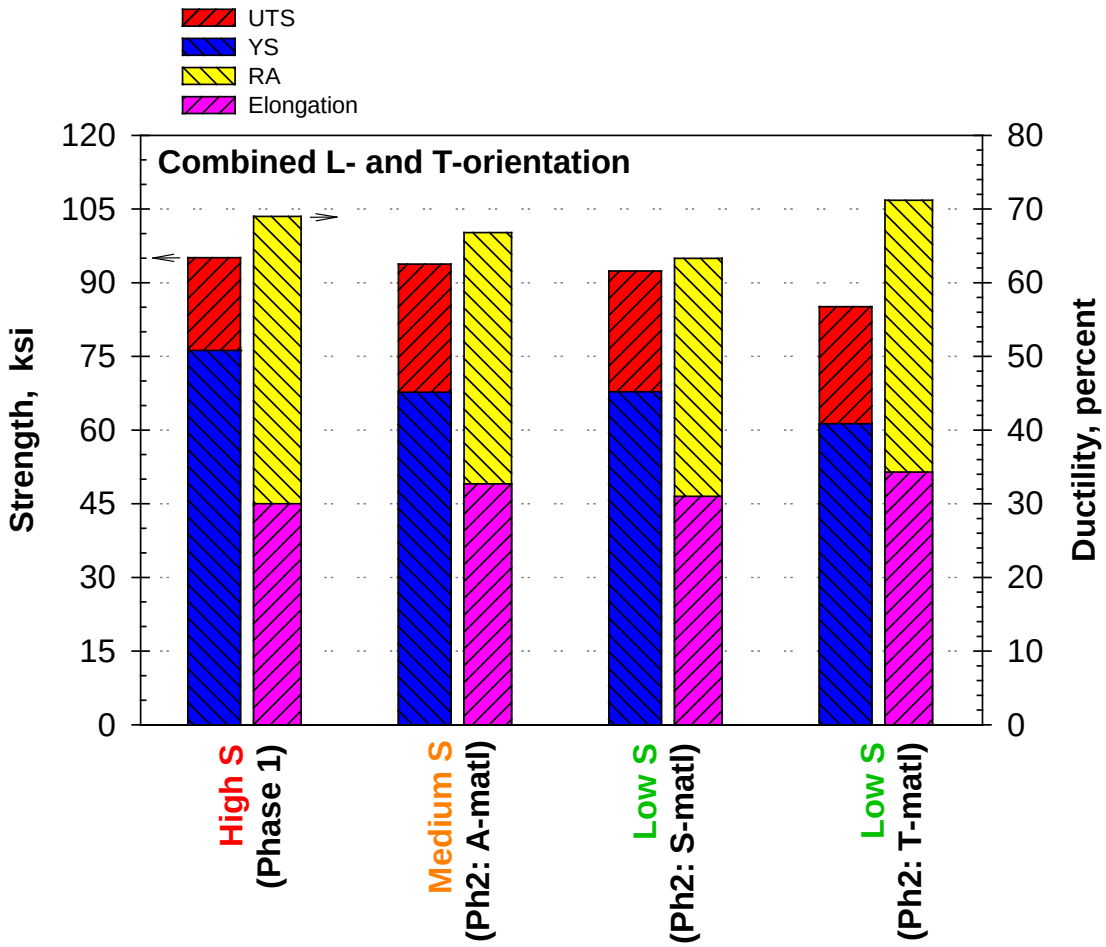

Figure 33. Tensile property comparison of Phase I and II TC128B materials.

Table 12. Measured tensile properties for both orientations (Phase I).

Material	Orientation	Specimen ID No.	UTS, ksi	YS, ksi	Elong (2"GL),%	RA, %
TC128B	L	T-L-S-1	96	77	28	67
		T-L-S-2	96	76	31	68
	T	T-T-S-1	95	76	31	70
		T-T-S-2	95	76	30	71
	Average:		**95.1**	**76.2**	**30.0**	**69.0**
A514B	L	N-L-S-1	122	113	20	61
		N-L-S-2	122	113	15	62
	T	N-L-T-1	124	114	22	68
		N-L-T-2	123	114	22	67
	Average:		**122.9**	**113.1**	**19.8**	**64.5**
NUCU	L	A-L-S-1	94	62	26	57
		A-L-S-2	95	62	26	57
	T	A-T-S-1	98	65	25	50
		A-T-S-2	95	64	27	55
	Average:		**95.5**	**62.9**	**26.0**	**54.8**
HPS100W	L	H-L-S-1	121	109	>15[3]	74
		H-L-S-2	121	109	25	75
	T	H-T-S-1	120	107	26	76
		H-T-S-2	120	108	26	75
	Average:		120.5	108.5	25.7	75.0

[3] Specimen failed outside gage length marks; value based on total length measurement

Table 13. Notched tensile test results (L-orientation, Phase I).

Material	Specimen ID No.	Notch D, inch	Notch R, inch	Max Net Stress, ksi	Max Bridging Strain (0.5" GL), in/in
TC128B	T-05-S-1	0.2508	0.0518	151.1	5.0
	T-05-S-2	0.2502	0.0508	151.5	5.6
	T-10-S-1	0.2506	0.1013	132.4	9.1
	T-10-S-2	0.2498	0.1013	132.0	9.4
	T-25-S-1	0.2512	0.2474	113.2	16.7
	T-25-S-2	0.2507	0.2474	114.3	16.7
A514B	N-05-S-1	0.2510	0.0510	197.4	2.0
	N-05-S-2	0.2506	0.0518	197.7	1.8
	N-10-S-1	0.2510	0.1014	172.5	3.7
	N-10-S-2	0.2507	0.1009	171.9	4.4
	N-25-S-1	0.2507	0.2474	150.7	8.0
	N-25-S-2	0.2511	0.2474	148.9	7.2
NUCU	A-05-S-1	0.2508	0.0507	145.5	4.3
	A-05-S-2	0.2513	0.0508	145.4	3.6
	A-10-S-1	0.2514	0.1011	128.2	7.0
	A-10-S-2	0.2508	0.1010	127.3	7.1
	A-25-S-1	0.2512	0.2476	111.3	12.7
	A-25-S-2	0.2506	0.2472	113.3	8.9
HPS100W	H-05-S-1	0.2513	0.0510	194.1	4.3
	H-05-S-2	0.2508	0.0512	194.5	4.4
	H-10-S-1	0.2507	0.1012	168.2	8.9
	H-10-S-2	0.2512	0.1010	168.6	7.5
	H-25-S-1	0.2510	0.2472	145.6	17.1
	H-25-S-2	0.2506	0.2474	146.9	16.2

Table 14. Quasistatic and high rate tensile test results (L-orientation, Phase I).

Material	Test Rate	Specimen ID No.	UTS, ksi	YS, ksi	Elong (0.5"GL),%	RA, %
TC128B	quasistatic	T-Q-1	96.7	76.3	28	67
		T-Q-2	95.5	75.4	26	65
	intermediate	T-M-1	96.5	76.1	29	66
		T-M-2	96.1	76.0	28	70
	high-rate	T-O-1	96.9	79.8	26	66
		T-O-2	101.6	84.0	27	66
A514B	quasistatic	N-Q-1	119.6	109.9	21	66
		N-Q-2	120.0	110.4	21	64
	intermediate	N-M-1	120.5	110.5	21	63
		N-M-2	120.4	110.1	20	64
	high-rate	N-O-1	126.9	118.3	21	63
		N-O-2	126.7	118.5	20	60
NUCU	quasistatic	A-Q-1	94.8	60.2	22	53
		A-Q-2	96.3	62.6	22	44
	intermediate	A-M-1	95.0	61.3	26	47
		A-M-2	95.6	61.8	28	56
	high-rate	A-O-1	102.1	72.0	25	53
		A-O-2	103.1	73.5	24	51
HPS100W	quasistatic	H-Q-1	119.3	106.5	24	74
		H-Q-2	120.0	107.0	24	75
	intermediate	H-M-1	120.0	107.3	25	74
		H-M-2	119.3	106.2	25	75
	high-rate	H-O-1	124.0	112.5	23	71
		H-O-2	123.7	112.7	24	72

Table 15. Measured tensile properties for the three TC128B variants in Phase II.

Material	Orientation	Specimen ID No.	UTS, ksi	YS, ksi	Elong (1"GL),%	RA, %
A-material	L	A-289-L1	93	67	33	68
		A-289-L2	94	69	32	70
	T	A-289-T1	94	67	34	66
		A-289-T2	94	67	31	64
	average:		**93.8**	**67.7**	**32.7**	**66.8**
S-material	L	S-288-L1	93	67	34	64
		S-288-L2	92	68	31	63
	T	S-288-T1	92	68	30	64
		S-288-T2	92	68	29	63
	average:		**92.4**	**67.8**	**31.0**	**63.3**
T-material	L	T-290-L1	86	62	31	70
		T-290-L2	85	63	36	71
	T	T-290-T1	85	61	35	71
		T-290-T2	85	60	35	73
	average:		**85.1**	**61.3**	**34.3**	**71.2**

Table 16. Notched tensile results (L orientation) for the three TC128B variants in Phase II.

Material	Notch Radius, inch	Specimen ID No.	Max Net Stress, ksi	Axial Displ at Failure, inch	Net Failure Stress, ksi	RA, %
A-material	0.05	A-289-N05-L1	144	0.031	131	36
		A-289-N05-L2	143	0.033	125	37
		A-289-N05-L3	145	0.038	125	43
	0.10	A-289-N10-L1	127	0.045	111	44
		A-289-N10-L2	127	0.052	104	50
		A-289-N10-L3	126	0052	104	49
	0.25	A-289-N25-L1	111	0.080	86	56
		A-289-N25-L2	111	0.095	82	63
		A-289-N25-L3	109	0.087	84	57
S-material	0.05	S-288-N05-L1	143	0.037	122	48
		S-288-N05-L2	141	0.036	122	49
	0.10	S-288-N10-L1	125	0.052	102	47
		S-288-N10-L2	123	0.047	100	48
	0.25	S-288-N25-L1	109	0.083	86	53
		S-288-N25-L2	108	0.090	81	57
T-material	0.05	T-290-N05-L1	131	0.047	106	52
		T-290-N05-L2	130	0.045	107	53
	0.10	T-290-N10-L1	117	0.059	90	54
		T-290-N10-L2	115	0.064	88	54
	0.25	T-290-N25-L1	102	0.103	71	76
		T-290-N25-L2	101	0.103	71	70

Table 17. Shear test results for the three TC128B variants in Phase II.

Material	Specimen ID No.	Max Shear Stress, ksi	Axial Displ at Failure, inch	Failure Shear Stress, ksi
A-material	A-289-S1	76	0.209	72
	A-289-S2	77	0.190	75
S-material	S-288-S1	74	0.195	67
	S-288-S2	74	0.200	68
T-material	T-290-S1	71	0.231	65
	T-290-S2	71	0.229	63

3.2.2 Notched Specimen Tensile Properties

One way to examine notched strength test results is to quantify the notch strength ratio, defined as the ratio of the notch strength (maximum net stress incurred in the specimen) normalized by the ultimate strength of the material. These notch strength ratios are shown in Figure 34 (non-TC128B materials, based on the data in Table 13) and Figure 35 (TC128B materials, based on the data in Table 13 and Table 16).

The notched strength ratio in Figure 34 and Figure 35 indicates the conventional expected trend for all materials and heats. As notch acuity increases (the notch gets tighter and the stress concentration increases), the achieved notch strength also increases. For the tightest notches, the net stress is over 150% of the ultimate strength of the material. For the bluntest notches, the level falls to 120% of the ultimate strength of the material.

All seven test materials exhibited very similar trends and magnitudes of notch strength ratio as seen in Figures Figure 34 and Figure 35. In fact, the similarity in notched strength for the TC128B material (Figure 35) is remarkable, especially considering the medium and low sulfur heats. However, this similarity does not necessarily mean the load-strain response is similar, and this is something that will be addressed when the data are shown in the modeling section of this report.

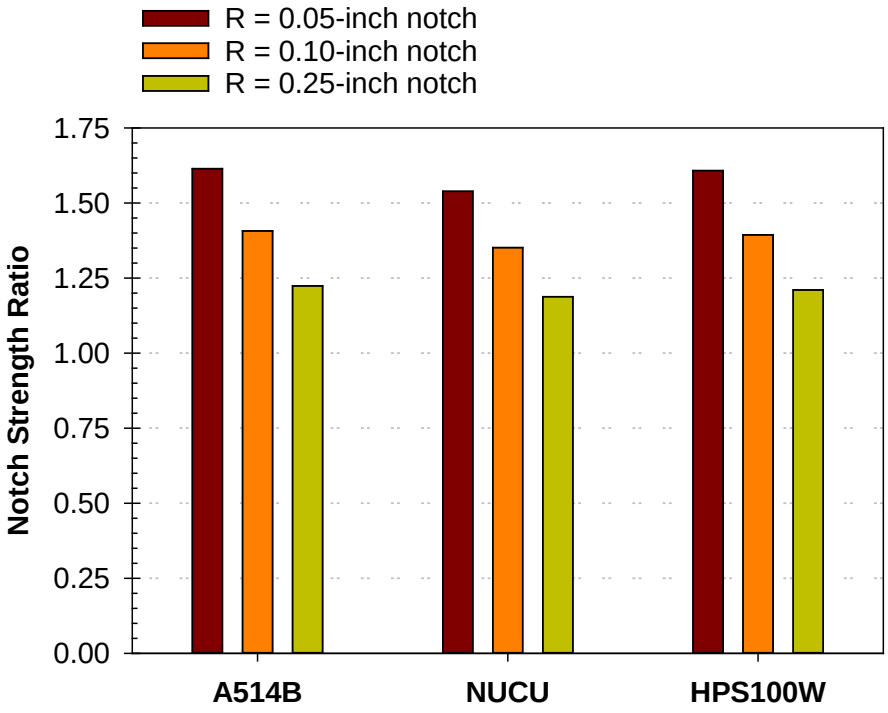

Figure 34. Notch strength comparison of Phase I non-TC128B materials.

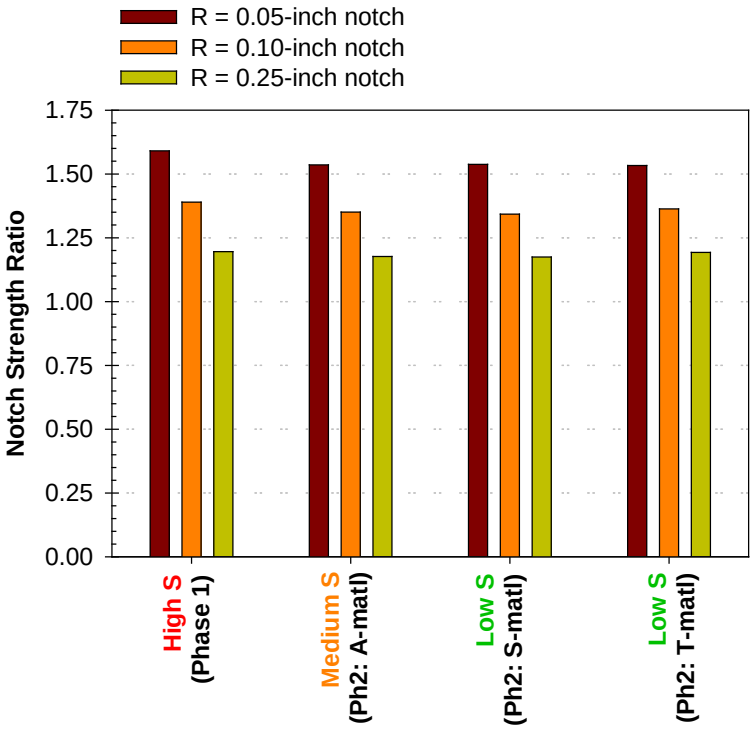

Figure 35. Notch strength comparison of Phase I and II TC1288B materials.

Another way of examining notch data is shown in Figure 36 the notch ductility ratio, essentially the measured reduction of area in the notched specimen (see Table 16) divided by the reduction of area observed in the smooth specimen test. A close examination of the reduction of area data in Table 16 indicates that in the presence of the notch, the ductility typically stays the same or decreases; in the smooth tests, RA for TC128B varies between 65-75% whereas in the notched test it ranges from 35-70%. When the notch data is considered in this fashion, there are some differences observed in Figure 36. The most acute notch has the lowest ductility ratio value (essentially the acute notch is more severe and in the failure process consumes ductility) whereas in the case of the bluntest notch this ratio indicates a loss of 20% or less of the ductility. The most curious trend in Figure 36 is the markedly lower ductility ratio for the medium sulfur case when compared to the two low sulfur conditions.

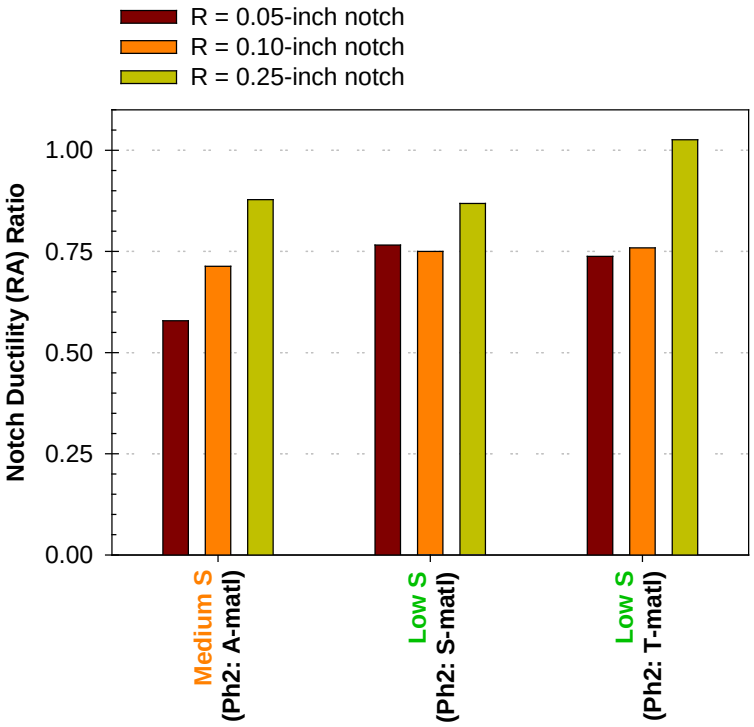

Figure 36. Notch ductility ratio comparison of Phase II TC128B materials.

3.2.3 Shear Properties

Shear tests, performed only during the Phase II testing, were performed on three heats of TC128B as shown in Table 17 and Figure 37. The results are plotted in terms of shear-stress-to-ultimate-strength ratio in Figure 37. The shear ratio results fall into a relatively tight range of 0.80-0.83 and do not appear to vary in any significant manner for the medium and low sulfur cases examined.

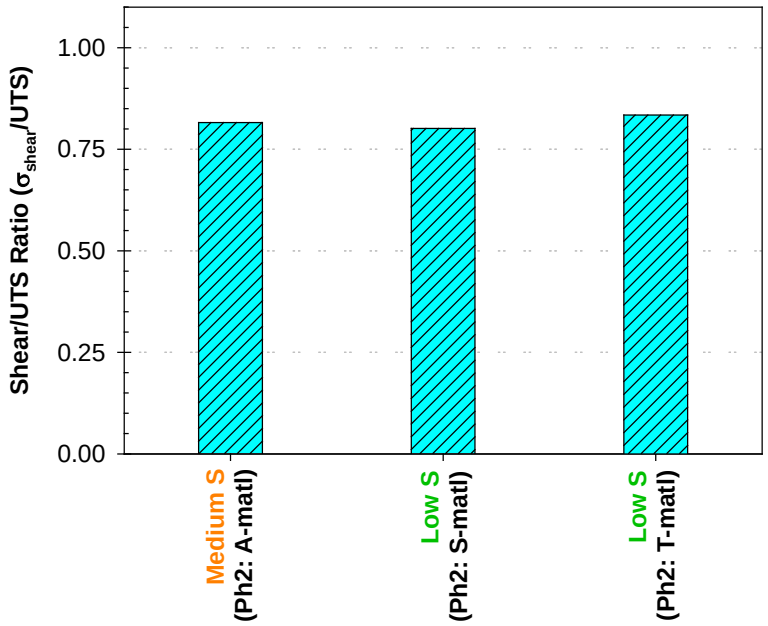

Figure 37. Shear strength comparison of Phase II TC128B materials.

3.3 Model Calibration for the Alternative Materials Characterized

A set of constitutive parameters were developed for each of the materials characterized in this program, as well as some TC128B materials characterized in previous tank car research programs. In this section, we present the material parameters and correlation of the model with test data for the non-TC128B materials tested in Phase I. The specific alloys and materials included in this study include the following:

- A709-Gr. HPS100W: moderate strength bridge steel (1-inch thick),
- NUCU: a higher strength bridge steel, nominally ASTM A710-GrB (0.5-inch thick), and,
- A514-GrB: current higher strength bridge steel (0.75-inch thick).

The baseline tensile test stress-strain behaviors for these materials are compared to each other and the Phase I TC128B in Figure 38. The plot shows that the NUCU material is similar in character to a TC128B material. Note that the Phase I TC128B Material has a significantly higher yield stress and a higher ultimate stress than any other TC128B material characterized to date in the NGRTC or ATCCRP Programs. The other two materials are higher in strength and very similar to each other with yield stresses of approximately 110 ksi and ultimate stresses of approximately 120 ksi. The comparison of the measured and calculated material behaviors are presented in the following subsections.

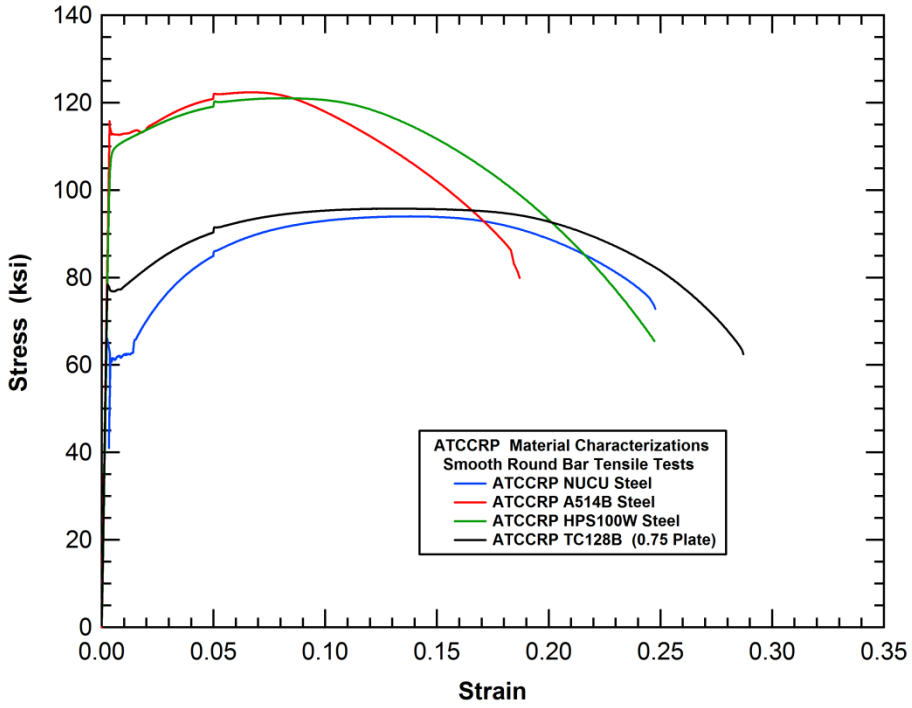

Figure 38. Comparison of tensile test stress-strain behaviors for the Phase I materials.

3.3.1 NUCU Material Properties

The material constitutive and damage model parameters can be developed primarily from the series of smooth and notched round bar tensile tests. The initial true stress versus true strain curve is developed from the smoothed round bar tensile test. Subsequent analyses of the notched tensile test allow for the determination of the Drucker Prager pressure effects coefficient and the corresponding Bao-Wierzbicki damage parameters. The final set of constitutive parameters are then used to simulate the set of smooth and notched tensile tests to validate that the constitutive model parameters have been properly determined and to show the quality of the correlation between the model and test data.

The constitutive parameters for NUCU are summarized in Table 18 and the correlation of the material constitutive model and material calibration tensile test data is shown in Figure 39. For this material, the traditional Bao-Wierzbicki Model (n=1.00) provided a good fit to the measured ductility over the range of stress triaxialities in the tests. The effect of mean stress on the yield behavior is also relatively low for this material (compared to the other materials in this study) with a Drucker-Prager yield criterion coefficient (α) equal to 0.015.

Table 18. Material constitutive parameters and tabular NUCU stress-strain values

Material Constitutive Parameters		
Bao Wierzbicki Coefficient - A		0.75
Bao Wierzbicki Coefficient - B		1.10
Modified Bao Wierzbicki Coefficient - n		1.00
Drucker Prager Coefficient - α		0.015
Point No.	**Plastic Strain (in/in)**	**True Stress (ksi)**
1	0.000e+00	66.5
2	1.810e-03	61.7
3	1.010e-02	63.5
4	1.980e-02	74.6
5	3.740e-02	86.0
6	6.060e-02	96.0
7	9.900e-02	104.2
8	1.438e-01	109.3
9	2.457e-01	116.6
10	3.950e-01	123.6
11	1.390e-00	155.8

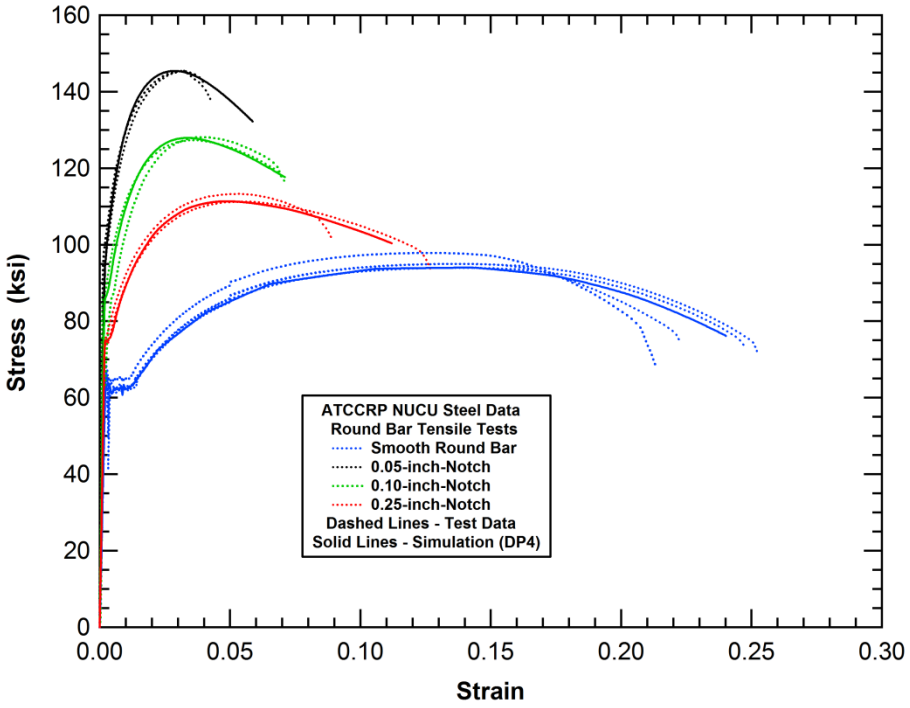

Figure 39. Model calibration for the ATCCRP NUCU Steel.

3.3.2 HPS100W Material Properties

The constitutive parameters for HPS100W are summarized in Table 19 and the correlation of the material constitutive model and material calibration tensile test data is shown in Figure 40. For this material, the Modified Bao-Wierzbicki Model was required to predict the ductility for the higher triaxiality levels (n=1.60). The effect of mean stress on the yield behavior is moderate for this material (compared to the other materials in this study) with a Drucker-Prager yield criterion coefficient (α) equal to 0.045.

Table 19. Material constitutive parameters and tabular HPS100W stress-strain values

Material Constitutive Parameters		
Bao Wierzbicki Coefficient - A		1.40
Bao Wierzbicki Coefficient - B		3.60
Modified Bao Wierzbicki Coefficient - n		1.60
Drucker Prager Coefficient - α		0.045
Point No.	**Plastic Strain (in/in)**	**True Stress (ksi)**
1	0.00E+00	109.6
2	6.50E-04	111.1
3	2.48E-03	112.2
4	6.06E-03	114.1
5	1.95E-02	119.2
6	3.55E-02	124.8
7	5.83E-02	130.6
8	8.52E-02	135.0
9	1.45E-01	140.0
10	2.94E-01	151.2
11	1.29E+00	203.0

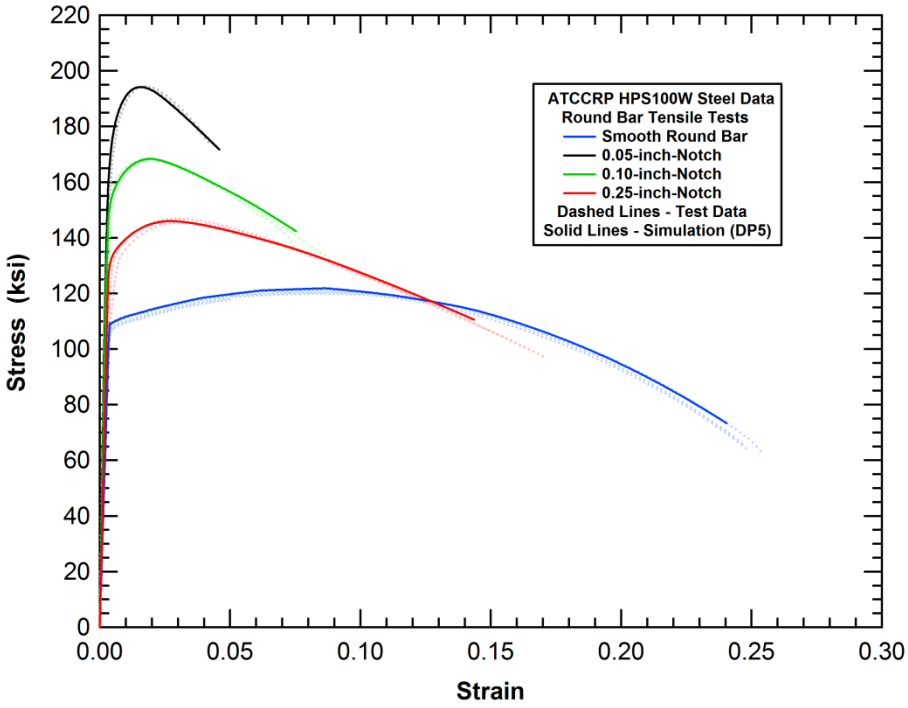

Figure 40. Model calibration for the ATCCRP HPS100W Steel.

3.3.3 A514B Material Properties

The constitutive parameters for A514B are summarized in Table 20 and the correlation of the material constitutive model and material calibration tensile test data is shown in Figure 41. For this material, the Modified Bao-Wierzbicki Model was required to predict the ductility for the higher triaxiality levels (n=2.20). The effect of mean stress on the yield behavior is moderate for this material (compared to the other materials in this study) with a Drucker-Prager yield criterion coefficient (α) equal to 0.035.

Table 20. Material constitutive parameters and tabular A514B stress-strain values

Material Constitutive Parameters		
Bao Wierzbicki Coefficient - A		1.20
Bao Wierzbicki Coefficient - B		3.00
Modified Bao Wierzbicki Coefficient - n		2.20
Drucker Prager Coefficient - α		0.035
Point No.	**Plastic Strain (in/in)**	**True Stress (ksi)**
1	0.00E+00	117.5
2	4.20E-04	114.5
3	1.29E-02	116.6
4	2.31E-02	121.2
5	3.71E-02	126.5
6	5.57E-02	131.4
7	8.51E-02	135.0
8	1.25E-01	137.6
9	1.95E-01	141.1
10	2.94E-01	145.2
11	1.29E+00	182.1

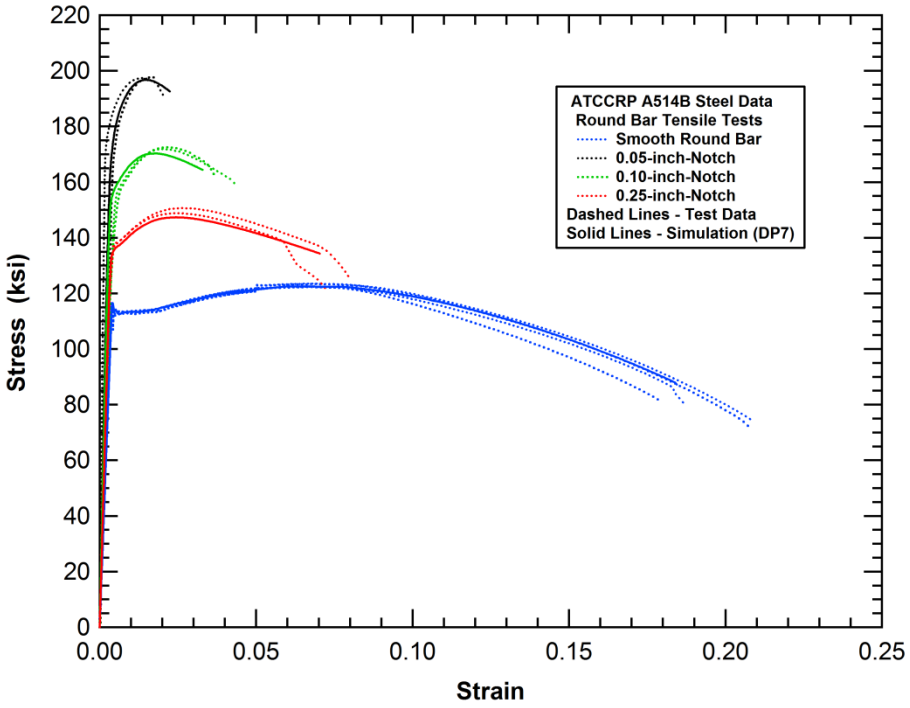

Figure 41. Model Calibration for the ATCCRP A514B Steel.

3.4 Evaluation of TC128B Steel samples

In addition to characterizing alternative steels, tests and analyses were performed on various samples of TC128B to investigate variability and where possible correlations to composition. It has been previously observed that there can be significant variations in the mechanical properties of TC128B. For example, the tensile stress-strain properties of the TC128B Samples tested in this program are compared to several other samples from previous research programs in Figure 42. These various samples have yield strengths ranging from approximately 55 ksi to over 75 ksi and ultimate strengths of 83 to 95 ksi.

In addition to the TC128B samples characterized in this research program, previous sets of TC128B characterization test data were available from the NGRTC research program [1-8]. These material data sets were reexamined and updated constitutive parameters were developed that include the Drucker Prager yield effects and modified Bao Wierzbicki damage model. The re-characterization and model comparisons for these materials are included in the following section of the report.

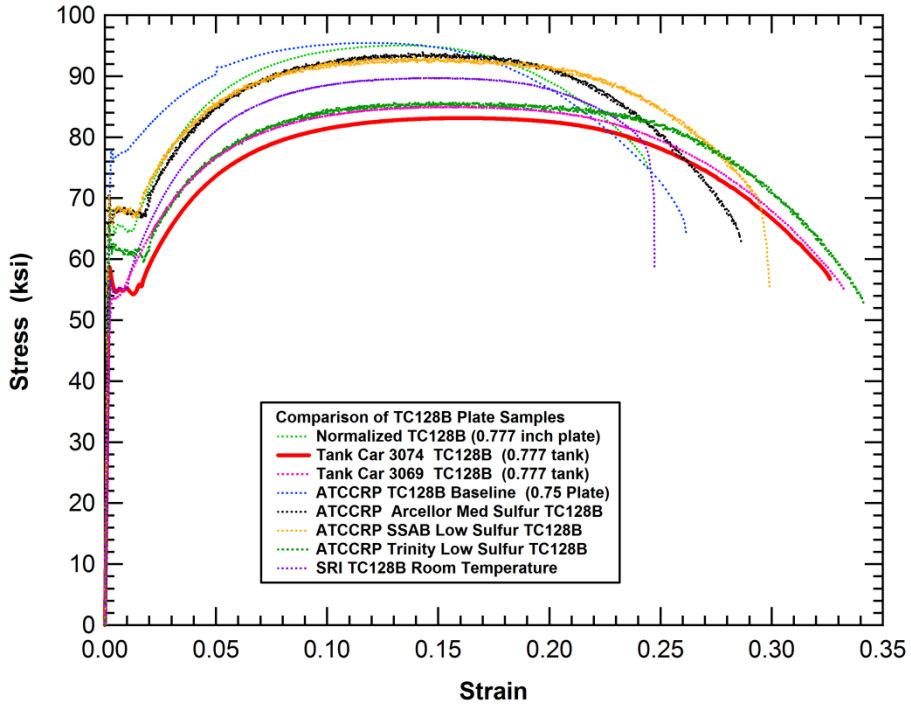

Figure 42. Comparison of tensile stress-strain curves from various TC128B samples.

3.4.1 NGRTC TC128B Material Properties

The material samples characterized in the NGRTC program included:

- two older TC128B plate samples that were removed from the tank cars used for the full-scale side impact tests (Tank Cars 3069 and 3074 materials)
- new (vintage 2007) sample of normalized TC128B (0.777-inch-thick).

The two older plate samples were at the lower end of the strength scale for the range of TC128B materials tested and the new TC128B sample had a significantly higher strength. The comparison of the tensile data for the new material with one of the older tank car samples is provided in Figure 43.

3.4.1.1 NGRTC Tank Car 3069 TC128B Material Properties

The first of the NGRTC TC128B samples characterized was an older material recovered from the test tank car Number 3069. A full set of smooth and notched tensile tests was performed for this material and the tensile test data is summarized in Figure 44.

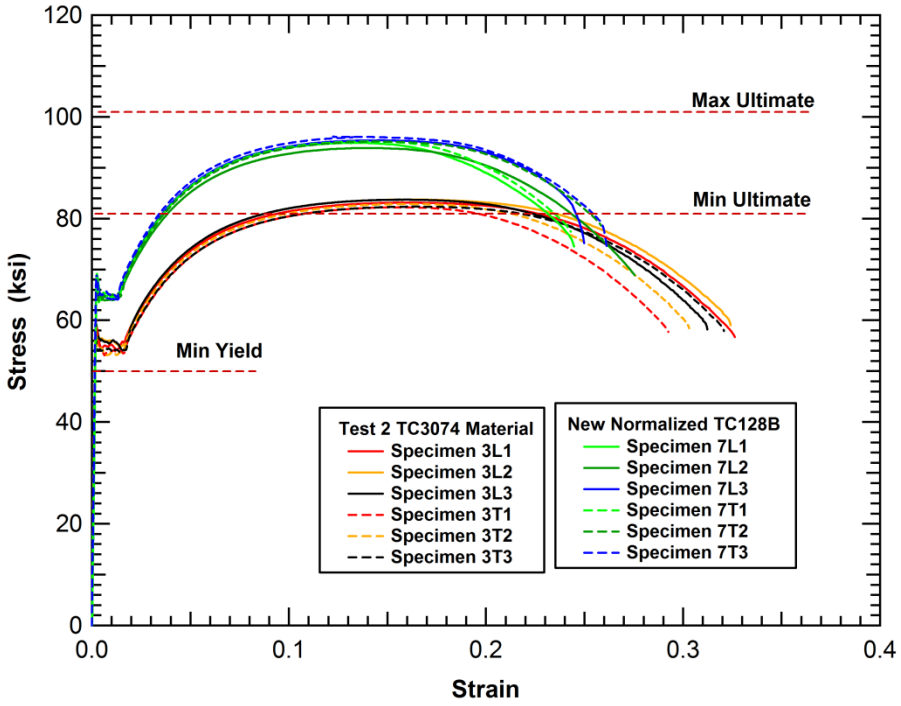

Figure 43. Comparison of tank car puncture analyses with different failure criteria.

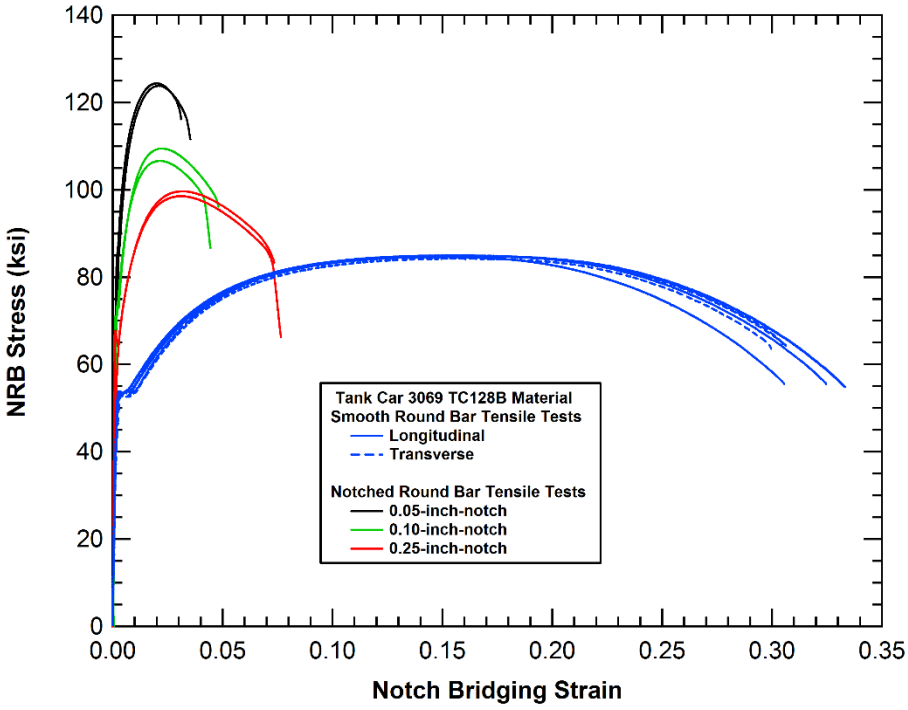

Figure 44. Characterization test data for the NGRTC Tank Car 3069 TC128B plate.

The constitutive parameters for the Tank Car 3069 TC128B material are summarized in Table 21 and the correlation of the constitutive model and tensile test data is shown in Figure 45. For this material, the traditional Bao-Wierzbicki Model (n=1.00) was used. However the comparison of the calculated and measured ductility over the range of stress triaxialities in the tests suggests that a better fit could be obtained with a higher value of a modified Bao-Wierzbicki exponent (n). The effect of mean stress on the yield behavior is also relatively high for this material (compared to the other materials in this study) with a Drucker-Prager yield criterion coefficient (α) equal to 0.120.

Table 21. Material constitutive parameters and tabular stress-strain values for the Tank Car 3069 TC128B

Material Constitutive Parameters		
Bao Wierzbicki Coefficient - A		0.75
Bao Wierzbicki Coefficient - B		2.00
Modified Bao Wierzbicki Coefficient - n		1.00
Drucker Prager Coefficient - α		0.120
Point No.	**Plastic Strain (in/in)**	**True Stress (ksi)**
1	0.00E+00	54.7
2	4.00E-03	54.9
3	2.74E-02	72.5
4	5.40E-02	84.6
5	8.67E-02	92.7
6	1.46E-01	100.0
7	2.60E-01	110.0
8	5.00E-01	128.0
9	1.00E+00	157.0
10	2.44E+00	220.0

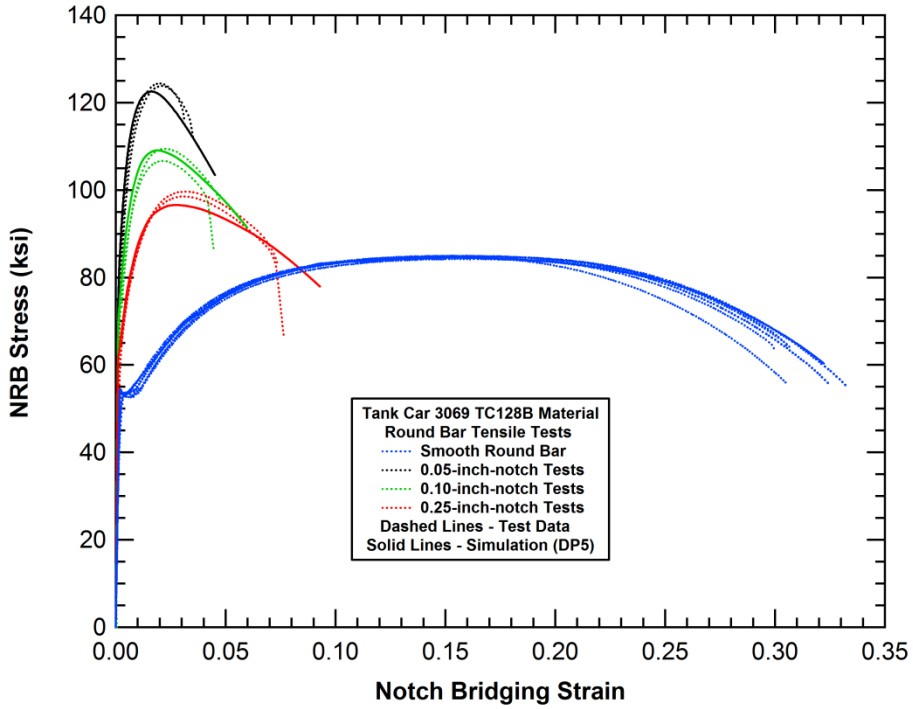

Figure 45. Model calibration for the NGRTC Tank Car 3069 TC128B plate.

3.4.1.2 NGRTC Tank Car 3074 TC128B Material Properties

The second of the NGRTC TC128B samples characterized was an older material recovered from the test tank car Number 3074. A full set of smooth and notched tensile tests was performed for this material and the tensile test data is summarized in Figure 46.

The constitutive parameters for the Tank Car 3074 TC128B material are summarized in Table 22 and the correlation of the constitutive model and tensile test data is shown in Figure 47. For this material, the traditional Bao-Wierzbicki Model (n=1.00) provided a good fit to the measured ductility over the range of stress triaxialities in the tests. The effect of mean stress on the yield behavior is moderate for this material (compared to the other materials in this study) with a Drucker-Prager yield criterion coefficient (α) equal to 0.050.

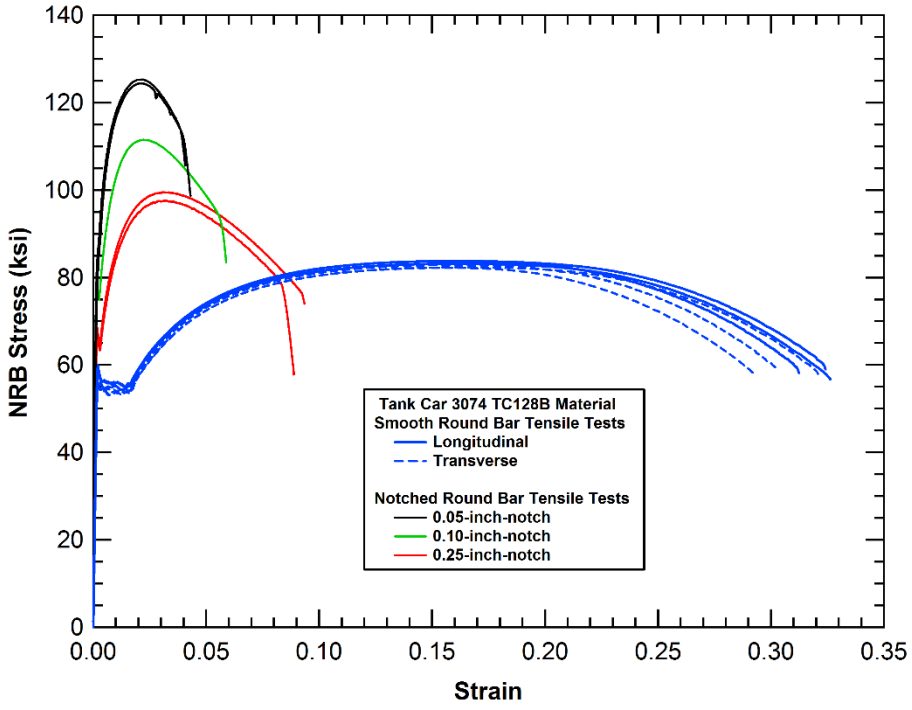

Figure 46. Characterization test data for the NGRTC Tank Car 3074 TC128B plate.

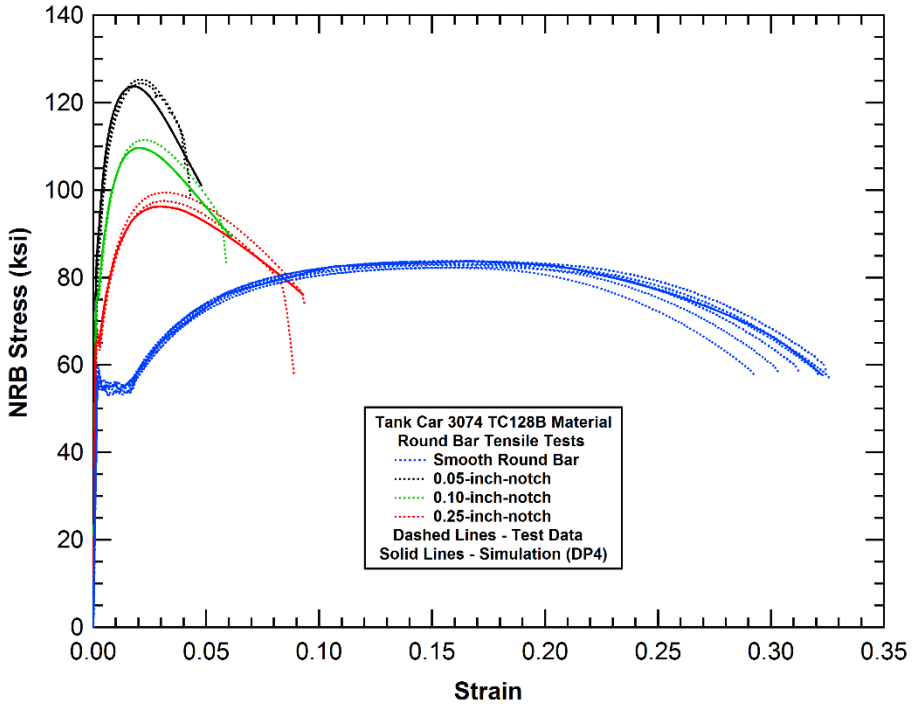

Figure 47. Model calibration for the NGRTC Tank Car 3074 TC128B plate.

Table 22. Material constitutive parameters and tabular stress-strain values for the Tank Car 3074 TC128B

Material Constitutive Parameters		
Bao Wierzbicki Coefficient - A		0.75
Bao Wierzbicki Coefficient - B		2.00
Modified Bao Wierzbicki Coefficient - n		1.00
Drucker Prager Coefficient - α		0.050
Point No.	**Plastic Strain (in/in)**	**True Stress (ksi)**
1	0.00E+00	58.5
2	1.20E-03	55.1
3	1.30E-02	55.3
4	2.76E-02	67.1
5	5.41E-02	80.2
6	9.87E-02	90.9
7	1.58E-01	97.9
8	2.50E-01	105.5
9	8.55E-01	140.0
10	2.17E+00	170.0

3.4.1.3 NGRTC Tank Car New Normalized 0.777-inch TC128B Plate Material Properties

The third of the NGRTC TC128B samples characterized was a section from a 0.777-inch-thick plate of new TC128B material that was normalized. A full set of smooth and notched tensile tests was performed for this material and the tensile test data is summarized in Figure 48.

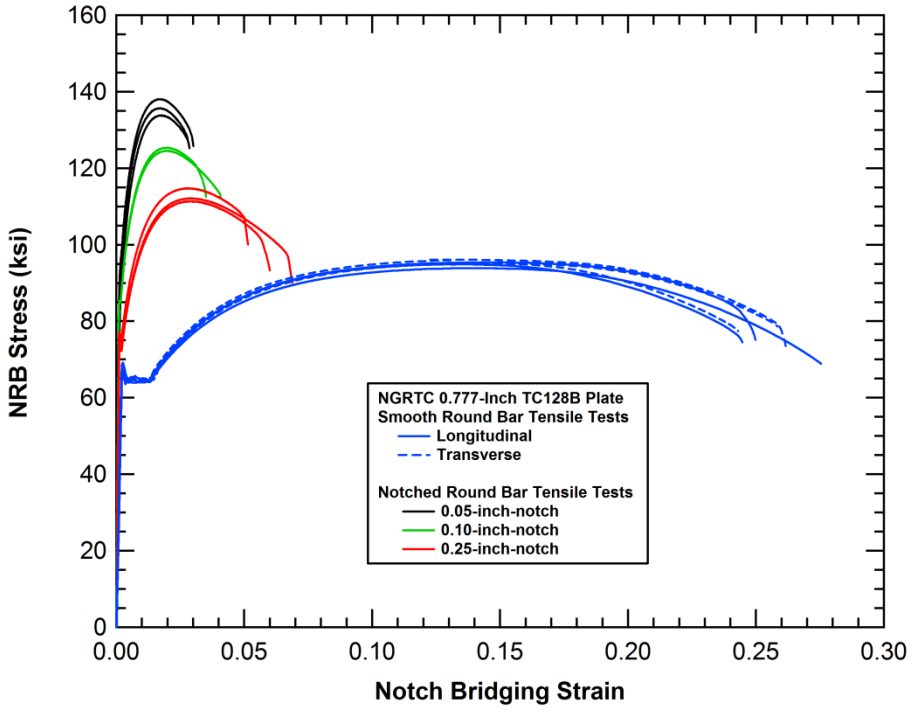

Figure 48. Characterization test data for the NGRTC new normalized 0.777-inch TC128B plate.

The constitutive parameters for the 0.777-inch-thick plate of new TC128B are summarized in Table 23 and the correlation of the material constitutive model and material calibration tensile test data is shown in Figure 49. For this material, the traditional Bao-Wierzbicki Model (n=1.00) provided a good fit to the measured ductility over the range of stress triaxialities in the tests. The effect of mean stress on the yield behavior is quite high for this material (compared to the other materials in this study) with a Drucker-Prager yield criterion coefficient (α) equal to 0.195.

Tank Car 3069 TC128B Material Characterization & Model Calibration -Figure 49. Modified Bao-Wierzbicki Model (n=1.00), Drucker-Prager Yield Criterion (a=0.195), High Resolution Analysis

Table 23. Material constitutive parameters and tabular stress-strain values for the new normalized 0.777-inch TC128B

Material Constitutive Parameters		
Bao Wierzbicki Coefficient - A		0.75
Bao Wierzbicki Coefficient - B		2.00
Modified Bao Wierzbicki Coefficient - n		1.00
Drucker Prager Coefficient - α		0.195
Point No.	**Plastic Strain (in/in)**	**True Stress (ksi)**
1	0.00E+00	73.4
2	1.52E-03	70.0
3	1.05E-02	69.1
4	2.22E-02	82.2
5	5.36E-02	100.2
6	9.82E-02	111.8
7	1.50E-01	118.5
8	2.50E-01	128.5
9	5.00E-01	143.5
10	1.25E+00	180.0

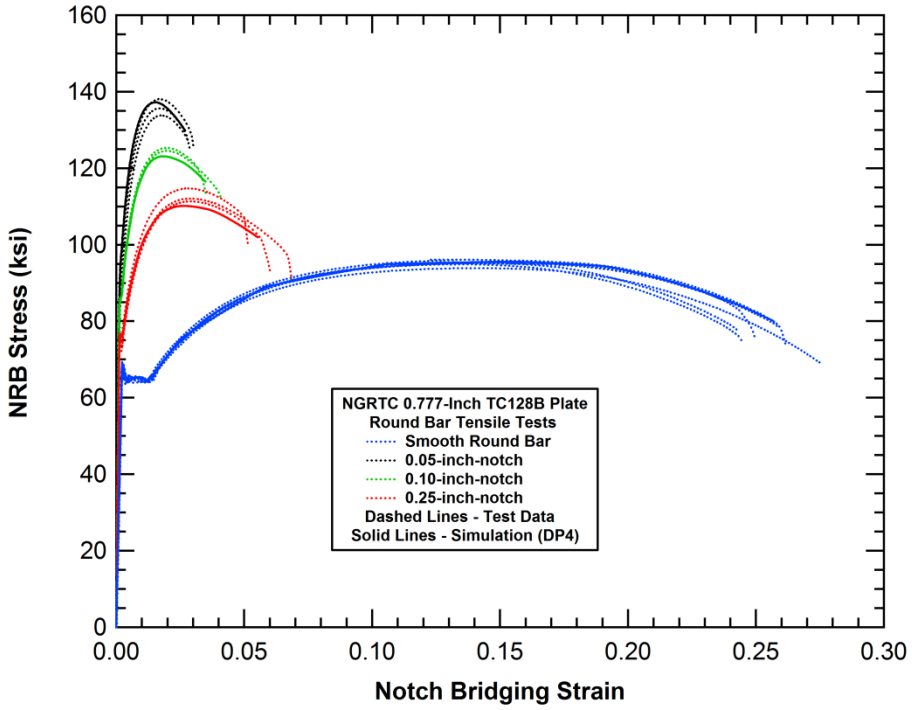

Figure 49. Model calibration for the NGRTC new normalized 0.777-inch TC128B plate.

3.4.2 ATCCRP TC128B Material Properties

The first of the ATCCRP TC128B materials was a sample of 0.750-inch-thick plate and was tested as part of the Phase I test program (shown previously in Figure 38). A full set of smooth and notched tensile tests was performed for this material and the tensile test data is summarized in Figure 50.

The constitutive parameters for the 0.750-inch-thick TC128B plate are summarized in Table 24 and the correlation of the material constitutive model and material calibration tensile test data is shown in Figure 51. For this material, the traditional Bao-Wierzbicki Model (n=1.00) provided a good fit to the measured ductility over the range of stress triaxialities in the tests. The effect of mean stress on the yield behavior is moderate for this material (compared to the other materials in this study) with a Drucker-Prager yield criterion coefficient (α) equal to 0.040.

The other three ATCCRP TC128B materials were tested in Phase II and were chosen with an emphasis on evaluating the effects of reduced sulfur levels on the material performance. The first of these three was the Arcelor Medium Sulfur TC128B plate. A full set of smooth and notched tensile tests was performed for this material and the tensile test data is summarized in Figure 52.

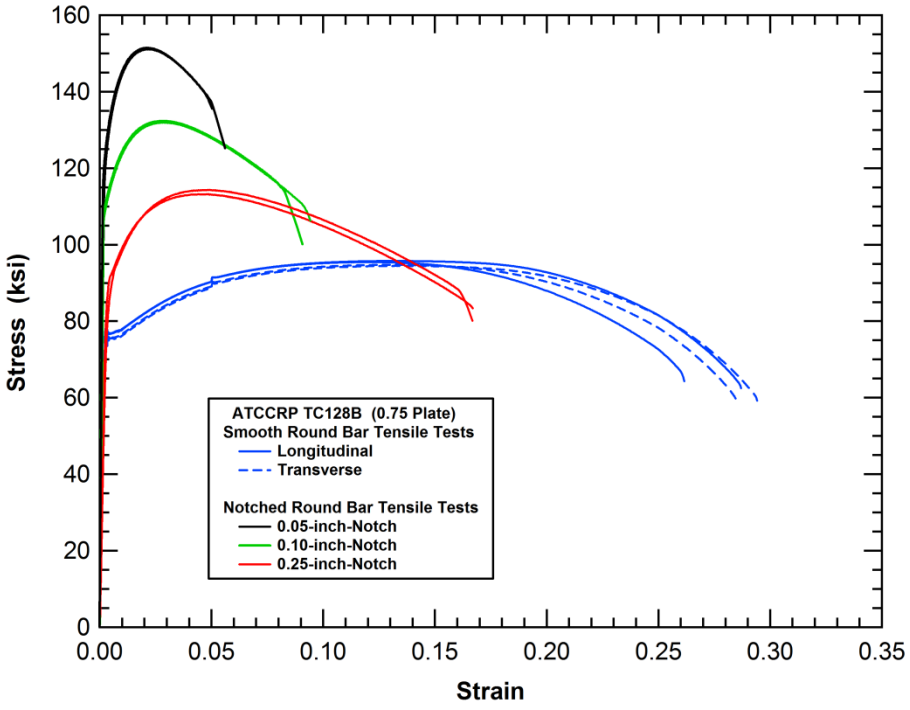

Figure 50. Characterization test data for the baseline ATCCRP 0.750-inch TC128B plate.

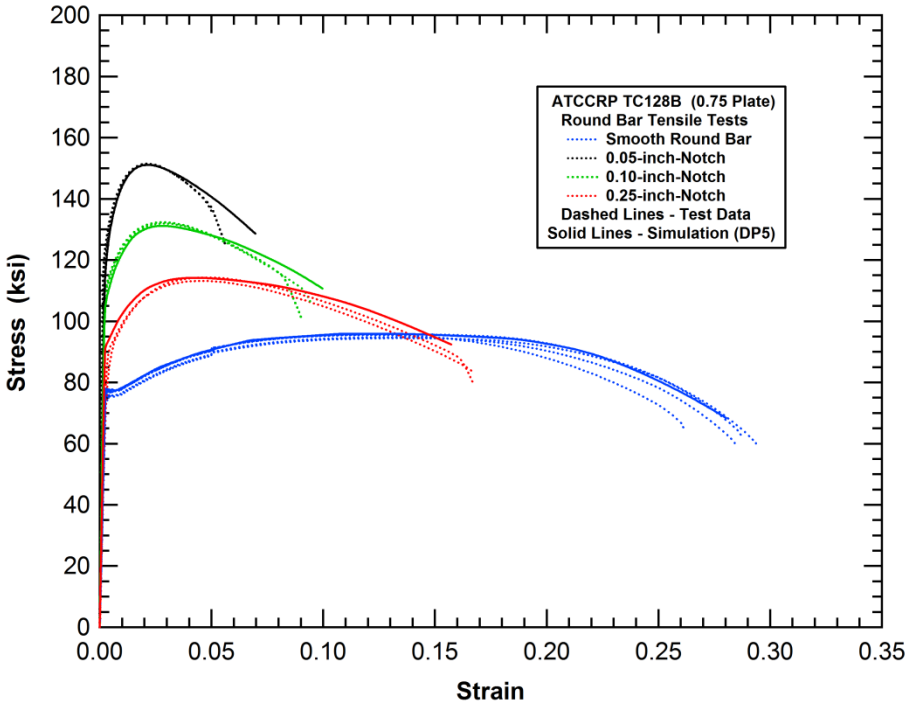

Figure 51. Model calibration for the baseline ATCCRP 0.750-inch TC128B plate.

Table 24. Material constitutive parameters and tabular stress-strain values for the ATCCRP 0.750-inch TC128B

Material Constitutive Parameters		
Bao Wierzbicki Coefficient - A		1.20
Bao Wierzbicki Coefficient - B		1.80
Modified Bao Wierzbicki Coefficient - n		1.00
Drucker Prager Coefficient - α		0.040
Point No.	**Plastic Strain (in/in)**	**True Stress (ksi)**
1	0.00E+00	79.6
2	1.51E-03	78.3
3	5.91E-03	79.0
4	2.38E-02	88.3
5	4.10E-02	94.8
6	6.32E-02	101.5
7	1.03E-01	107.9
8	1.44E-01	112.3
9	2.96E-01	126.7
10	4.45E-01	136.8
11	1.49E+00	177.3

The constitutive parameters for the Arcelor Medium Sulfur TC128B plate are summarized in Table 25 and the correlation of the material constitutive model and material calibration tensile test data is shown in Figure 53. For this material, the Modified Bao-Wierzbicki Model was required to predict the ductility for the higher triaxiality levels (n=1.50). The effect of mean stress on the yield behavior is moderate for this material (compared to the other materials in this study) with a Drucker-Prager yield criterion coefficient (α) equal to 0.050.

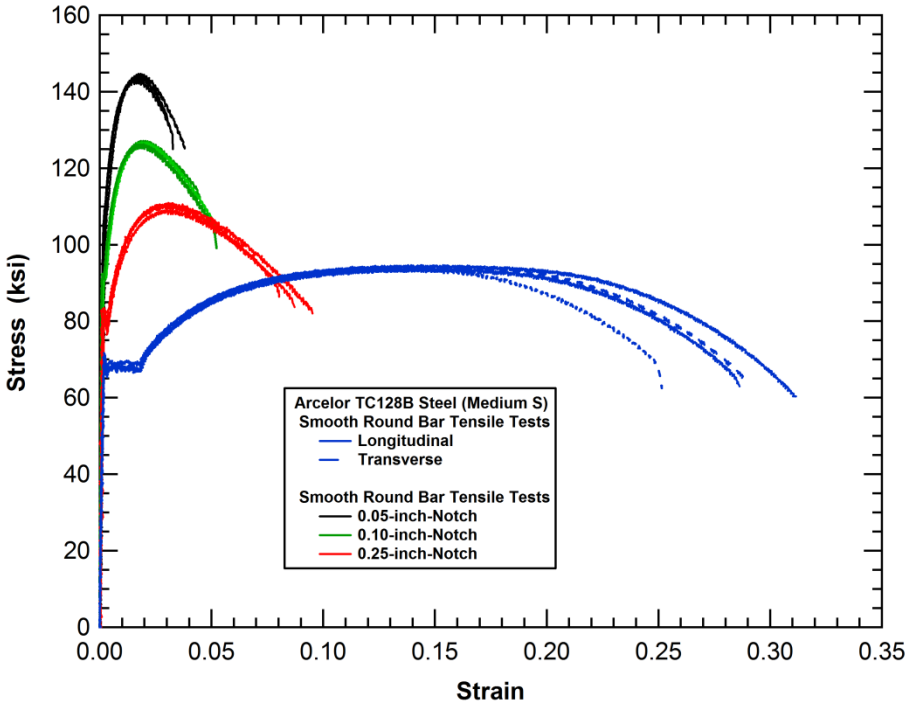

Figure 52. Characterization test data for the baseline ATCCRP Arcelor Medium Sulfur TC128B plate.

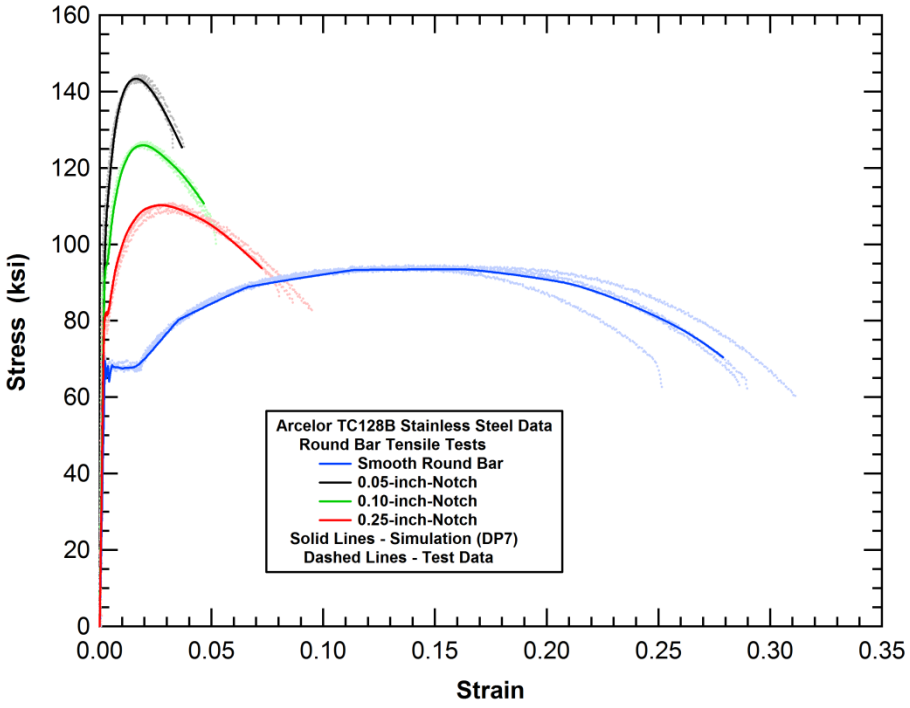

Figure 53. Model calibration for the Arcelor Medium Sulfur TC128B plate.

Table 25. Material constitutive parameters and tabular stress-strain values for the Arcelor Medium Sulfur TC128B

Material Constitutive Parameters		
Bao Wierzbicki Coefficient - A		1.00
Bao Wierzbicki Coefficient - B		1.50
Modified Bao Wierzbicki Coefficient - n		1.00
Drucker Prager Coefficient - α		0.050
Point No.	**Plastic Strain (in/in)**	**True Stress (ksi)**
1	0.00E+00	72.0
2	5.89E-04	67.7
3	3.52E-03	69.5
4	1.45E-02	69.5
5	3.20E-02	84.4
6	6.16E-02	96.3
7	1.06E-01	105.7
8	1.71E-01	112.9
9	3.46E-01	126.0
10	7.00E-01	142.5
11	2.09E+00	175.0

The second ATCCRP TC128B material tested in Phase II was the SSAB Low Sulfur TC128B plate. A full set of smooth and notched tensile tests was performed for this material and the tensile test data is summarized in Figure 54.

The constitutive parameters for the SSAB Low Sulfur TC128B plate are summarized in Table 26 and the correlation of the material constitutive model and material calibration tensile test data is shown in Figure 55. For this material, the Modified Bao-Wierzbicki Model was required to predict the ductility for the higher triaxiality levels (n=1.60). The effect of mean stress on the yield behavior is moderate for this material (compared to the other materials in this study) with a Drucker-Prager yield criterion coefficient (α) equal to 0.050.

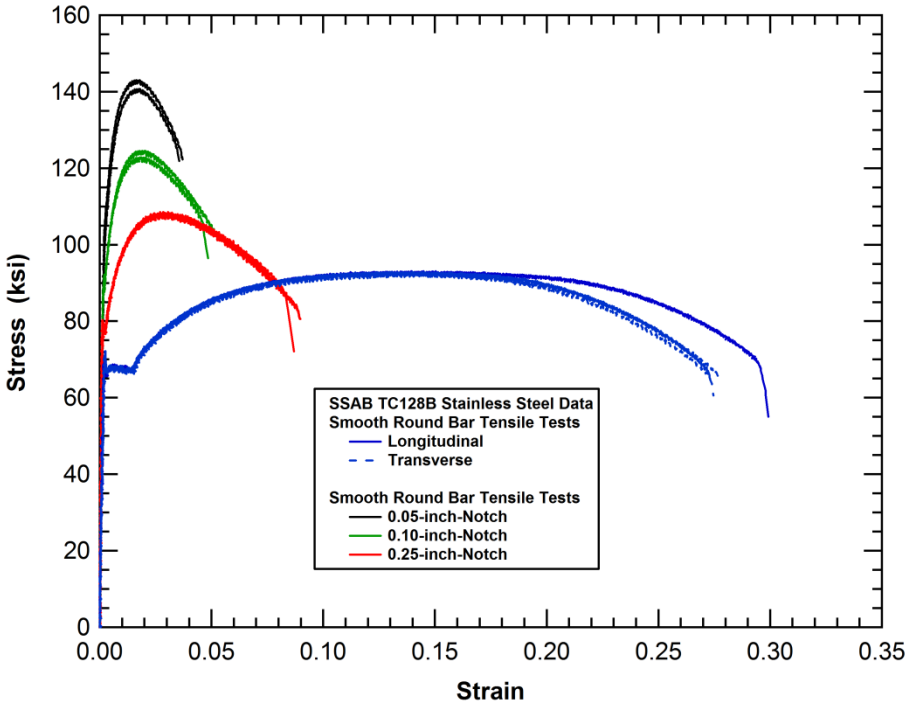

Figure 54. Characterization test data for the baseline ATCCRP SSAB Low Sulfur TC128B plate.

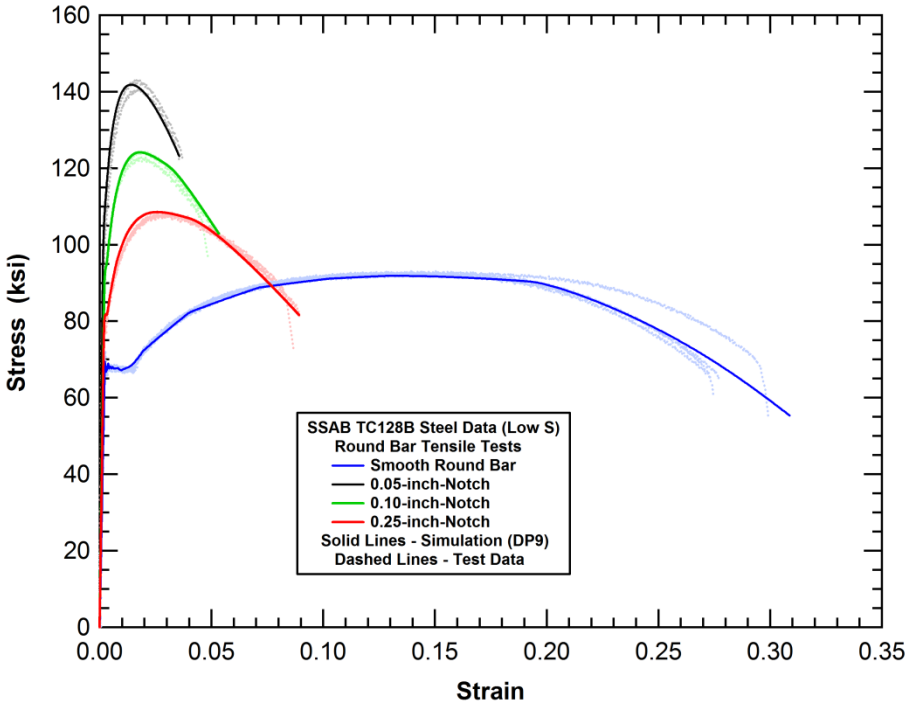

Figure 55. Model calibration for the SSAB Low Sulfur TC128B plate.

Table 26. Material constitutive parameters and tabular stress-strain values for the SSAB Low Sulfur TC128B

Material Constitutive Parameters		
Bao Wierzbicki Coefficient - A		1.40
Bao Wierzbicki Coefficient - B		3.75
Modified Bao Wierzbicki Coefficient - n		1.60
Drucker Prager Coefficient - α		0.050
Point No.	**Plastic Strain (in/in)**	**True Stress (ksi)**
1	0.00E+00	71.5
2	3.88E-04	69.3
3	1.15E-02	69.2
4	1.73E-02	75.0
5	3.69E-02	87.0
6	6.65E-02	96.7
7	9.63E-02	102.2
8	1.24E-01	106.0
9	1.56E-01	109.1
10	2.96E-01	122.0
11	1.99E+00	194.0

The third ATCCRP TC128B material tested in Phase II was the Trinity Low Sulfur TC128B plate. A full set of smooth and notched tensile tests was performed for this material and the tensile test data is summarized in Figure 56.

The constitutive parameters for the Trinity Low Sulfur TC128B plate are summarized in Table 27 and the correlation of the material constitutive model and material calibration tensile test data is shown in Figure 57. For this material, the traditional Bao-Wierzbicki Model (n=1.00) provided a good fit to the measured ductility over the range of stress triaxialities in the tests. The effect of mean stress on the yield behavior is moderate for this material (compared to the other materials in this study) with a Drucker-Prager yield criterion coefficient (α) equal to 0.050.

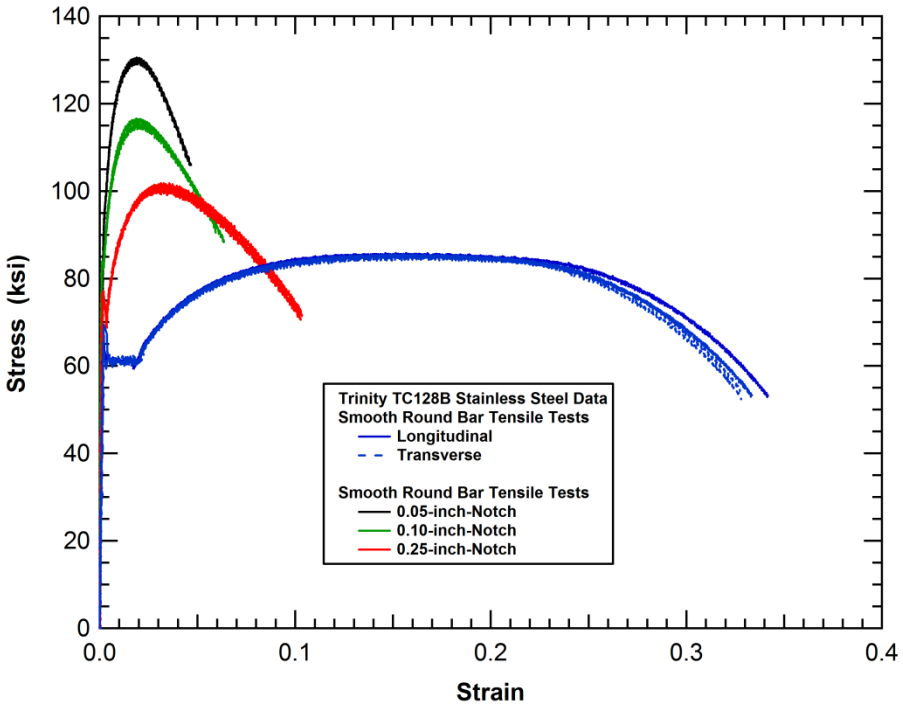

Figure 56. Characterization test data for the baseline ATCCRP Trinity Low Sulfur TC128B plate.

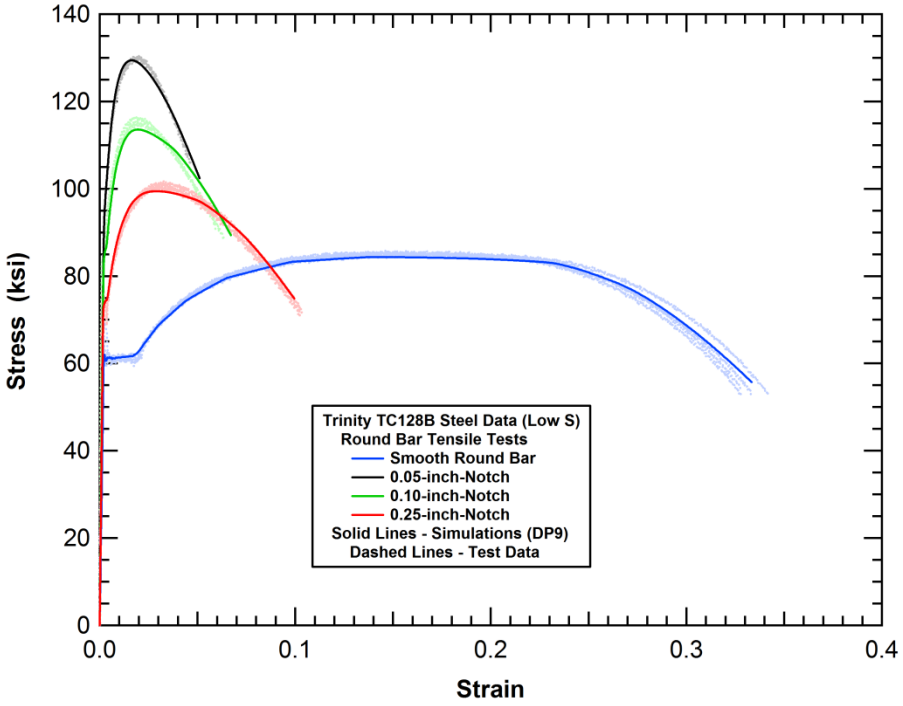

Figure 57. Model calibration for the Trinity Low Sulfur TC128B plate.

Table 27. Material constitutive parameters and tabular stress-strain values for the Trinity Low Sulfur TC128B

Material Constitutive Parameters		
Bao Wierzbicki Coefficient - A		0.85
Bao Wierzbicki Coefficient - B		2.20
Modified Bao Wierzbicki Coefficient - n		1.00
Drucker Prager Coefficient - α		0.050
Point No.	**Plastic Strain (in/in)**	**True Stress (ksi)**
1	0.00E+00	64.5
2	1.17E-03	62.1
3	1.77E-02	64.0
4	2.06E-02	66.9
5	2.74E-02	72.0
6	4.11E-02	79.0
7	6.05E-02	86.1
8	9.14E-02	92.9
9	1.31E-01	98.0
10	3.56E-01	119.2
11	5.63E-01	131.0
12	1.18E+00	153.0

3.5 Evaluation of Puncture Resistance for Alternative Tank Car Materials

An objective of this project is to assess the combination of material properties that will guide the search for optimization of the tank car material selection. To assist in this effort we evaluated the puncture performance of a set of candidate steels with significantly different properties from TC128B as shown in Figure 58. Note that these candidate steels were selected based on their mechanical properties and availability of test data and not necessarily for their suitability for use in railroad tank car service (e.g. weldability, fatigue resistance, cost). The idea is that once the

desirable mechanical properties were identified, the selection of a tank car material that optimizes the desirable properties could be identified.

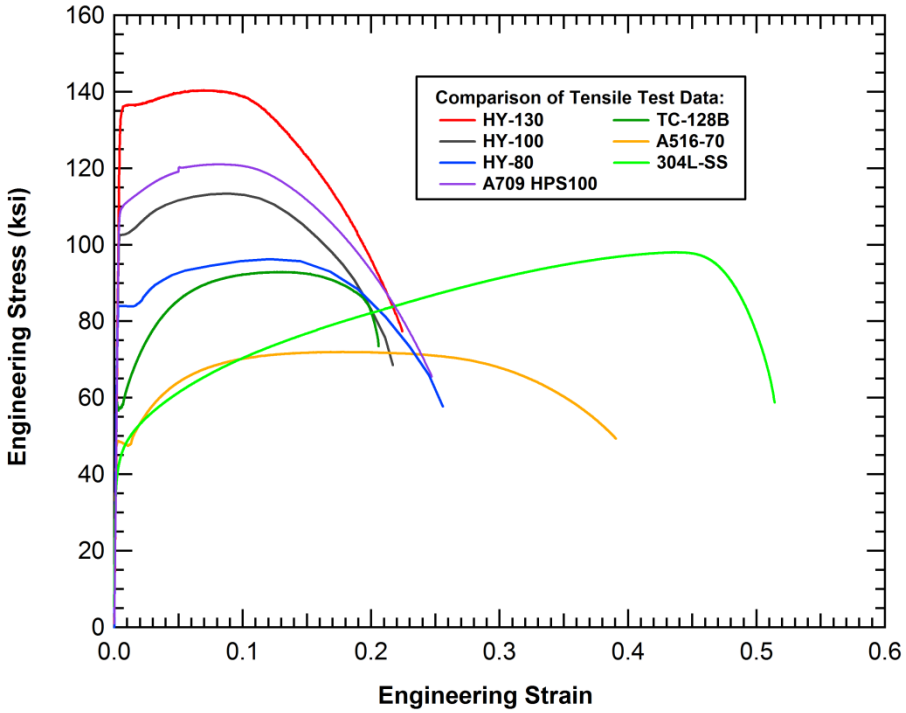

Figure 58. Candidate tank car steels with a range of mechanical properties.

The methodology that will be applied is:

1. Use existing data to develop constitutive and BW failure parameters and validate against material test data.
2. Simulate a series of side impact puncture conditions on a 105J600I chlorine tank car design with each candidate material. Compare results to the corresponding TC128B tank car design.
3. Evaluate the comparisons of the different materials to assess the influence of various material characteristics (e.g. yield, ultimate, elongation) on puncture resistance.

3.5.1 Tank Car Puncture Modeling

The BW failure models and constitutive model fits developed in this program can be used with the previously developed tank car puncture prediction capability to assess the material effects on puncture performance. This tank car impact and puncture modeling capability was previously developed and applied in multiple studies [1, 50] to evaluate a wide range of tank designs. The side impact condition was a normal impact centered on the belt line of the tank.

The baseline failure models use a fine mesh of solid brick elements in the impact zone with an element dimension of approximately 0.040 inch (1 mm). The mesh transitions to shell elements outside the impact zone with increasing mesh coarseness. The model of the commodity tank and BW impact zone mesh used in the tank shell puncture analyses is shown in Figure 59. An existing algorithm in LS-DYNA is used to tie the edge of the shell elements to the solid elements around the edge of the impact zone.

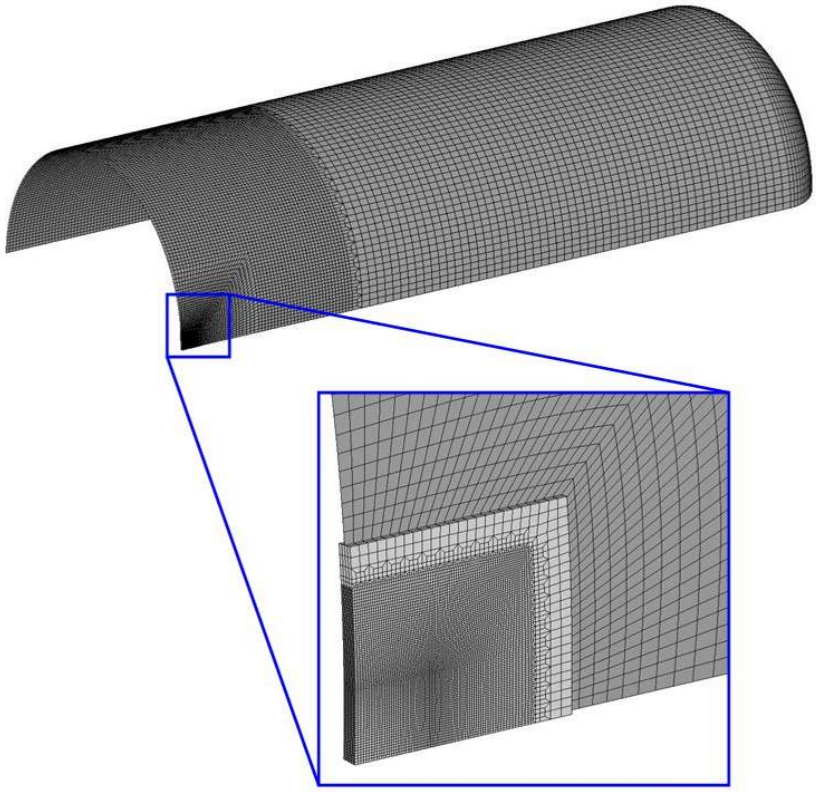

Figure 59. Tank model and impact zone mesh used for side impact puncture analyses.

As a result of the very fine mesh in the impact zone, the puncture models were significantly larger and have correspondingly longer run times. To allow for the evaluation of a wide range of impact conditions and tank geometries, some simplifications in the tank model were implemented.

The first simplification was the use of symmetry planes. For the majority of side impact analyses described in this section, two symmetry planes were used to reduce the model to one-quarter of the full tank (a half model was used for the offset head impacts). This had a small effect since some tank car structural details could not be included in the quarter model (e.g. manway and bolsters). The primary effect of this approximation was that a side impact centered on the tank may have a slightly reduced stiffness for large dent sizes since the manway and surrounding structures are stiffer than the bare commodity tank.

An example impact and puncture simulation is shown in Figure 60. The tank is backed by a rigid wall and impacted with a rigid impactor. Due to the vertical symmetry appproximation, no gravitational loads are applied. The tank is deformed locally by the impact and when sufficiently large impact forces develop, the impactor punctures the tank. A detailed view of the puncture behavior is shown in Figure 61.

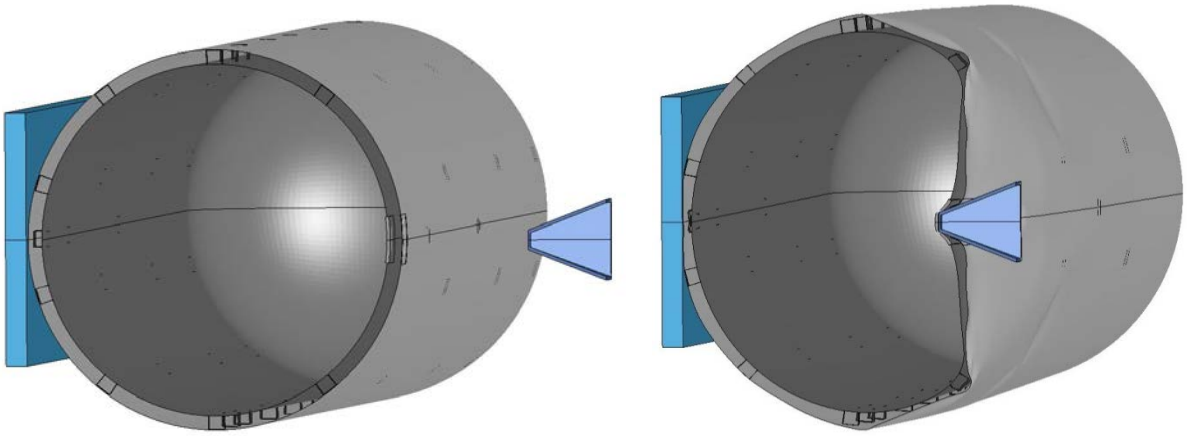

(a) Initial impact geometry **(b) Puncture response of the tank**

Figure 60. Detailed impact and puncture sequence for a 600 lb chlorine car.

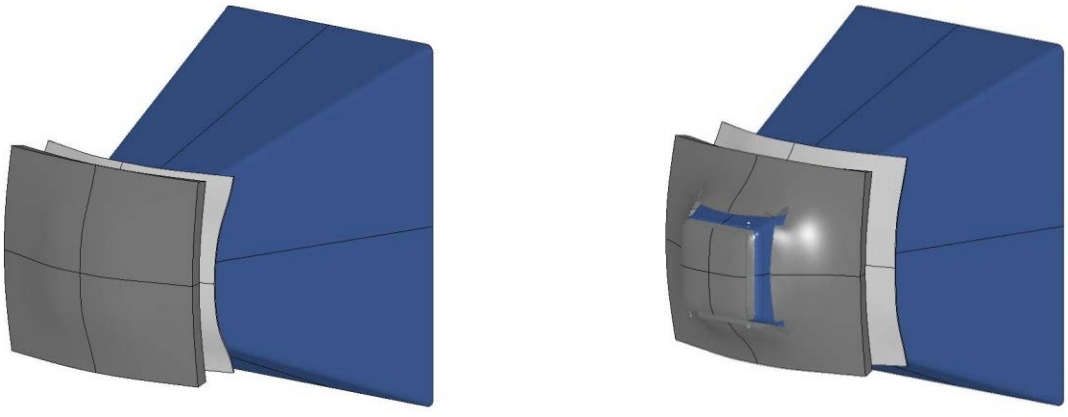

(a) Initial impact deformations **(b) Tank puncture response**

Figure 61. Calculated puncture initiation and fracture progression.

The first set of analyses used 3x3, 3x6, 6x6, 9x9, 12x12, 3x12, 12x3 rectangular impactors, all with a 0.50-inch radius around the edges. The third set of tank impact analyses performed used round impactor face profiles to investigate the effects of the impactor shape. The additional impactors used were a 5.73, 7.64, 9.55, 11.46, and 13.37 inch diameter impactors (ram face perimeter lengths of 18, 24, 30, 36, and 42 inch, respectively).

The calculated puncture forces and puncture energies for the various materials and various impactors in normal side impact conditions are summarized in Figure 62 and Figure 63, respectively. The puncture parameters in the figures are plotted against the impactor "characteristic size" defined as the square root of the area of the impactor face [50]. This parameter was found to be a good surrogate of impactor puncture threat for different impactor shapes. The fits to the data provide some insight to the relative performance for these impacts. However, we need a methodology that can summarize the relative performance of all of the impact conditions analyzed in a simpler format.

The methodology selected to compare the relative performance of each material was to normalize the puncture performance metrics (force and energy) for each impact condition to the corresponding performance of the TC128B tank under the identical impact conditions as described in Equations 29 and 30. In the equation, the subscript (i) corresponds to the index number of the specific impact scenario being analyzed.

$$F_{n1} = \frac{F_i}{F_i^{TC128B}} \tag{29}$$

$$E_{n1} = \frac{E_i}{E_i^{TC128B}} \tag{30}$$

These summaries of the normalized puncture forces and energies for all of the impact analyses performed are summarized in Figure 64 and Figure 65, respectively. It is interesting to note that the relative improvements in puncture force and puncture energy are not proportional for different candidate materials. For example, the 304L stainless produces the highest average normalized puncture energy (55% improvement over TC128B) but only a 17% improvement in average normalized puncture force which is less than three other materials (HY-100, A709 HPS100, and HY-130). The relative improvements in the puncture forces and puncture energies from the different materials are also reasonably consistent across the range of different impactor sizes and shapes analyzed.

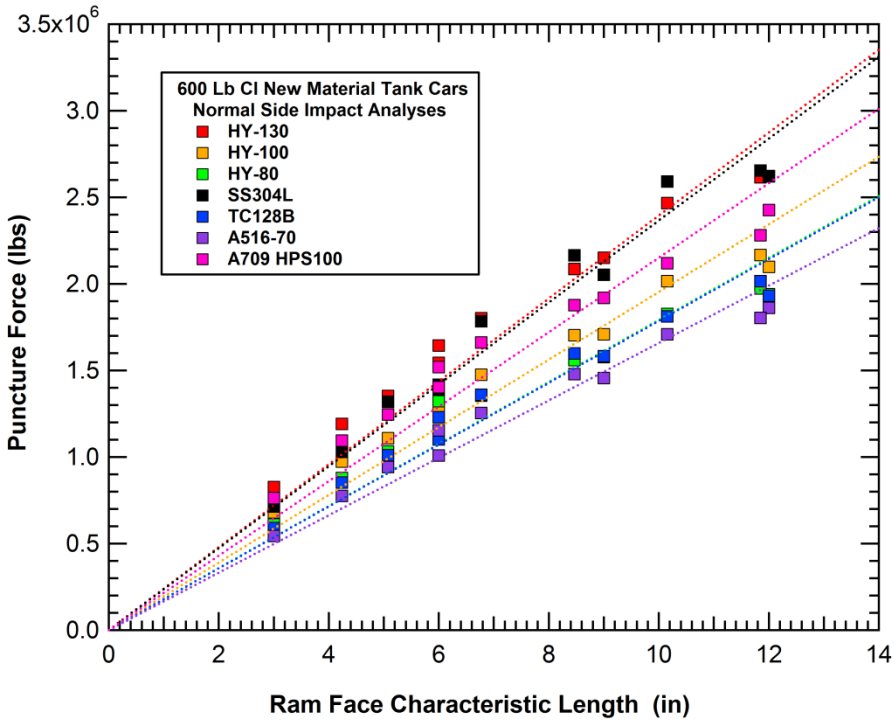

Figure 62. Calculated puncture forces for candidate tank car steels.

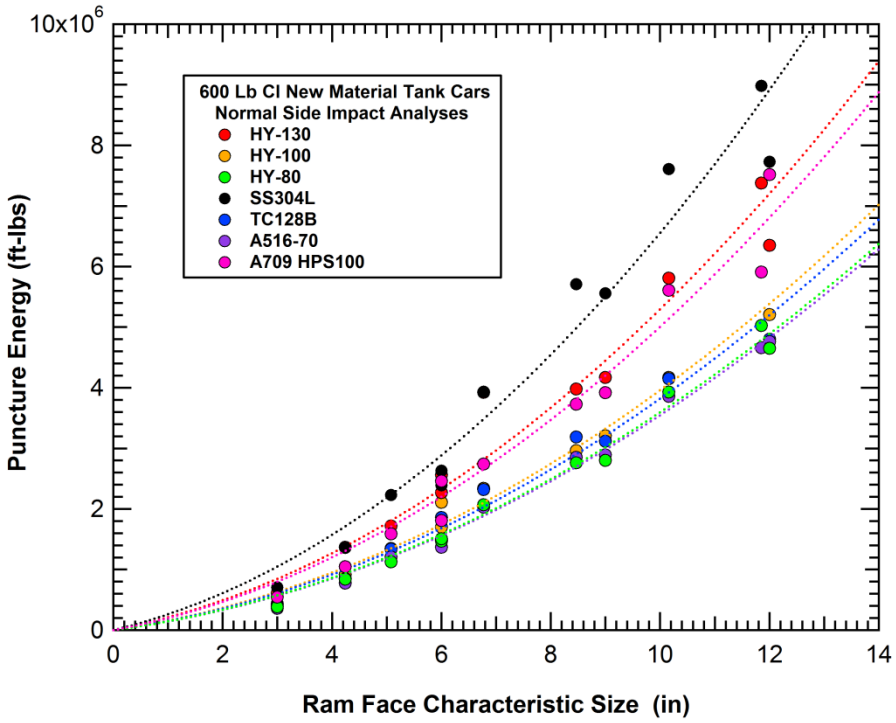

Figure 63. Calculated puncture energies for candidate tank car steels.

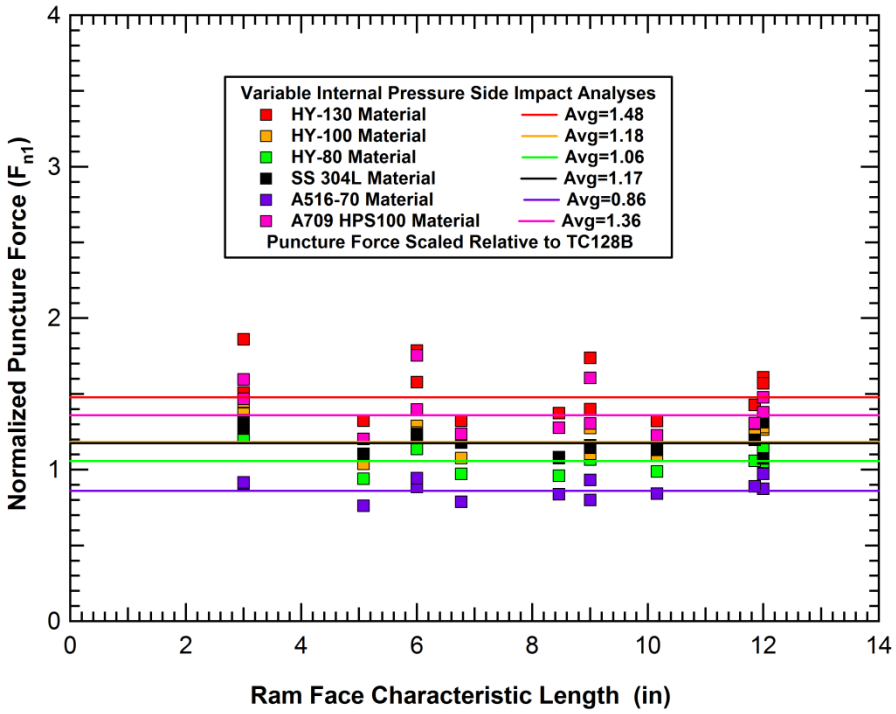

Figure 64. Relative puncture force performance for candidate tank car steels.

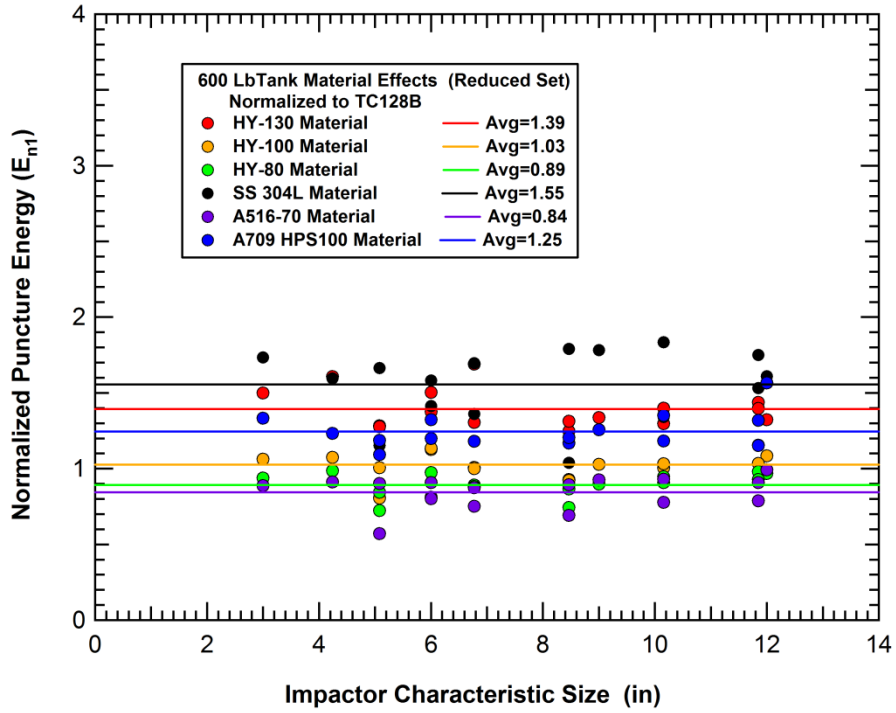

Figure 65. Relative puncture energy performance for candidate tank car steels.

The normalized puncture energies are overlayed with the corresponding normalized curve of impact energy versus normalized speed in Figure 66. The values correspond to an approximately 6% reduction in puncture speed for A516-70 material and a 24% increase in puncture speed for the 304L stainless steel. Note that these values are for the idealized impact scenario restrained by the rigid impact wall. The corresponding variations in puncture probabilities for real world impact conditions may be considerably different.

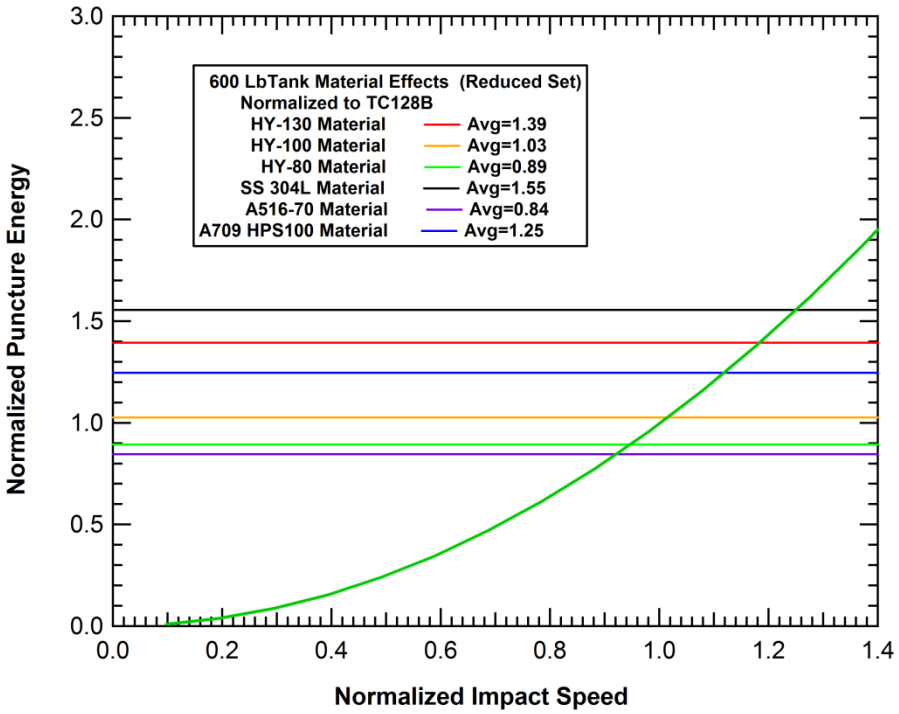

Figure 66. Relative puncture protection performance for candidate tank car steels.

3.6 Tank Car Puncture Modeling

The work presented so far has included results from extensive computer simulations of puncture performance as well as experimental results detailing the properties of a variety of different materials. The purpose of this section is to re-examine the computer simulations of puncture in the context of the impact of the different stress-strain properties derived for the materials.

3.6.1 Description of Different Stress-Strain Curve Parameters

Prior to examining the modeling results in the context of different material properties, it is useful to review the basic data obtained from a material strength test. A representative stress-strain curve for a material is shown in Figure 67 denoting several key quantities that are used to characterize the tensile response, specifically the strength and ductility, of the material. The typical key parameters from a tensile test include the yield strength (usually 0.2% strain offset),

the ultimate strength and the elongation at failure or rupture (denoted σ_Y, σ_U and e_R in Figure 67). Although other parameters are sometimes included (for instance stiffness, or modulus, and another measure of ductility, reduction of area), these are the key parameters typically used to quantify tensile behavior.

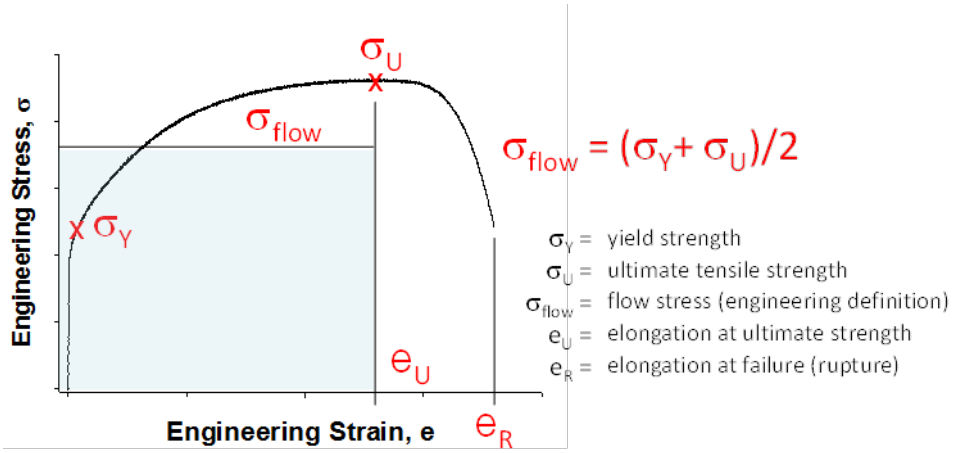

Figure 67. Definition of the characterization of a material's stress-strain behavior.

The yield and ultimate strength (as well as modulus) are considered material properties, somewhat independent of test method, given that typical test methodologies have been used to derive these properties. However, the ductility measurement, percent elongation, is a structural quantity (not a material property) that depends on the method used to measure it. For instance, the gage length of the specimen as well as the shape of the specimen used to measure percent elongation can affect elongation results (as recognized by Barba's law, J. Barba, 1880). This non-property (e.g. non-unique) aspect of elongation is an issue that needs to be kept in mind when potentially using elongation as a correlating variable.

One other parameter shown in Figure 67 is the flow stress, defined for convenience as the average between yield and ultimate strength, which can be useful for providing a measure of the area under a stress strain curve. When predicting the energy to puncture, it is not unreasonable to relate this to an energy measure derived from the elastic and plastic strain-energy in a tensile test. However, rather than including all of the energy to rupture in a tensile test (in mechanics, this energy, or work, to rupture is termed the modulus of toughness), only the energy under the stress-strain curve to the ultimate stress will be utilized. This area, shaded in Figure 67, corresponds to the product of flow stress and elongation at ultimate, symbolically $e_U \sigma_{flow}$. Structural modeling experience has indicated that little energy is added after peak load is achieved.

3.6.2 Influence of Stress-Strain Parameters on Puncture Force

In Section 3.5 of this report we have determined the relative puncture protection levels for a range of material types with diverse mechanical properties. However, it is desirable to evaluate the results and develop a predictive model using stress-strain characteristics (e.g. yield strength, ultimate strength, elongation). This model could then be applied to assess the performance of candidate materials and guide the selection or development of new materials. However, before developing the final form of the model, it is beneficial to examine how some of these different stress-strain parameters affect puncture force.

A quick review of the puncture performance and material properties indicates that the material ultimate strength is a significant factor for improving puncture resistance. However the performance is not proportional to only the material ultimate strength. A clear example of this can be seen by the comparison of the performance for TC128B and HY-80 tanks. The comparison of the TC128B and HY-80 material tensile stress-strain curves is shown in Figure 68. The ultimate strength of the HY-80 is approximately 13 ksi higher than the ultimate strength of TC128B (96 ksi versus 83 ksi). Similarly, the yield strength of the HY-80 is approximately 29 ksi higher than the yield strength of TC128B (84 ksi versus 55 ksi). However, in spite of the higher strength of HY-80 compared to TC128B, the average puncture energy for the HY-80 tanks was lower than that of the TC128B tanks in the evaluation of puncture performance described previously (on average, puncture energy for HY-80 was 0.89 as shown in Figure 65, 11% lower than that observed for TC128B).

After evaluating the tank impact and puncture behaviors using a variety of models and methodologies, we have found that the impact and puncture performance can be primarily determined based on yield strength and ultimate strength. However, yield and ultimate strength only partially quantify the tensile behavior of the material; therefore, it may also be important to include a term in the model that quantifies the ductility of the material. In this modeling, the effect of ductility will be examined by including elongation at ultimate strength as well as a form that examines the strain energy in a stress-strain curve up to the ultimate strength of the material. However, before the form of the model is developed, the effect of these different parameters on puncture force will be determined in this section.

The evaluation of the puncture performance, described in Section 3.5 is based on a series of side impact analyses with various impactors at both normal and oblique impact orientations. Each unique impact calculation with a specific tank material and impact condition results in a calculated force deflection behavior for the impactor up to the point at which the tank punctures (at the peak puncture force level). We integrate the impactor force-deflection curve up to the point of tank puncture to calculate the impact energy dissipated (puncture energy).

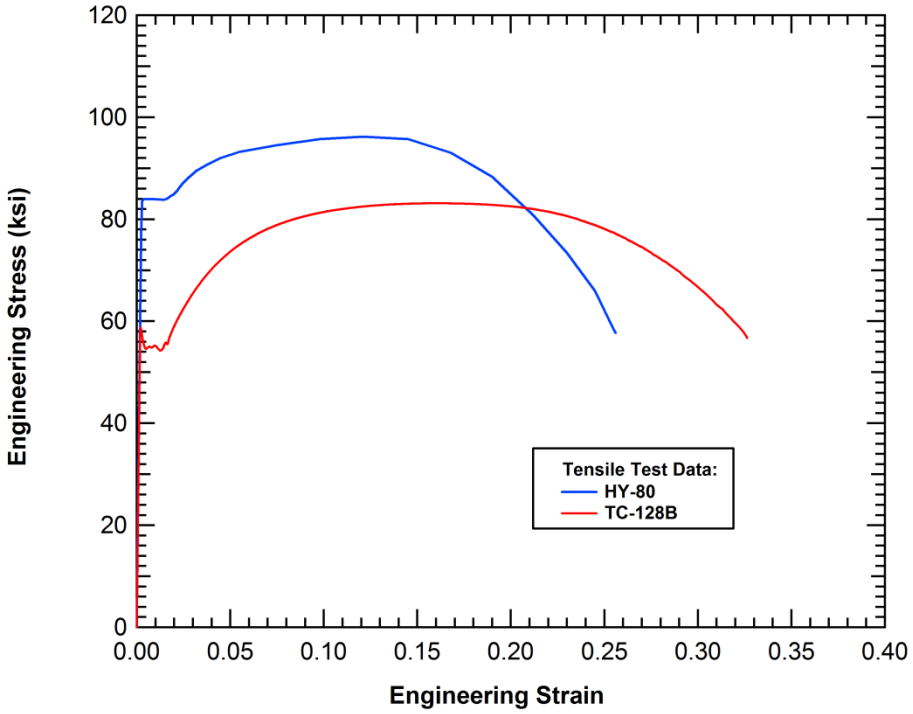

Figure 68. Comparison of the TC128B and HY-80 material tensile stress-strain curves.

The first significant assumption (observation) of the strength model for material performance is that the puncture force for a given impact scenario scales primarily with the ultimate strength. A summary of the relative puncture forces for all of the side impact calculations was provided previously in Figure 64. Remember that this data is the F_{n1} force to puncture the tank scaled relative to the force required to puncture a TC128B tank under identical impact conditions. The average of normalized puncture force over the 18 impact conditions analyzed varies from 0.86 for A516-70 to 1.48 for HT-130. We can demonstrate the influence of ultimate strength on the puncture force by creating a second normalized force that is equivalent to the previous normalized puncture force and scaled by the ratio of the TC128B ultimate strength to the specific material ultimate strength. This normalized force is defined below in Equation 31,

$$F_{n2} = \frac{F_i}{F_i^{TC128B}} \left[\frac{\sigma_u^{TC128B}}{\sigma_u^{Material}} \right] \tag{31}$$

with tabulated results shown in Table 28 and the UTS-corrected F_{n2} plotted in Figure 69.

Table 28. Baseline normalized puncture force scaled with different stress-strain parameters.

Material	Average Normalized (to TC128B) Puncture Force				
	Baseline F_{n1}	σ_U**-corrected** F_{n2}	σ_Y**-corrected** F_{n3}	e_U**-corrected** F_{n4}	$e_U\,\sigma_{flow}$**-corrected** F_{n5}
HY-130	1.48	0.88	0.63	3.38	1.74
HY-100	1.18	0.87	0.67	2.10	1.39
HY-80	1.06	0.93	0.73	1.14	1.12
SS 304L	1.17	1.01	1.66	0.43	0.44
A516-70	0.86	1.00	1.04	0.76	0.91
A709 HPS100	1.36	0.94	0.73	2.42	1.51
average:	***1.19***	***0.94***	***0.91***	***1.71***	***1.19***
std. dev.:	***0.22***	***0.06***	***0.40***	***1.12***	***0.47***
min:	***0.86***	***0.87***	***0.63***	***0.43***	***0.44***
max:	***1.48***	***1.01***	***1.66***	***3.38***	***1.74***

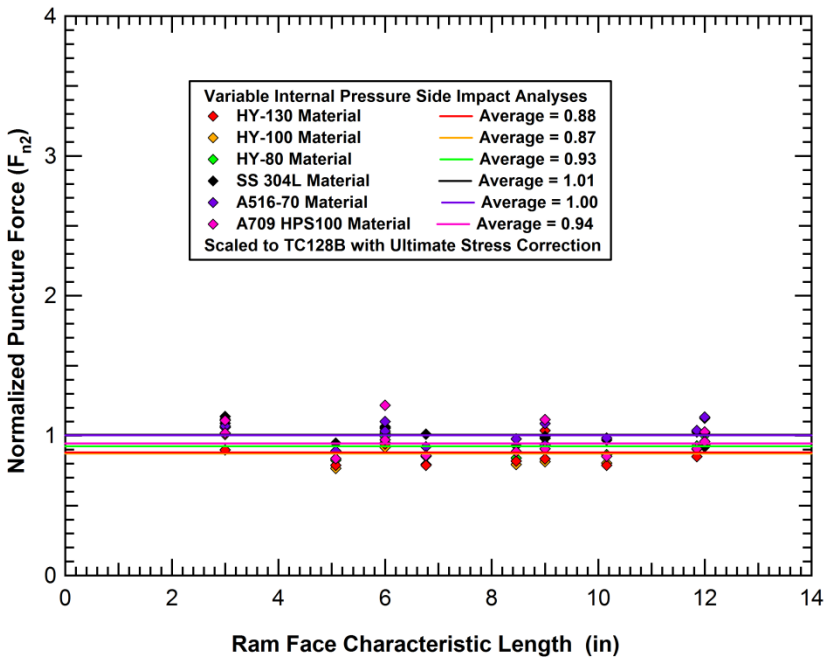

Figure 69. Relative puncture force after ultimate stress correction

The scaling of the puncture forces by the material ultimate strength, shown in Figure 69, significantly reduces the variability in the calculated results (compare to Figure 64). The statistical assessment in Table 28 indicates that standard deviation of the normalized puncture force results is reduced by almost a factor of 4 (compare F_{n1} to F_{n2}, standard deviation reduced from 0.22 to 0.06). This is an indication that the majority of the variation in puncture force is attributable to the material ultimate strength. This is also consistent with a punch-shear failure mechanism where the failure is dominated by exceeding the material strength around the perimeter of the impactor face.

As a further demonstration that the ultimate strength is the most significant factor on the puncture force, yet another normalized force was created that is equivalent to the first normalized puncture force and scaled by the ratio of the TC128B yield strength to the specific material yield strength. This normalized force is defined in Equation 32,

$$F_{n3} = \frac{F_i}{F_i^{TC128B}} \left[\frac{\sigma_y^{TC128B}}{\sigma_y^{Material}} \right] \tag{32}$$

with tabulated results shown in Table 28 and the YS-corrected F_{n3} plotted in Figure 70. Whereas the ultimate strength correction in Figure 69 resulted in lower variability, the data in Table 28 indicates that variability of the data increases when a yield strength correction is applied. Specifically, the standard deviation nearly doubles (compare F_{n1} to F_{n3}, standard deviation increases from 0.22 to 0.40). Given this, the scaling of the puncture forces by the material yield strength does not reduce the variability in the calculated results. This suggests that normalized puncture force varies primarily with tensile strength and less with yield strength (note that this approach looks at the trend with each variable alone, and not a combination of the two effects).

Although yield strength correlates less well than tensile strength, it does have a significant impact on the force deflection curve. This leads to the second significant assumption (observation) of the strength model for material performance is that the impact force deflection curve for a given impact scenario scales primarily with the yield strength. The impact force deflection behavior will have components that are controlled by the tank elastic modulus or internal pressure effects as well as a portion that is dominated by the plastic yielding around the dent. It is assumed that the plastic portion of the impact behavior is controlled by the yield stress at low plastic strain levels.

To demonstrate this effect, consider the set of force-deflection curves for a normal impact with the six inch square impactor on the tanks of the various candidate materials as shown in Figure 71. The curves all show similar behaviors but the magnitude of the force deflection curve is scaled up or down with a ranking order that is similar to the yield strength ranking.

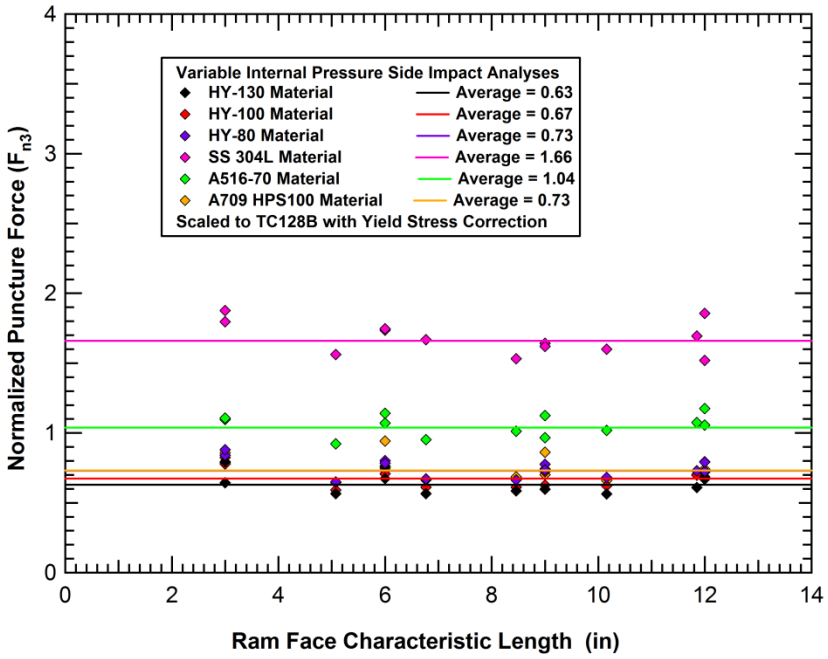

Figure 70. Relative puncture force after yield stress correction

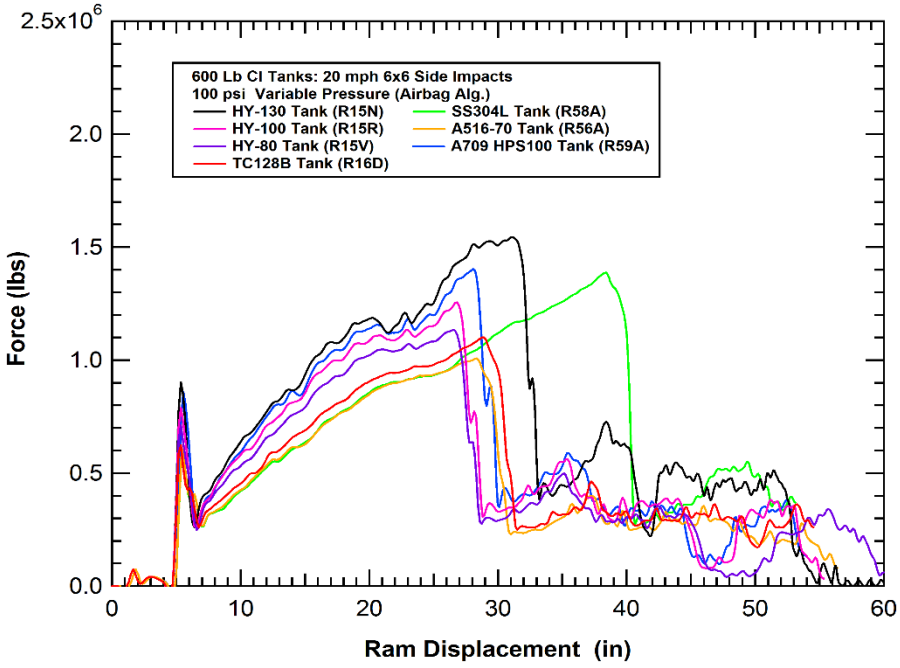

Figure 71. Calculated force deflection curve for various material tanks.

One of the issues in evaluating the yield strength effects is to determine the portion of the behavior that is controlled by the elastic response and the proportion of the curve dominated by the plastic behavior. With a relatively simple trial and error procedure we determined that

approximately 55% of the behavior is controlled by the elastic behavior and 45% is controlled by the plastic response. Thus we can define a yield stress corrected force by the equation:

$$F_y = 0.55F + 0.45F\left[\frac{\sigma_y^{TC128B}}{\sigma_y^{Material}}\right] \tag{33}$$

Using this equation, a plot of the yield strength corrected force-deflection curves for a normal impact with the six inch square impactor on the tanks of the various candidate materials is shown in Figure 72. When comparing Figure 71 and Figure 72, the yield corrected impact force (Figure 72) tends to collapse the dispersed data onto a single characteristic, corrected force deflection curve. The points at which the tank is punctured vary as expected based on the material ultimate strengths. The one curve that diverges at the higher displacements in Figure 72 is the 304L stainless steel tank. It is believed that this is a consequence of the significant strain hardening of this material at relatively low strain levels increasing the level of force in the large deflection portion of the curve. Although the yield corrected impact force does a reasonable job collapsing the data, the outlier for stainless steel suggests that not all of the different material behaviors are captured by yield strength effects alone. Given that, this indicates a potential need for including an additional stress-strain characterization parameter, perhaps ductility (elongation).

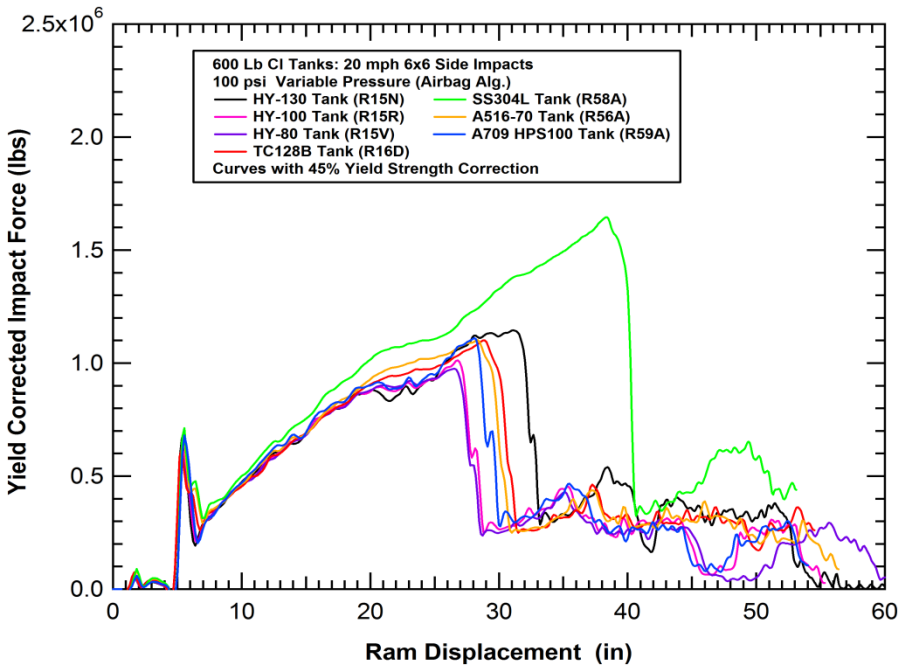

Figure 72. Calculated force deflection curve for various materials with yield stress corrections.

The preceding evaluations have used a method to illustrate how puncture force differences for the different materials scale with strength (ultimate and yield). A similar technique can be used to examine how puncture force varies with the two additional (ductility-based) tensile parameters discussed earlier: percent elongation at ultimate and area under the stress-strain curve up until ultimate strength. Again, using a similar approach as to that discussed earlier, two normalized puncture force parameters can be introduced, F_{n4} and F_{n5} in Equation 34 and 35,

$$F_{n4} = \frac{F_i}{F_i^{TC128B}} \left[\frac{e_U^{TC128B}}{e_U^{Material}} \right] \tag{34}$$

$$F_{n5} = \frac{F_i}{F_i^{TC128B}} \left[\frac{(\sigma_{flow}\, e_U)^{TC128B}}{(\sigma_{flow}\, e_U)^{MATERIAL}} \right] \tag{35}$$

where tabulated results are shown in Table 28 and the two F_{n4} and F_{n5} average normalized puncture force results are plotted in Figure 73 (namely e_U in Figure 73(a) and $e_U \sigma_{flow}$ in Figure 73(b)).

The dispersion of the normalized puncture force data has increased when comparing the results in Figure 73 to the original uncorrected data (F_{n1} in Figure 64). This is especially true with the e_U corrected data, F_{n4} where the standard deviation has increased 5x from 0.22 to 1.12 (see Table 28). In the case of the $e_U \sigma_{flow}$ correction, F_{n5}, the standard deviation has increased less, namely 2x from 0.22 to 0.47. However, the observed average normalized puncture force standard deviation using both of these correction methods is greater than observed with either of the strength corrections.

In summary, the strength corrections indicate the critical role that material strength plays in governing puncture force. Clearly, the ultimate strength of the material is the primary variable, although as shown yield strength also plays a role in collapsing the force-deflection curves of the full-scale puncture simulations. The other two stress-strain parameters examined, namely e_U and $e_U \sigma_{flow}$ do not by themselves further collapse the puncture force data. Although this approach is useful for identifying the most critical variable, the cross-coupling (or in effect the interaction) that may occur with the different stress-strain parameters can only be established by using all of the different parameters in different forms of a model to relate stress-strain parameters to puncture energy.

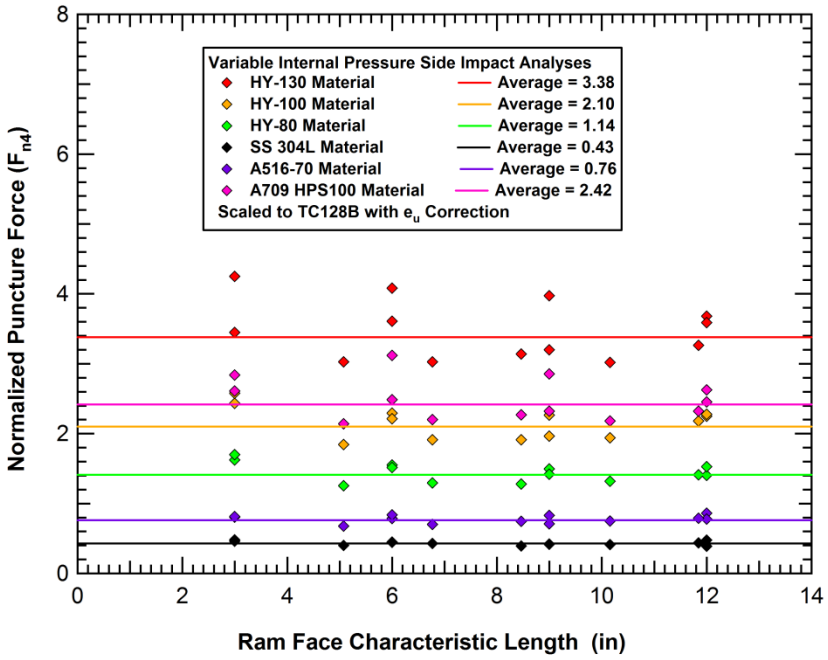

(a) elongation (at ultimate) correction

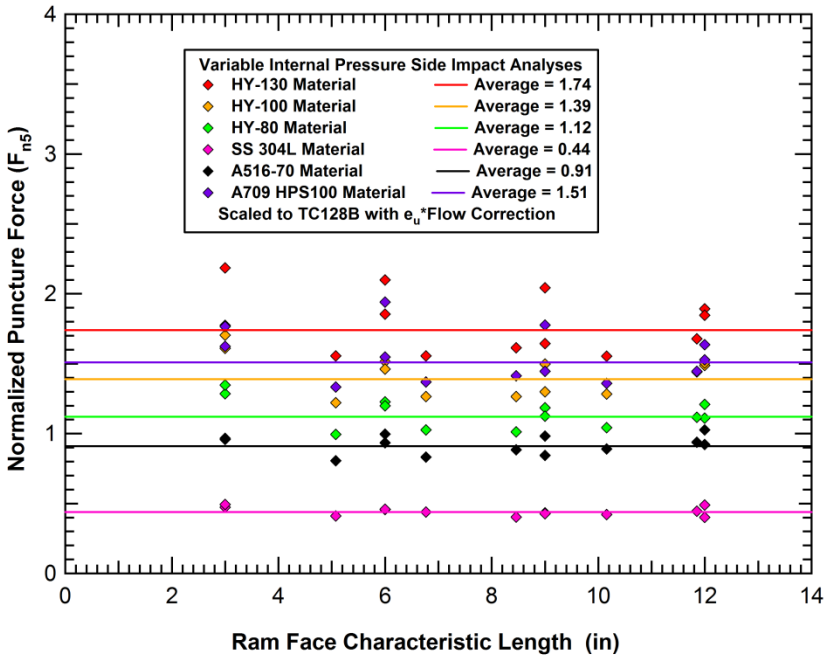

(b) area under the stress-strain curve (to ultimate) correction

Figure 73. Relative puncture force after two different corrections including ductility.

3.7 Puncture Energy Models

The above observations on the role stress-strain curve parameters allow us to put together a strength model that governs the material effects on the tank puncture energy. Remember that the puncture energy is obtained by integrating the force deflection curve up to the point of puncture. As shown in Figure 72, yield strength scaling does a reasonable job of collapsing the force-deflection curves for materials of varied strengths. Similarly, the force magnitude at which the tank is punctured is primarily controlled by the material ultimate strength. Although the two strength parameters correlate the different types of data reasonably well, it is arguable whether they provide a full correlation since the third significant parameter governing the stress-strain curve, elongation, is absent. Note that in Figure 72, the material with the highest ductility (304L stainless steel) has the largest variation in the functional model formulation. Therefore, elongation will also be considered as a variable in the puncture energy modeling. It will be included in two ways; first as a stand-alone term and second in a formulation using the energy under the stress-strain curve.

3.7.1 Model Form and Calibration

When developing a model, the first step is to understand what parameters govern behavior. This was accomplished to some degree in the previous Section 3.6.2 of this report where different stress-strain parameters were examined in the context of the puncture force. The next step is to use the governing physics to postulate a form of the model (coefficients and powers and combined terms including different parameters). Unfortunately, the puncture process is too complex to understand and capture the underlying physics with any degree of certainty. Recall, all of the puncture energy results were obtained from full-scale structural analyses (finite element analyses) that are not readily governed by simple relationships that allow understanding the role of the different variables involved. The tank deformation process includes contributions from the inertial behavior and kinematics of the tank, local deformation response in the dent formation (e.g. moving plastic hinges), and internal pressure work. Generating the average puncture energy values for each material is a complex, time-consuming undertaking utilizing all of the variables involved in a structural analysis.

Therefore, the approach utilized herein is to attempt to correlate puncture energy with stress-strain parameters using the simplest, lowest power correlations while minimizing interaction effects where multiple variables are combined in terms. If the simplest models manage to correlate the available data, there is no need for a more complex higher order model. Three models are utilized herein: one using two parameters (ultimate and yield strength) and two using three parameters (ultimate strength, yield strength and elongation at ultimate). We used the averaged normalized puncture energy values (E_{n1} as shown in Figure 65) obtained from the set of

side impact calculations to correlate the models and obtain regression constants. The definitions of the three models are as follows:

$$E_{Fit} = A_1\sigma_U + A_2\sigma_Y \quad (36)$$

$$E_{Fit} = B_1\sigma_U + B_2\sigma_Y + B_3 e_U \quad (37)$$

$$E_{Fit} = C_1\sigma_U + C_2\sigma_Y + C_3 e_U \sigma_{flow} = C_1\sigma_U + C_2\sigma_Y + C_3 e_U(\sigma_U + \sigma_Y)/2 \quad (38)$$

where E_{fit} (the curve fit normalized energy from the model) corresponds to the E_{n1} values for the different materials and the constants A_n, B_n and C_n were determined from linear regression of the normalized energy and the different model parameters ($\boldsymbol{\sigma_U}$, $\boldsymbol{\sigma_Y}$ and e_U). To aid in this companion discussion, the shorthand description of the three models in Equations 36-38 are the U-Y, U-Y-e and U-Y-eFlow models, respectively.

A summary of the models and the regression constants is provided in Table 29. The form of the model is shown along with the parameters involved, which include the curve fit constant (A_n, B_n and C_n) and the parameters that characterize the stress-strain curve. The measure of "goodness of fit", the R^2 error result (last column of Table 29) also provides a relative sense of the error incurred in the regression. What is interesting is that these three different models all tend to fit the calibration data reasonably well (exhibiting R^2 error results in excess of 0.9). The similarity of the R^2 error results for the three fits is striking; all yield values in the range of 0.92-0.93.

Table 29. Curve fit parameters for the two different models.

Model Name	Parameters Used			Form of Equation	Eqn. No.	Regression Constants	Fit R^2 error
	σ_U (ksi)	σ_Y (ksi)	Elong at UTS, in/in				
U-Y	✓	✓		$A_1\sigma_U + A_2\sigma_Y$	(36)	A_1 = 0.0200 A_2 = -0.0113	0.913
U-Y-e	✓	✓	✓	$B_1\sigma_U + B_2\sigma_Y + B_3 e_U$	(37)	B_1 = 0.0140 B_2 = -0.0054 B_3 = 0.821	0.917
U-Y-eFlow	✓	✓	✓	$C_1\sigma_U + C_2\sigma_Y + C_3 e_U \sigma_{flow}$	(38)	C_1 = 0.0132 C_2 = -0.0052 C_3 = 0.0146	0.926

Further detail of the fits, and the calibration data used to perform the regressions, are indicated in Table 30 along with the corresponding E_{fit} results from each of the models and the percent errors resulting at each observation. As shown, average normalized (to TC128B) puncture energy

results for seven materials were used to derive the regression constants. The similarity of the three fits was previously indicated with similar R^2 error results in Table 29. This similarity is also apparent from the statistical error analysis in Table 30. In terms of average error, the two three parameter models (eqns. 37 and 38) outperform the two parameter model (eqn 36) with average error for U-Y-eFlow 65% of that observed with the two parameter U-Y model. Standard deviations of error for all three are quite similar, in the range of 6.8-7.1%. Similarly the maximum and minimum error values observed are also fairly similar for the three fits.

The overall performance of the regression models relative to the calibration data is further examined in Figure 74 where the predicted results are plotted against the calibration data. The solid line would indicate perfect agreement between the calibration data and the fit data. All three models indicate good agreement with the calibration data with the predicted normalized energy resulting from the models typically within the dashed lines representing ±10% of the calibration data. This result is consistent with the findings in Table 30 with the standard deviation of the error; using the typical ±2 standard deviation comparison would imply prediction of the calibration data within 13.6-14.2% (the 95% confidence interval assuming a normal distribution of error).

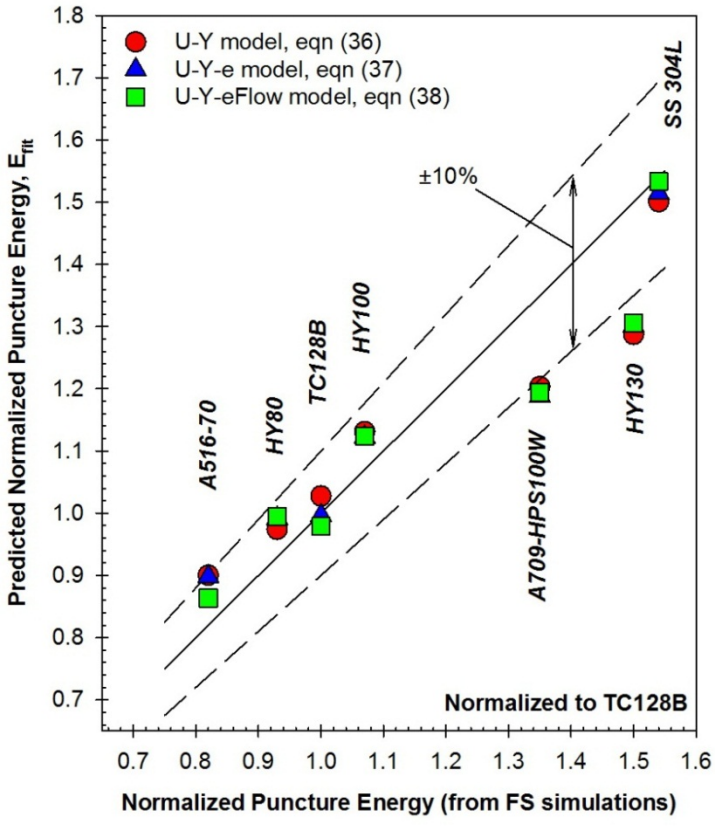

Figure 74. Curve fit comparisons and results for the three different models (data shown used to derive curve fit parameters).

Table 30. Curve fit results for the three different models.

Material	Normalized Average Energy	σ_U ksi	σ_Y ksi	Elong at UTS e_U, in/in	Specific Curve Fit Model Utilized [equation no.]					
					U-Y [36]		U-Y-e [37]		U-Y-eFlow [38]	
					E_{fit}	%error	E_{fit}	%error	E_{fit}	%error
A516-70	0.84	72	48	0.18	0.90	6.5	0.90	6.4	0.86	2.2
HY80	0.89	96	84	0.12	0.97	9.0	0.99	11.1	0.99	11.4
TC128B	1.00	84	58	0.16	1.03	2.8	0.99	-0.35	0.98	-2.1
HY100	1.03	114	102	0.09	1.13	10.3	1.12	9.4	1.12	9.6
A709	1.25	121	108	0.09	1.20	-3.4	1.19	-4.6	1.19	-4.1
HY130	1.39	141	136	0.07	1.29	-7.6	1.30	-6.6	1.31	-6.3
SS304L	1.56	98	41	0.44	1.50	-3.5	1.51	-2.6	1.53	-1.4
				average:		*2.02*		*1.8*		*1.3*
				standard deviation:		*6.96*		*7.1*		*6.8*
				minimum:		*-7.61*		*-6.6*		*-6.3*
				maximum:		*10.26*		*11.1*		*11.4*

In general, the results of all three models are fairly consistent and similar in magnitude across the range of energy levels considered. Prediction errors are mixed between the three models with no clear systematic trend exhibited as normalized puncture energy increases. What is striking about the three different formulations is that the predicted results are fairly consistent and the R^2 error is so similar between the three. Although the reason for this is unknown, it could simply be a consequence of the predominant role of the most critical tensile strength parameter. This parameter could be controlling the overall behavior with only a secondary influence from the other parameters included in the different formulations.

However, on balance it is valuable to have all three models. Inevitably, the models will be used to extrapolate to materials outside those used to calibrate the model. In this case, it is unknown how each behaves in regimes outside the bound of the calibration. Therefore, by using all three models the widest range of potential behavior could be postulated with results from all three factored into any decisions regarding candidate materials and where resources should be invested in to gain performance improvements with different materials.

3.7.2 Model Sensitivity to Input Stress-Strain Parameters

The models themselves, and the coefficients developed for each, can provide some insight into how tensile property changes affect puncture energy. However, the intermingling of all three stress-strain characterizations in the third term of the U-Y-eFlow model does complicate this assessment. Moreover the quantities used to characterize stress-strain behavior are also related to one another. For instance, it is typical to see ductility loss as strength is increased. Moreover, ultimate and yield strength changes are typically in the same direction for both quantities. Nevertheless, further insight into the models can be gained by examining theoretical changes in the input parameters.

The sign of the coefficients of the different models detailed in Table 29 provides some insight into the sensitivity of the different variables involved in the fit. Not surprisingly, the ultimate strength coefficient is positive, indicating energy increases with an increase in strength. This is contrasted by a negative coefficient for yield strength in all three models; this implies that a concomitant increase in yield strength results in a decrease in puncture energy. Although at first blush this result may seem counterintuitive, it occurs due to the increased stiffness of the force-deflection curve. Although the higher curve would dissipate more energy up to a given displacement, this effect is offset by the fact that the puncture strength is reached at lower displacement levels. This reduction in displacement at puncture produces the reduction in the puncture energy for higher yield stresses. Finally, an increase in elongation (at ultimate stress) results in an energy increase (see B_3 coefficient in Equation 37).

The form of the different puncture models can also be used to provide a sense of the puncture energy change given a certain magnitude increase in the controlling parameters. This assessment is provided in Table 31 detailing the theoretical energy change (assuming an overall energy of unity) given perturbations in the input parameters. Keep in mind the changes detailed in Table 31 differ. For instance, a strength change of ±5 ksi is a modest amount (within the scatter of test-to-test variability). For most of the materials considered the 5 ksi increment is less than 10% of the baseline strength (yield or ultimate). On the other hand, a ductility change of 2% (0.02 in/in) is a larger change, especially given the effective range of e_U material data (7-18% in Table 30, with the exception of the higher 44% for the stainless steel material).

Table 31. Puncture energy change resulting from different stress-strain parameter changes.

Parameter Change	*Percent Change in Puncture Energy*		
	U-Y model	**U-Y-E model**	**U-Y-eFlow model**
+5 ksi increase in σ_U	+10.0	+7.01	+6.63
+5 ksi increase in σ_Y	–5.66	–2.70	–2.59
0.02 in/in (2%) increase in e_U	n/a	+1.64	+0.03
+5 ksi increase in both σ_U and σ_Y	+4.37	+4.32	+4.04
+5 ksi increase in σ_U and -5 ksi decrease in σ_Y	+15.69	+9.71	+9.22

Based on the data in Table 31, the largest percent change in puncture energy, 7-10% overall, occurs with a +5 ksi increase in ultimate strength. A similar increase in yield strength results in a 3-6% decrease in energy (consistent with the negative sign of the second term of all the models). A 0.02 in/in (change in elongation by 2%) results in a smaller change in energy, on the order of 1.5%. Finally, Table 31 also indicates the puncture energy change for a like increase in both ultimate and yield, and a changing increase in ultimate (increasing) and yield (decreasing). The largest overall energy change, 9-16%, occurs for an increase in ultimate strength and a decrease in yield strength.

3.7.3 Applying the Puncture Models to Different Materials

Additional material test data (summarized in Appendix A) is available from this program as well as previous tank car research programs that can be used with the models developed herein to determine the resulting effect on tank car puncture. Available tensile properties include several nominal-chemistry TC128B (from the NGRTC program), different chemical variants of TC128B (including medium- and low-sulfur TC128B tested during Phase II of this program as well as special TC128B data provided by Arcelor Mittal) and the NUCU and A514B data tested during Phase I of this program. These data, and the model predictions for normalized puncture energy, are summarized in Table 32 and Figure 75.

Predicted puncture energy for four datasets of nominal chemistry TC128B are shown to the left in Figure 75, including “3074” which is the calibration data used to derive the curve fit parameters. The average normalized puncture energy (predicted by the U-Y model) for these four nominal chemistry TC128B materials is shown by the red line with ±2 standard deviations also indicated. The ±2 standard deviation band corresponds to approximately ±10%. Hence the

lot-to-lot variability of nominal chemistry TC128B yields approximately the same error band as we noted earlier during the model calibration shown in Figure 74.

The additional four TC128B datasets, with perturbed chemistries (three with reduced sulfur and one special chemistry variant), yield normalized puncture energy that is within the error band noted with different lots of TC128B material. This suggests that these modified chemistries do not yield markedly better puncture resistance than already observed in existing TC128B material (given the nominal TC128B band indicated in Figure 75). In fact, as sulfur decreases, the predicted puncture energy also decreases, regardless of which of the three puncture prediction models is utilized. This is likely a consequence of the lowered strength that is observed in lower sulfur material (without a concomitant increase in ductility).

The non-TC128B material shown in Table 32 and Figure 75 (NUCU and A514B, tested in this program) exhibit some enhancement of performance relative to TC128B. Both materials indicate puncture performance in the higher end of the TC128B range of behavior, although not significantly outside the range and therefore arguable from a statistical viewpoint. Of the two materials, the largest enhancement in puncture performances appears to be with A514B where all three models predict an increase in puncture performance. This is contrasted to the NUCU material where higher puncture energy is indicated by the U-Y model as opposed to the other two models that include a ductility term.

Table 32. Predicted puncture energy for different variants of TC128B and other materials.

Material Type and Reference			σ-ε Curve			Model Result, E_{fit}		
Material	**Source**	**Description**	σ_U **ksi**	σ_Y **ksi**	e_U **in/in**	**U-Y Eqn. (36)**	**U-Y-e Eqn. (37)**	**U-Y-eFlow Eqn. (38)**
TC128B (nominal)	NGRTC-Dow	TC ID. 3069	85	53	0.16	1.104	1.037	1.013
	NGRTC-Dow	TC ID. 3074	84	58	0.16	1.027	0.996	0.979
	NGRTC-Dow	0.777 plate	95	68	0.14	1.134	1.080	1.073
	Phase I	0.750 plate	96	77	0.14	1.052	1.046	1.050
TC128B (varied S)	Phase II	A-matl (med 0.005 S)	94	69	0.15	1.103	1.069	1.067
	Phase II	S-matl (low 0.002 S)	93	69	0.14	1.083	1.047	1.041
	Phase II	T-matl (low 0.002 S)	86	65	0.16	0.988	0.987	0.980
TC128B(S)	Arcellor Mittal	special chemistry	83	53	0.14	1.059	0.992	0.964
NUCU	Phase I	A710-GrB	94	61	0.13	1.193	1.096	1.077
A514B	Phase I	A514-GrB	122	113	0.07	1.166	1.159	1.151

Shaded row is data used in model calibration

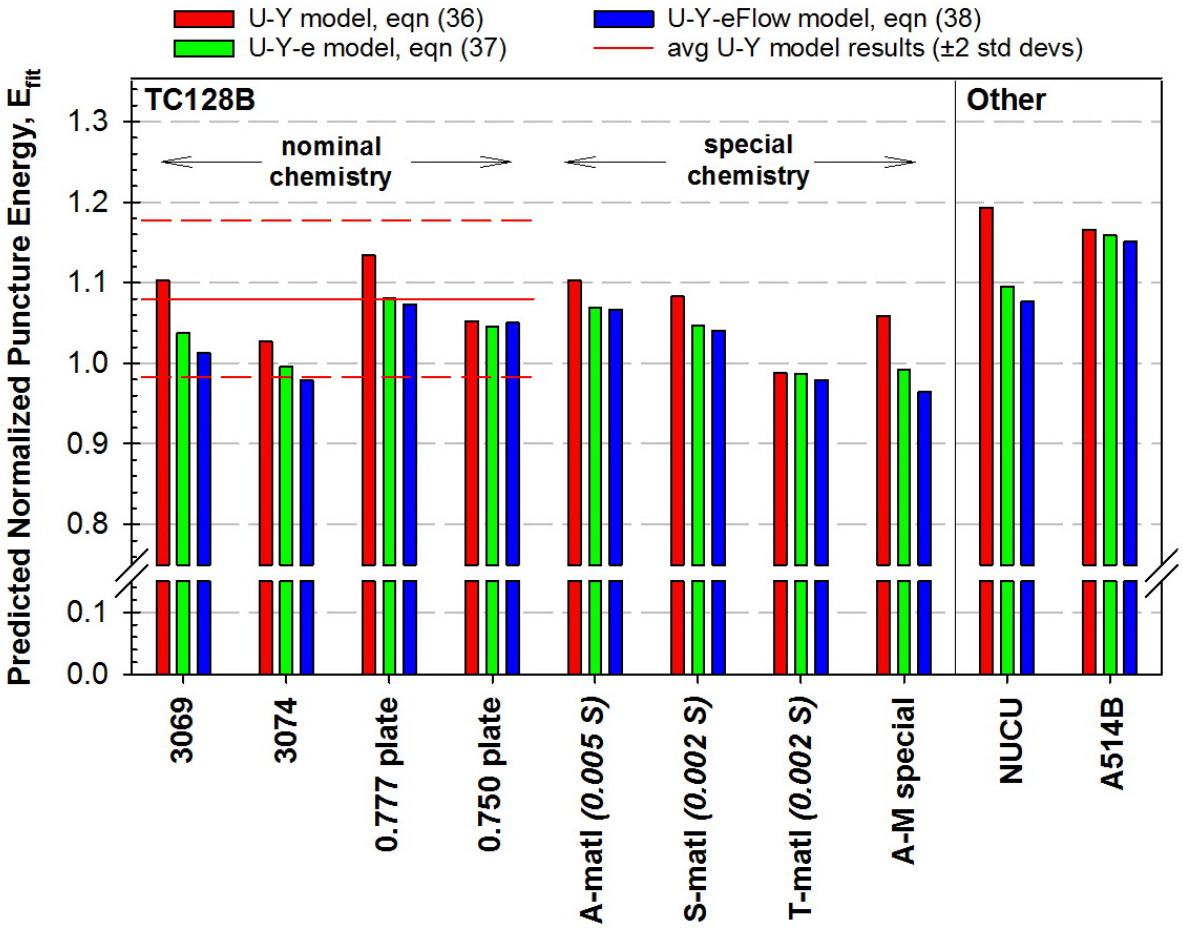

Figure 75. Model results for different variants of TC128B and other materials.

The sensitivity analyses performed in Section 3.7.3 suggest the possibility, with the optimum range of stress-strain parameters, of energy improvements of 2.2-2.6x when compared to nominal TC128B material. However, it must be noted that this is for an optimum (e.g. not real) material. In examining the real materials examined herein, the largest puncture energy improvement observed was on the order of 1.3-1.5x for HY130 and 304L stainless steel. This puncture energy increase translates into a 15-20% increase in "allowable" impact speed before puncture occurs (see Figure 66). Even in the best case situation of a 2x puncture energy improvement, this translates into a 40% increase in impact speed before puncture occurs (again, see Figure 66).

Given this, it is not unreasonable to note that the new and improved materials will net at best a modest improvement in puncture performance. Therefore higher levels of puncture improvement will likely be gained through additional modifications of the tank car structure that further improve puncture performance of tank cars.

The three models in the previous section, derived by empirically fitting energy results from the structural modeling using different stress-strain parameters, provide a viable method to compare and contrast different candidate materials for tank car structure. Admittedly the ability of the models to predict behavior outside of the data used to calibrate the models is as yet unknown. Nevertheless, having a tool to rapidly screen candidate materials is beneficial. Without this tool, expensive and time-consuming laboratory tests and full-scale simulations would be required to evaluate different candidate materials. Moreover these models can be used to help the industry determine the possible impact of different material modifications that impact mechanical properties. Given these tools, puncture enhancement of different candidate materials can be predicted to aid in material selection decisions and cost-benefit analyses.

4 Summary and Conclusions

This report describes the results of a research program to characterize and evaluate tank car steels with the objective of improving railroad tank car tank integrity. In this work, puncture force/energy is evaluated for a range of materials and impact scenarios. Puncture behavior is a structural response not easily quantified in any closed form manner (hence puncture prediction requires full-scale numerical simulation to assess behavior).

When this program was originally conceived, a number of different material failure models were proposed including the Bao-Wierzbicki, Gurson-Tvergaard and a maximum strain approach. These models involve different failure criteria that lead to development of puncture. In the end, the only suitable model was found to be the Bao-Wierzbicki model and hence it was focused on in this report.

The research program included detailed characterizations of various steel material samples (including a number of different TC128B variants). These detailed material characterizations included assessing tensile stress-strain properties as well as mechanical behavior of notched samples. As part of the research, detailed constitutive and damage models were developed for each material and the models were used to simulate the corresponding tests. An unexpected result of this process was that the commonly used von Mises yield criterion could not adequately model the full range of tests in the material characterization data. Specifically, the von Mises assumption that the yield condition is independent of the mean stress resulted in the inability of the model to reproduce the load displacement curves for both the smooth and notched tensile tests. This effect was more pronounced in specific materials (i.e., the tank car 3069 and new TC128B steel from the NGRTC program).

A summary of the material properties and material constitutive parameters is provided in Table A1 in Appendix A. The table includes the yield stress, ultimate stress, yield to ultimate (Y-U) ratio, elongation at ultimate stress, total elongation, smooth tensile to notched tensile ultimate ratio, Drucker Prager coefficient, modified Bao-Wierzbicki coefficient, longitudinal and transverse Charpy v-notch impact energy, whether the material has significant anisotropy in the longitudinal and transverse directions, and sulfur content for the materials (when available).

In addition to the direct material characterization, a series of puncture analyses were performed for various candidate materials to identify the material characteristics that most strongly control puncture resistance. To assist in this evaluation, we intentionally selected candidate materials with a wide range of mechanical properties, as shown in Figure 74. These materials were used in a suite of puncture analyses under various side impact conditions using a chlorine tank car geometry.

The material properties were investigated in different combinations in an attempt to understand the material characteristics that contribute most significantly to the puncture resistance. The goal was to relate puncture behavior (as determined from the full-scale numerical simulations) to the stress-strain properties of the materials (strength and ductility). Three models are proposed in this work, as described in Equations 36, 37 and 38 with overall performance of the three depicted in Figure 74, that include linear combinations of ultimate strength, yield strength and ductility (in this case, the percent elongation at ultimate or the area under the stress-strain curve to the ultimate strength of the material). All three models provide excellent predictions of the observed puncture behavior (within 10% of the TC128B-normalized puncture energy). It is not possible to differentiate between the three models given the calibration data used herein; therefore, all three models are proposed since it is likely that candidate tank car materials will perturb the input variables beyond the calibration range involved herein (in essence, extrapolating the models beyond the range of calibration).

The form of the models (in other words, how the different input parameters are combined) are simple linear combinations of different strength and ductility terms. This form is not based on any physics of the failure process; rather, the form is the simplest form available that provides a reasonable prediction of the numerical puncture simulations. The proposed models were determined empirically by least square fitting of the puncture data when combined with the different input variables.

Although these models are purely empirical, an examination of the numerical puncture force response clearly indicates the compelling role of the ultimate strength of the material in predicting puncture behavior. However, the force-deflection characteristics of the simulations exhibit reasonable correlation to the yield strength of the material. An increase in ultimate strength leads to higher puncture energy; conversely, an increase in yield strength leads to a lower puncture energy[4]. Nevertheless the utility of a puncture model including only strength (ultimate and yield) variables is limited since it does not adequately capture the effect of differing levels of ductility in the failure process (hence the introduction of the models that capture ductility).

These models provide a basis to predict the effect of differing strength and ductility on the puncture behavior of a rail tank car. However, material selection is not simply based upon stress-strain curve properties. There are other issues involved (such as weldability, corrosion and fatigue resistance, toughness, material cost etc.) that clearly are not captured by these models. Nevertheless, the three material puncture models provide a viable method to compare and

[4] Subsequent to the publication of the initial draft of this report, additional analyses were performed for head impacts of different materials (see Reference 51). These analyses found similar trends for the effects of yield and ultimate strength but with higher magnitudes of the effects.

contrast different candidate materials for tank car structure. Admittedly the ability of the models to predict behavior outside of the data used to calibrate the models is as yet unknown.

A predictive tool to rapidly screen candidate materials is beneficial to the tank car industry. Without this tool, expensive and time-consuming laboratory tests and full-scale simulations would be required to evaluate different candidate materials. Moreover these models can be used to help the industry determine the possible impact of different material modifications that impact mechanical properties. Given these tools, puncture enhancement of different candidate materials can be predicted to aid in material selection decisions and cost-benefit analyses. Applying these models to various combinations of strength and ductility indicates that the new and improved materials will net at best a modest improvement in puncture performance.

The current requirements for TC128B specify a minimum value of the yield stress and both a minimum and maximum value of the ultimate strength. However, it is likely that these specifications are provided more reflecting the chemistry of the TC128B rather than overall design considerations. It is likely that the minimum values are required to ensure that the tank car design has sufficient integrity for the operating conditions. However, considering only puncture resistance, there is no reason to specify a limit on the maximum ultimate strength for the material. As the puncture models indicate, from a puncture viewpoint it might make sense to place a limit on the maximum allowable yield stress for the material. But material specifications are a complex combination of characteristics of both the material and the design considerations.

In addition to identifying the characteristic of the materials that should be further investigated, there is some additional work that should be performed to carry this model further. Primarily, the strength model was shown to work well for side impacts on a chlorine tank car design. Some additional work is needed to confirm if the same (or similar) results are obtained for head impacts and on other tank designs of different thicknesses and at different pressure levels.

5 References

1. Kirkpatrick, S.W., “Detailed Puncture Analyses of Various Tank Car Designs,” ARA Final Technical Report, Prepared for the Next Generation Railroad Tank Car (NGRTC) Project, January, 2009.
2. McKeighan, P.C., “Tensile Properties and Stress-Strain Behavior of Various Steel Products Used in Fabricating Test Specimen for the NGRTC Program,” NGRTC Project Memorandum, Southwest Research Institute, 21 November 2007.
3. McKeighan, P.C., “Notched Tensile Properties of Tank Car Material from Full Scale Test No. 1 (Car No. 3069) and Test No. 2 (3074) Oriented in the Transverse Direction,” NGRTC Project Memorandum, Southwest Research Institute, 20 November 2007.
4. McKeighan, P.C., “Notched Tensile Properties of Thickest TC128B Tank Car Material from Material Inventory for Fabricating Test Specimens,” NGRTC Project Memorandum, Southwest Research Institute, 6 December 2007.
5. McKeighan, P.C., “Shear Tests on TC128B Normalized Material of Two Different Thicknesses,” NGRTC Project Memorandum, Southwest Research Institute, December 2007.
6. McKeighan, P.C., “Puncture Tests on Jacket Material (A1011, 90X) and Normalized TC128B Shell Material (two thicknesses)- Revised,” NGRTC Project Memorandum, Southwest Research Institute, 17 December 2007.
7. McKeighan, P.C., “Puncture Behavior of 0.48-inch Thick A516 Material,” NGRTC Project Memorandum, Southwest Research Institute, 12 April 2008.
8. McKeighan, P.C., “Puncture Properties of Different 90x Stacked Layers and a Composite Structure,” NGRTC Project Memorandum, Southwest Research Institute, 23 March 2008.
9. Anderson, T.L., Rose, B., McKeighan, P.C. and Kirkpatrick, S.W., “Quantifying and Enhancing Puncture Resistance in Railroad Tank Cars Carrying Hazardous Materials: Phase II – Development and Validation of a Puncture Resistance Evaluation Methodology” Technical Report, Prepared for The Chlorine Institute, December 20, 2007.
10. Tyrell, D.C., Jeong, D.Y., Jacobsen, K. and Martinez, E., "Improved Tank Car Safety Research," *Proceedings of the 2007 ASME Rail Transportation Division Fall Technical Conference*, RTDF2007-46013, September 2007.
11. National Transportation Safety Board, 2004: “Derailment of Canadian Pacific Railway Freight Train 292-16 and Subsequent Release of Anhydrous Ammonia Near Minot, North Dakota; January 18, 2002,” Railroad Accident Report NTSB/RAR-04/01.
12. National Transportation Safety Board, 2006: “Collision of Union Pacific Railroad Train MHOTU-23 with BNSF Railway Company Train MEAP-TUL-126-D with Subsequent Derailment and Hazardous Materials Release, Macdona, Texas, June 28, 2004,” Railroad Accident Report NTSB/RAR-06/03.
13. National Transportation Safety Board, 2005: “Collision of Norfolk Southern Freight Train 192 with Standing Norfolk Southern Local Train P22 with Subsequent Hazardous Materials

Release at Graniteville, South Carolina, January 6, 2005," Railroad Accident Report NTSB/RAR-05/04.

14. Bao, Y. and Wierzbicki, T., "On Fracture Locus in the Equivalent Strain and Stress Triaxiality Space," *International Journal of Mechanical Sciences* 46, 81-98.
15. Bao, Y. and Wierzbicki, T., "A Comparative Study on Various Ductile Crack Formation Criteria," *Journal of Engineering Materials and Technology* 126, 314-324.
16. Lee, Y-W and Wierzbicki, T., "Quick Fracture Calibration for Industrial Use," Massachusetts Institute of Technology Impact & Crashworthiness Laboratory, Report No: 115, August 2004.
17. Tang, Y., Yu, H., Gordon, J., Jeong, D. and Perlman, A.B., "Analysis of Railroad Tank Car Shell Impacts Using Finite Element Method," *Proceedings of the 2008 ASME/IEEE Joint Rail Conference*, JRC2008-63014, April 2008.
18. Bridgeman, P.W., Studies in Large Plastic Flow and Fracture, McGraw-Hill, New York, 1953.
19. Schwer, L.E. "Definition of Effective Stress and Effective Plastic Strain and Their Use in Constitutive Relations," APTEK, Inc., White Paper, 1987.
20. Malvern, L.E., Introduction to the Mechanics of a Continuous Medium, Prentice-Hall, 1969.
21. Spitzig, W.A., Sober, R. J. and Richmond, O., "The Effect of Hydrostatic Pressure on the Deformation Behavior of Maraging and HY-80 Steels and its Implications for Plasticity Theory," *Metallurgical Transactions A*, Vol. 7a, Nov. 1976, pp. 1703-1710.
22. Richmond, O. and Spitzig, W. A., 1980, ''Pressure Dependence and Dilatancy of Plastic Flow,'' International Union of Theoretical and Applied Mechanics Conference Proceedings, pp. 377–386.
23. Spitzig, W.A. and Richmond, O., "The Effect of Pressure on the Flow Stress of Metals," *Acta Metallurgica*, Vol. 32. No. 3, pp. 457-463. 1984.
24. Spitzig, W. A., Sober, R.J. and Richmond, O., "Pressure Dependence of Yielding and Associated Volume Expansion in Tempered Martensite," *Acta Metallurgica*, Vol. 23, July 1976, pp 885-893.
25. Kuroda, M., "Crystal plasticity model accounting for pressure dependence of yielding and plastic volume expansion," *Scripta Materialia* 48(2003) 605–610, 2002.
26. Wilson, C.D., "A Critical Reexamination of Classical Metal Plasticity," *Journal of Applied Mechanics*, Jan. 2002, Vol. 69, pp. 63-68.
27. Drucker, D. C., and Prager, W., 1952, ''Soil Mechanics and Plastic Analysis for Limit Design,'' *Q. Appl. Math.*, 10, pp. 157–165.
28. Beremin, F. M., 1981, "Study of Fracture Criteria for Ductile Rupture of A508 Steel," in *Advances in Fracture Research (ICF5)*, D. François, Ed., Pergamon Press , pp. 809-816.

29. Chaboche, J. L. et al., Editors, 1986, "Séminaire International sur l'Approche Locale de la Rupture," Conference Proceedings, Centre de Recherches EDF, "Les Renardières," Moret-sur-Loing, France.

30. Curran, D. R., Seaman, L. and Shockey, D. A, 1987, "Dynamic Failure of Solids," *Physics Reports*, Vol. 147, pp. 253-388.

31. Lemaitre, J., 1986, "Local Approach of Fracture," *Engineering Fracture Mechanics*, Vol. 25, pp. 523-537.

32. Mudry, F., 1985, "Methodology and Applications of Local Criteria for Prediction of Ductile Tearing," Elastic-Plastic Fracture Mechanics, L. H. Larson, ed., ECSC, EEC, EAEC, Brussels and Luxembourg, Belgium, pp. 263-283.

33. Hancock, J. W. and Mackenzie, A. C., 1976, "On the Mechanisms of Ductile Failure in High-Strength Steels Subjected to Multiaxial Stress States," *Journal of the Mechanics and Physics of Solids*, 24, pp. 147-169.

34. Rice, J. R., and Tracey, D. M., 1969, "On the Ductile Enlargement of Voids in Triaxial Stress Fields," *J. Mech. Phys. Solids*, 17, 201-217.

35. Giovanola, J. H., and Rosakis, A. J., Editors, 1992, *Advances in Local Fracture/Damage Models for the Analysis of Engineering Problems*, AMD-vol. 137, American Society of Mechanical Engineers, New York.

36. Giovanola, J. H. and Kirkpatrick, S. W., 1992, "Applying a Simple Ductile Fracture Model to Fracture of Welded T-Joints," in *Advances in Local Fracture/Damage Models for the Analysis of Engineering Problems*, AMD Vol. 137, J. H. Giovanola and A. J. Rosakis, Eds., American Society of Mechanical Engineers, New York, pp. 285-303.

37. Giovanola, J.H., and Kirkpatrick, S.W., 1993, "Methodology for Evaluating Strength and Fracture Resistance of Weldments Using a Local Approach to Fracture," in *Pressure Vessel Integrity-1993, PVP-Vol. 250*, W. E. Pennel, S. Bhandari, G. Yagawa, Editors, American Society of Mechanical Engineers, New York, pp.157-171.

38. Giovanola, J.H., Kirkpatrick, S.W. and Crocker, J.E., 1996, "Investigation of Scaling Effects in Elastic-Plastic Ductile Fracture Using the Local Approach," *Proceedings of the First European Mechanics of Materials Conference on Local Approach to Fracture*, Euromech-Mechamat '96, Fontainebleau-France, Sept. 9-11.

39. Gurson, A.L., "Continuum Theory of Ductile Rupture by Void Nucleation and Growth: Part 1—Yield Criteria and Flow Rules for Porous Ductile Media." *Journal of Engineering Materials and Technology*, Vol. 99, 1977, pp. 2-15.

40. Tvergaard, V., "On Localization in Ductile Materials Containing Spherical Voids." *International Journal of Fracture*, Vol. 18, 1982, pp. 237-252.

41. Tvergaard, V., "Material Failure by Void Growth to Coalescence." *Advances in Applied Mechanics*, Vol. 27, 1990, pp. 83-151.

42. Anderson, T. L. and Kirkpatrick, S.W., "Quantifying and Enhancing Puncture Resistance in Railroad Tank Cars Carrying Hazardous Materials," Technical Report, Prepared for The Chlorine Institute, August 7, 2006.

43. Mackenzie, A. C., Hancock, J. W., and Brown, D. K., 1977, "On the Influence of State of Stress on Ductile Failure Initiation in High-Strength Steels," *Eng. Fracture Mechanics*, 9, 167-188.

44. Reis, F., Malcher, L., Andrade Pires, F.M. and Cesar de Sa, J.M.A., "A Modified GTN Model for the Prediction of Ductile Fracture at Low Stress Triaxialities," *International Journal of Structural Integrity*, vol. 1, no. 4, 2010.

45. Zhang, Z. L., "A complete Gurson Model," in *Nonlinear Fracture and Damage Mechanics*, edited by M. H. Alibadi, WIT Press Southampton, UK, 2001, pp. 223-248.

46. Nahshon, K. and Hutchinson, J. W., "Modification of the Gurson model for shear failure," *European Journal of Mechanics* 27 (1), 1–17, 2008.

47. Fuech, M., Sun, D.-Z., Erhart, T. and Frank, T., "Recent Development and Applications of the Gurson Model," LS-DYNA Anwenderforum, Ulm, 2006.

48. Association of American Railroads, Technical Services Division, Mechanical Section—Manual of Standards and Recommended Practices.

49. "Draft of NTSB Material Laboratory Factual Report [In reference to Canadian Pacific Railway Derailment and Anhydrous Ammonia Release, Minot, ND, January 18, 2002, DCA-02-MP-002]," Frank Zakar, Metallurgy Group Chairman, Feb. 14, 2003.

50. Kirkpatrick, S.W., "Detailed Puncture Analyses of Various Tank Car Designs - Analysis of Different Impactor Threats and Impact Conditions," Federal Railroad Administration (FRA) Final Report, Report No. DOT/FRA/ORD-13/17, March 2013.

51. S.W. Kirkpatrick, "TWP-4 Assessing Puncture Resistance for Sandwich Tank Car Designs; TWP-5 Composite Materials for Protection Systems; TWP-22 Advanced Head Protection Concepts," Advanced Tank Car Collaborative research Program (ATCCRP) Research Report, Draft Final Technical Report for Projects TWP-4, TWP-5, and TWP-22, September 2017.

Appendix A – Supplemental Data

Table A1. Comparison of the various candidate tank car material properties.

Material	Yield Stress (ksi)	Ultimate Stress (ksi)	Y-U ratio	Elong. At UTS	Elong.	ST/NT Ratio	D-P Coeff. (α)	Mod. BW Coeff. (n)	Long. CVN (ft-lbs)	Trans. CVN (ft-lbs)	L-T Isotropy	Sulfu
TC128B (3069)	53	85	1.60	0.16	0.32	1.47	0.120	1.6	146	80	Yes	-
TC128B (3074)	58	84	1.44	0.16	0.32	1.50	0.050	1.0	136	106	Low	0.003
TC128B (0.777)	68	95	1.40	0.14	0.32	1.42	0.195	1.0	-	-	Low	0.007
TC128B (0.750)	77	96	1.25	0.14	0.29	1.58	0.040	1.0	70	65	Low	0.008
TC128B (A289)	69	94	1.36	0.15	0.29	1.54	0.050	1.0	120	105	Low	0.005
TC128B (S288)	69	93	1.35	0.14	0.28	1.53	0.050	1.6	117	119	Low	0.002
TC128B (T290)	65	86	1.31	0.16	0.33	1.53	0.050	TBD	130	147	Low	0.002
NUCU (A710-B)	61	94	1.54	0.13	0.25	1.53	0.015	1.0	139	175	Low	-
A514B	113	122	1.08	0.07	0.18	1.61	0.035	2.2	96	139	Yes	-
HPS100W	108	121	1.12	0.09	0.25	1.61	0.045	1.6	180	205	Low	-
HY-80	84	96	1.14	0.12	0.26		-	-	-	-	-	-
HY-100	102	114	1.12	0.09	0.23		-	-	-	-	-	-
HY-130	136	141	1.04	0.07	0.23	1.65	-	1.9	-	-	-	-
SS 304L	41	98.0	2.40	0.44	0.55		-	-	-	-	-	-
A516-70	48	72	1.50	0.18	0.40		-	-	-	-	-	-

Spec. ID No.	UTS, ksi	YS, ksi	elong, %
151N3SR3_L1	82.3	52.5	41.5
151N3SR3_L2	83.0	53.2	40.6
average:	*82.7*	*52.9*	*41.1*

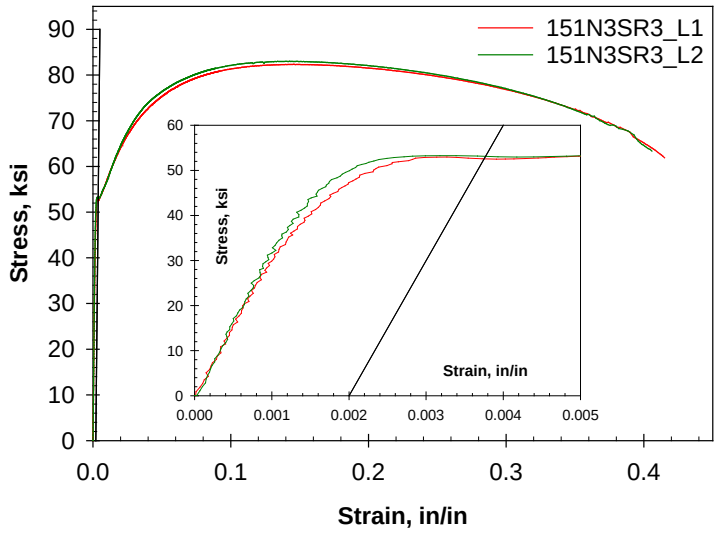

Figure A1. Tensile stress-strain results of special TC128B (data provided by ArcelorMittal)[5]

[5] Special (reduced carbon and niobium) TC128B material produced by ArcelorMittal (data supplied by William Heitmann), reference De, A.K., Gungor, O.E. and Manohar, M., "Development of a High Toughness Steel with Enhanced Upper Shelf Energy for Pressure Tank Car Applications," ArcelorMittal Global R&D, presentation at the Tank Car Committee Meeting, Dallas, TX, April 2015.

Appendix B – Characterization of 304L Stainless Steel

Introduction

During the performance of the TWP-10 project, described in the main body of this report, the steel characteristics required for improved puncture resistance were identified. The recommendations coming out of that TWP-10 research effort included:

1. Investigate high strength (130 ksi) steels but with lower yield and properties desirable for tank car steels.

2. Perform a detailed characterization of 304L stainless steel.

3. Investigate lower cost alternatives that provide properties similar to 304L stainless.

The second recommendation was selected as a priority and the ATCCRP committee funded a follow-on effort to complete this task. The results of this subsequent effort are described in this appendix.

The statement of work for the follow-on effort included:

Task 1 – Perform a TWP-10 material characterization test series on ASTM A240 Type 304L stainless steel including tensile, notched tensile, and high-rate tensile test series.

Task 2 – Develop detailed TWP-10 constitutive model including a Drucker-Prager yield criterion and Bao-Wierzbicki damage and failure model.

Task 3 – Confirm material performance in impact calculations.

Characterization Testing

The material characterization test program included longitudinal and transverse tensile tests, notched round bar tensile tests, and longitudinal tensile tests at elevated strain rates. The objective was to perform three repeat tests at each condition to assess repeatability of results. The tensile and notched tensile data for the 304L stainless material are shown in Figure B1. Similarly, the high rate tensile testing results are shown in Figure B2. These high rate tests use a round bar specimen geometry with a shortened specimen gauge length. For comparison, the quasistatic longitudinal tensile behavior measured with the standard round bar tensile test with the 2-inch gauge section length is also provided in the figure.

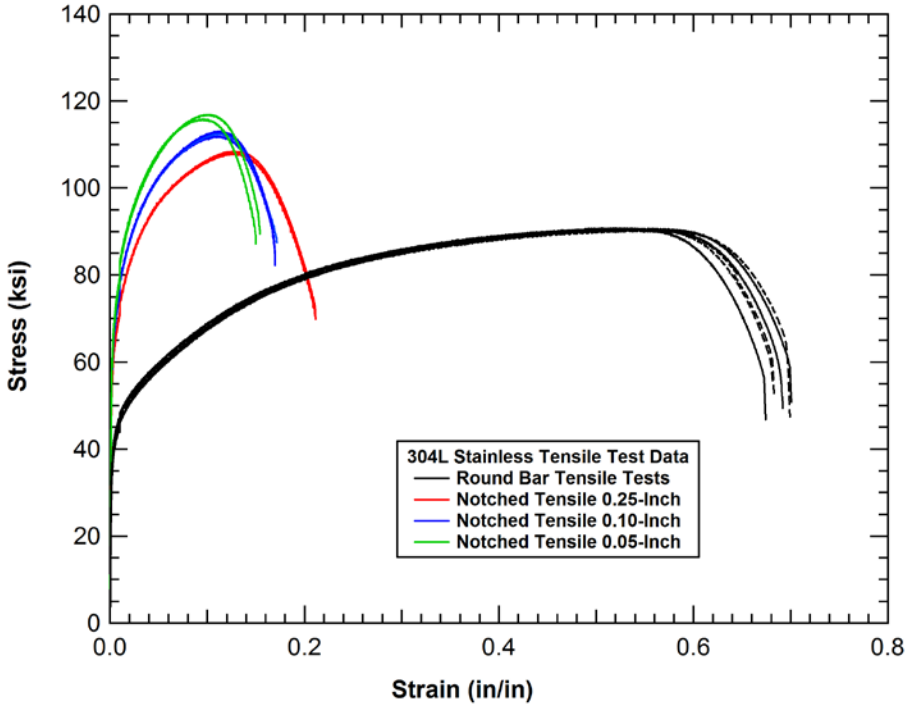

(a) Tensile data summary

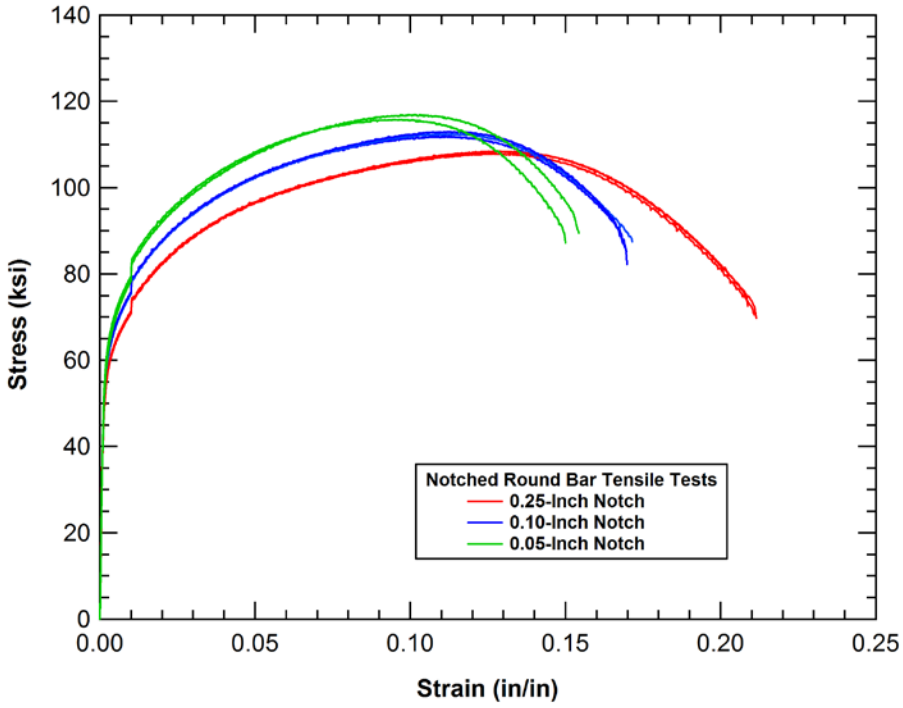

(b) Notched tensile data only

Figure B1. Summary of the 304L stainless quasistatic tensile test data.

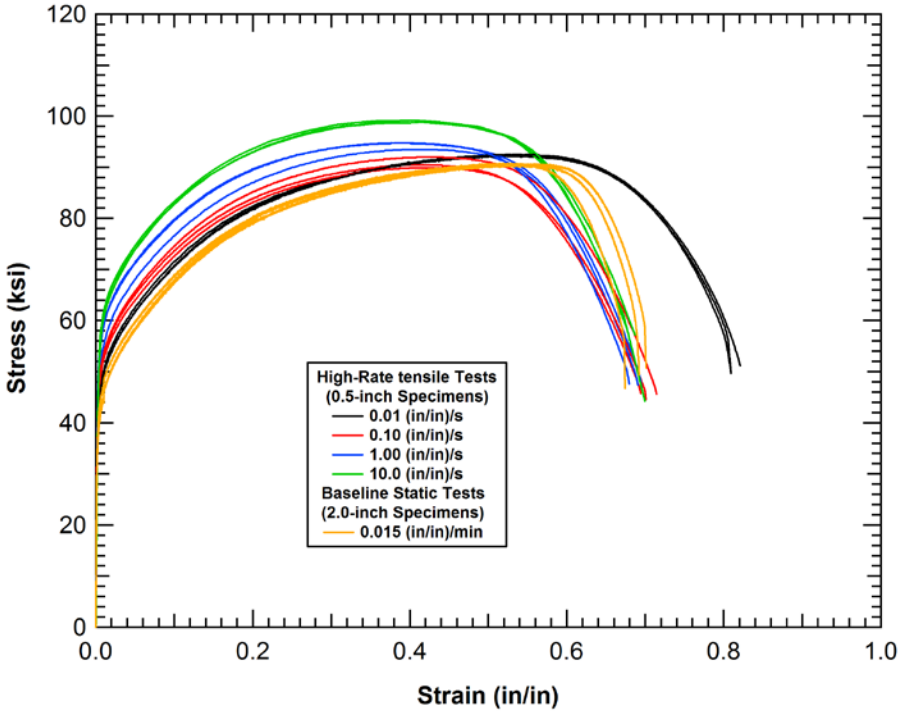

Figure B2. Summary of the 304L stainless tensile test data at elevated strain rates.

The tensile data, shown in Figure B1, has a yield strength of 36 ksi and an ultimate tensile strength of 90 ksi with an elongation of approximately 0.68. These values compare favorably to the required ASME A240 minimum properties for 304L stainless steel of 25 ksi yield strength, 70 ksi tensile strength, and 40% elongation. It is also reasonably consistent with other data found in open literature for 304L stainless steel. In addition the data compares favorably to that used to create the ASTM A240 304L used in the original TWP-10 study described in Section 3.5. The primary difference is approximately a 5 ksi lower tensile strength of the new data.

The notched tensile data, shown in Figure B1, indicates a different behavior from the previous steels tested in that the notched specimens are more different from the smooth round bar result and there is less variation between the different notch radii than seen for the previous carbon steels tested. We believe this is primarily a result of the stainless having both a very large ductility and a large amount of hardening that result in a modification of the notch shape and corresponding influence on the triaxiality levels in the notched specimens as they deform. Note that there was also a slightly different specimen geometry used for these notched tensile tests in this series compared to the original specimen design. The original design used in the baseline TWP-10 test series, shown in Figure B3, uses a 0.50-inch bar diameter outside the notch. The new design used in this TWP-10A test series, shown in Figure B4, used a 0.38-inch bar diameter outside the notch. Analysis of the two specimen geometries shows that this bar diameter plays a

role in the measured response, but is not the primary factor influencing the characteristics of the notched tensile test behaviors.

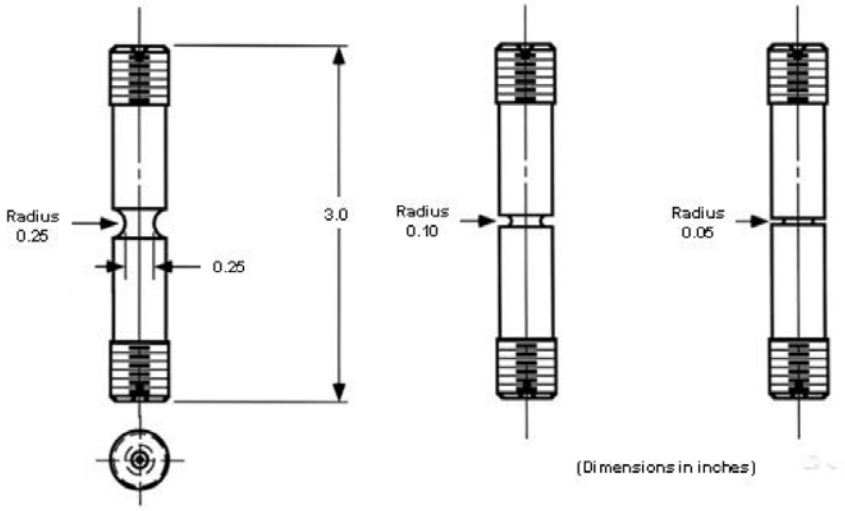

Figure B3. Notched specimen geometry used in previous testing detailed in the body of this report.

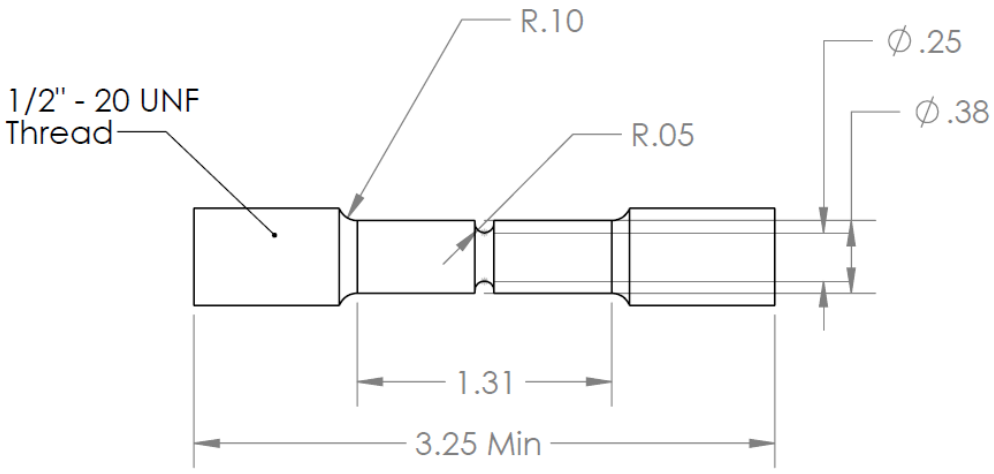

Figure B4. Notched specimen geometry used in stainless steel testing detailed in this Appendix.

The high strain rate tensile data, shown in Figure B2, shows a more significant strain rate effect than typically seen for carbon steels in the range of rates tested. The ultimate strength of the material increases by approximately 7% over the range of rates tested and the elongation is reduced by approximately 15%. At intermediate strain levels, the rate effects on the stress can be more significant (approximately 10-15%). However, due to the strain rates and distribution of plastic strain magnitudes seen in the tank impact behavior, we believe that accurate assessments of the impact response will still be obtained in simulations that neglect the strain rate effects.

The conversion of the smooth round bar tensile test data to true stress and the corresponding piecewise linear fit to the data used for the material constitutive model are both shown in Figure B5. This conversion to the true stress-strain behaviors was described in Section 2.4 of this report. This constitutive model fit was used to simulate the tensile test configuration and the corresponding comparison to the test data is shown in Figure B6. The good agreement between the tests and model show that the tabular fit is accurate and has been correctly implemented in the model.

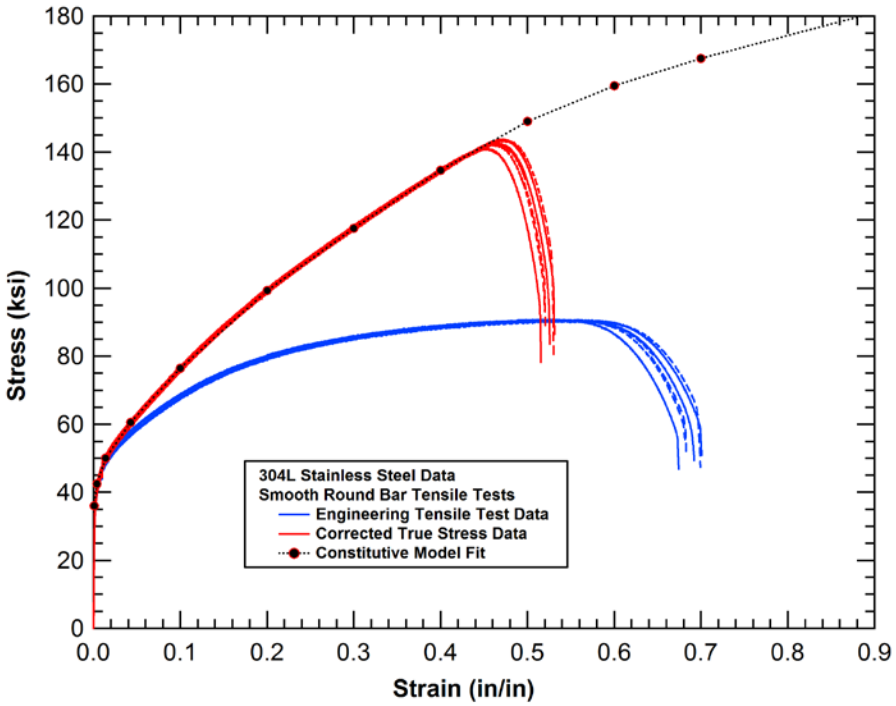

Figure B5. Comparison of the measured and calculated 304L stainless tensile behavior.

The resulting constitutive model developed from the smooth round bar tensile test was subsequently applied to simulate the notched round bar tensile specimens. The correlation of the measured and calculated behaviors for the notched tensile tests is shown in Figure B7. The model gives good agreement for both the smooth round bar tensile test and for the notched tensile test with the smallest 0.05-inch notch radius. For the intermediate 0.10-inch and 0.25-inch notch radii, the model under-predicts the peak tensile strength (by approximately 3% and 6% respectively) and elongation. The problem is that any changes that could be made to the model to improve correlation at these intermediate notch radii would reduce the correlation at either (or both) of the smooth tensile or sharp notch radii test conditions. As a result, this model was used as the final fit to the data and the corresponding model parameters are provided in Table B1.

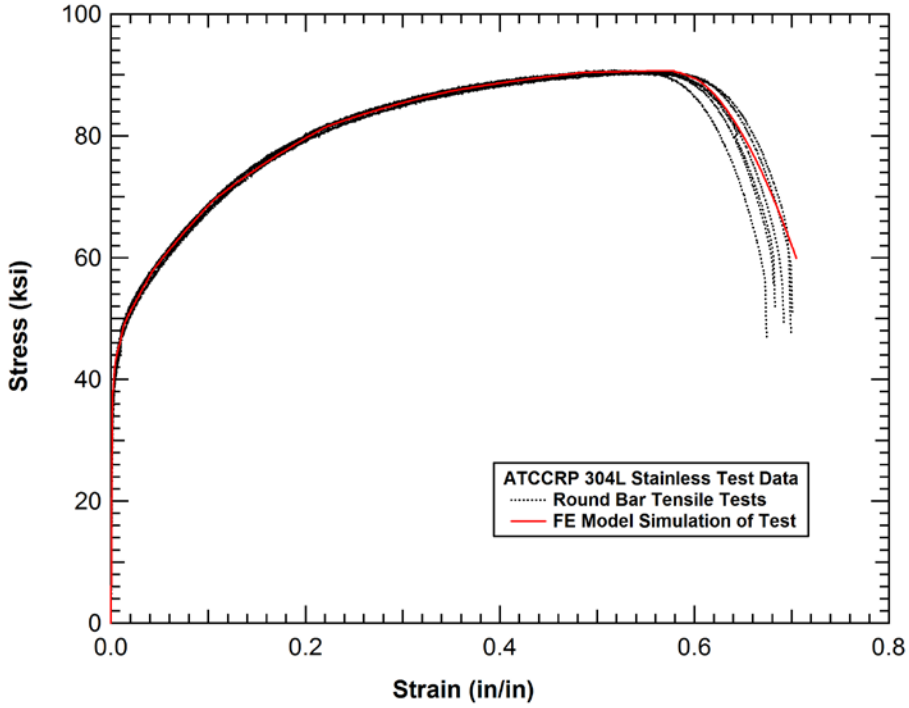

Figure B6. Comparison of the measured and calculated 304L stainless tensile behavior.

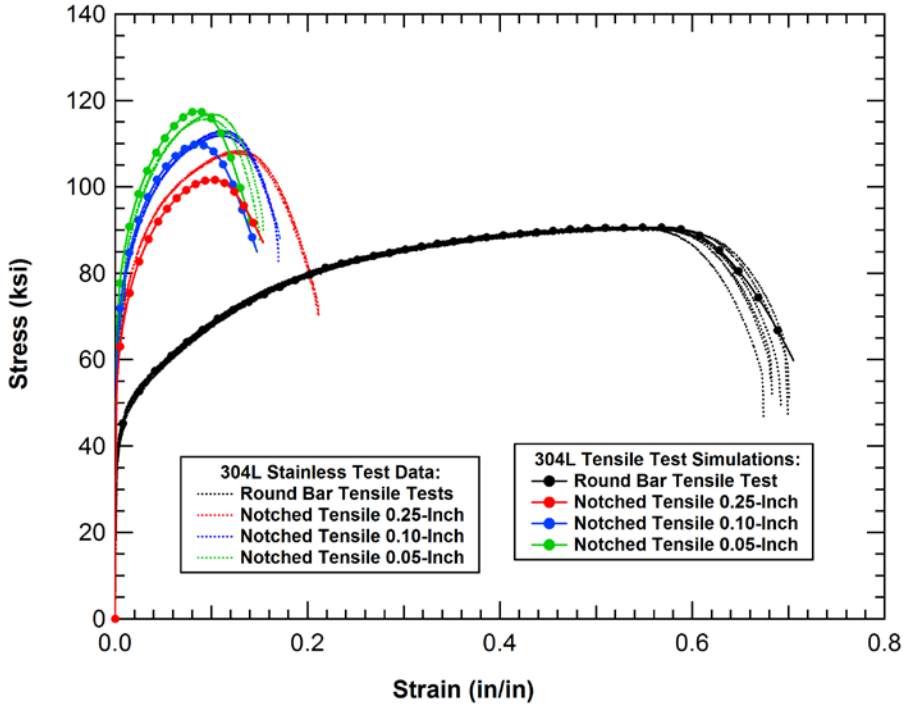

Figure B7. Comparison of the measured and calculated 304L stainless tensile behavior.

Table B1. Material constitutive parameters and tabular 304L stress-strain values.

Material Constitutive Parameters		
Bao Wierzbicki Coefficient - A		0.96
Bao Wierzbicki Coefficient - B		2.40
Modified Bao Wierzbicki Coefficient - n		1.00
Drucker Prager Coefficient - α		0.00
Point No.	**Plastic Strain (in/in)**	**True Stress (ksi)**
1	0.000E+00	36.0
2	2.483E-03	42.5
3	1.233E-02	50.0
4	4.098E-02	60.5
5	9.745E-02	76.5
6	1.967E-01	99.3
7	2.961E-01	117.6
8	3.955E-01	134.6
9	4.945E-01	149.0
10	5.900E-01	159.5
11	6.900E-01	167.5
12	1.690E+00	235.0

The resulting constitutive model was applied to the simulation of blunt impact tank punctures. The initial impact scenario investigated was an impact of a 105J600I tank car design with a 6x6-inch impactor. For the initial investigation, three different simulations were compared. One of the simulations was the original simulation performed with the ASTM A240 304 stainless steel as part of the original TWP-10 study described in Section 3.5. Since that time, some additional improvements were made to the puncture models and modeling parameters. In addition, the version of LS-DYNA currently being used for analyses has been updated. As a result the second simulation was performed using an updated impact model but with the original ASTM A240 304

stainless steel constitutive model. Finally, a simulation was performed using the new ASTM A240 304L stainless steel constitutive model described in this appendix.

The comparison of the calculated force-deflection characteristics for the three impact simulations is shown in Figure B8. The first observation is that the two new simulations, using the original and the new 304L stainless steel constitutive models, are nearly identical. This is good news in that it indicates the new model does not significantly influence the puncture behavior compared to the original model used in the study. The outlier is the original impact simulation that corresponds well for the majority of the force-deflection curve but punctures prematurely at a force that is approximately 8% lower than in the new simulations. Because of the kinematics of this impact scenario, this premature puncture resulted in a significant 36 percent reduction in the calculated puncture energy, compared to the new simulations.

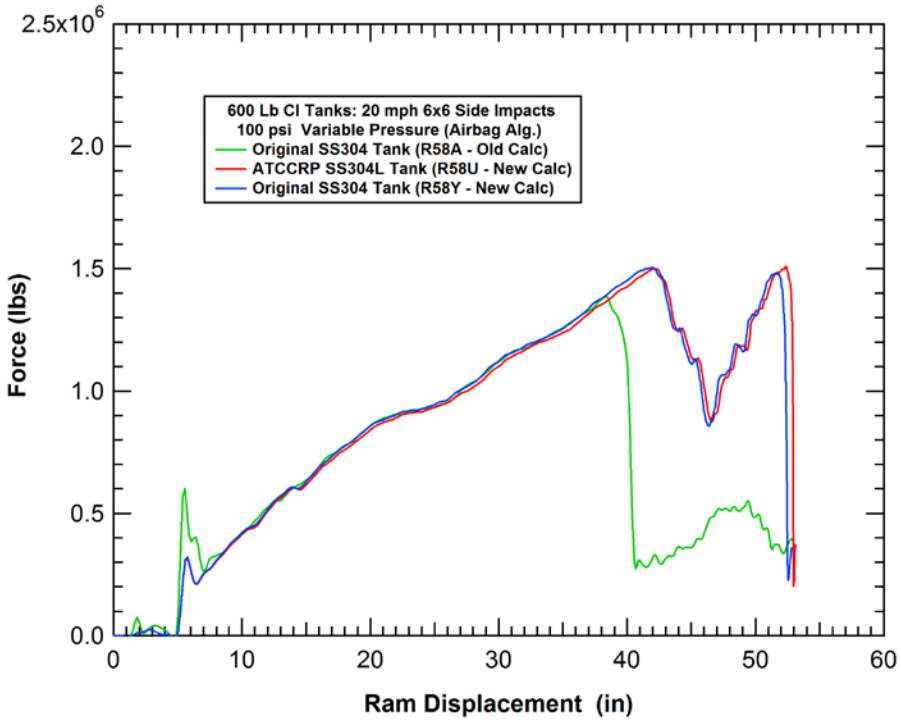

Figure B8. Comparison of the calculated stainless steel tank impact behaviors.

An investigation determined that a time-step based element erosion parameter (DTMIN) was responsible for the premature failure in the old simulation. This parameter is set to allow for elements that experience a large deformation to be deleted if they are controlling the calculation timestep at a level below the fraction of the original timestep. The idea is to prevent a few elements that have been highly distorted from significantly reducing the calculation time step size, and consequently increasing the calculation run time. Typically, these are elements along a

fracture zone or in a high distortion crush zone and deleting them has no significant influence on the calculated response.

In this simulation, the high ductility of the stainless steel, combined with the assigned value of DTMIN, resulted in element deletions that did influence the response for this scenario. Additional analyses were therefore performed to assess the magnitude of the effect. The additional calculations were performed for the 3-inch, 9-inch, and 12-inch impactors using the new constitutive model and updated impact models. The comparisons of the original and updated model simulations are shown in Figure B9. The comparison shows that the effect seen in the 6-inch impactor is by far the largest for the various impact conditions. The other impact conditions see a smaller single digit difference in both puncture force and puncture energy. As a result, the conclusions of the high puncture performance of 304L stainless steel in the previous analyses are still valid and the performance gain estimates are conservative based on these previous analyses.

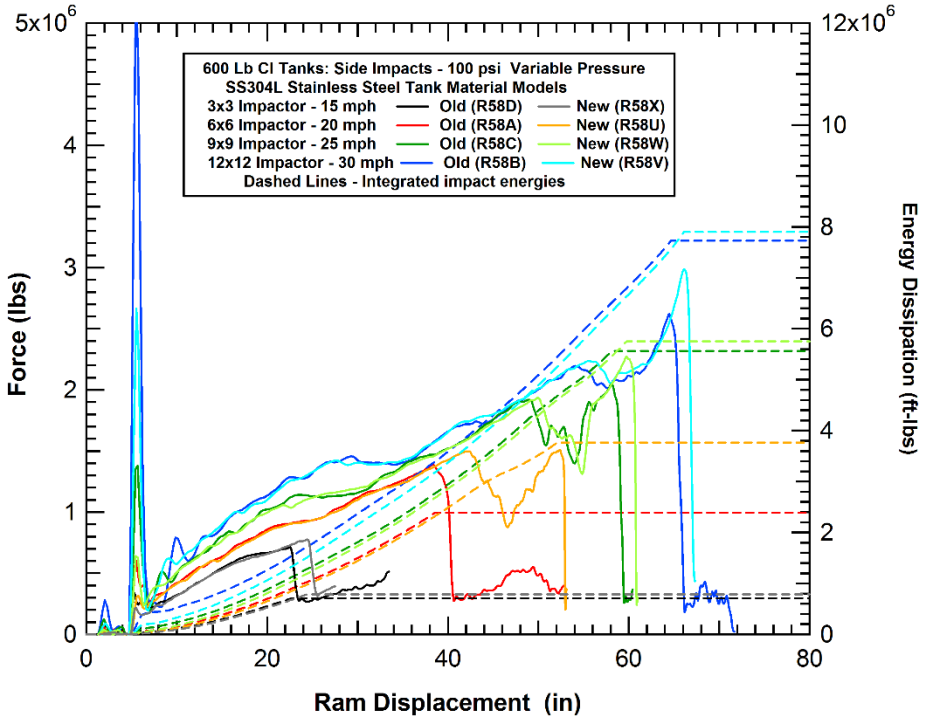

Figure B9. Comparison of the measured and calculated 304L stainless tensile behavior.

A secondary check on the modeling effect of DTMIN was also performed using updated analyses on the material with the second largest ductility (elongation) in the material screening study. This was the A516-70 material described in Section 3.5. In these simulations the effects of the new modeling parameters was significantly less than seen in the 304L stainless steel. Thus, the effect of the modeling parameters on puncture response were primarily a result of the

unusually high elongation behavior of stainless steel and not significant for the other materials evaluated.

Summary and Conclusions

During the performance of the main TWP-10 project, the steel characteristics required for significant increases in puncture resistance were identified. The recommendations coming out of that research effort included performing a detailed characterization of 304L stainless steel to provide test data and confirm the analyses predicting high puncture performance for that material.

The material characterization test program performed on the 304L stainless steel included longitudinal and transverse tensile tests, notched round bar tensile tests, and longitudinal tensile tests at elevated strain rates. Good quality data was obtained and the results were summarized in this appendix.

A material constitutive and damage model was developed based on the new 304L stainless material characterization tests and the existing TWP-10 methodology. The model was used in tank impact analyses to re-evaluate the puncture performance of the 304L stainless steel. The assessment identified an inaccuracy introduced in the original analyses from a modeling parameter. However, the assessment determined that the effect was relatively small and would not have significantly changed the results or conclusions of the original study. Furthermore, the effect would have slightly underestimated the performance of the stainless steel material.

The final conclusion is that the testing and analyses performed in this supplemental study are consistent with the previous results and continue to indicate the superior puncture resistance of the 304L stainless steel compared to the carbon steels evaluated. Further validation of this conclusion would require impact and puncture testing on a 304L stainless steel tank structure or an alternative impact and puncture test specimens.